

Utah State University

DigitalCommons@USU

All Graduate Theses and Dissertations

Graduate Studies

5-2015

Experimental Validation Data for CFD of Steady and Transient Mixed Convection on a Vertical Flat Plate

Blake W. Lance
Utah State University

Follow this and additional works at: <https://digitalcommons.usu.edu/etd>



Part of the [Mechanical Engineering Commons](#)

Recommended Citation

Lance, Blake W., "Experimental Validation Data for CFD of Steady and Transient Mixed Convection on a Vertical Flat Plate" (2015). *All Graduate Theses and Dissertations*. 8094.
<https://digitalcommons.usu.edu/etd/8094>

This Dissertation is brought to you for free and open access by the Graduate Studies at DigitalCommons@USU. It has been accepted for inclusion in All Graduate Theses and Dissertations by an authorized administrator of DigitalCommons@USU. For more information, please contact digitalcommons@usu.edu.



EXPERIMENTAL VALIDATION DATA FOR CFD OF STEADY AND TRANSIENT
MIXED CONVECTION ON A VERTICAL FLAT PLATE

by

Blake W. Lance

A dissertation submitted in partial fulfillment
of the requirements for the degree

of

DOCTOR OF PHILOSOPHY

in

Mechanical Engineering

Approved:

Dr. Barton L. Smith
Major Professor

Dr. Robert E. Spall
Committee Member

Dr. Aaron Katz
Committee Member

Dr. Nick A. Roberts
Committee Member

Dr. Eric D. Held
Committee Member

Dr. Mark R. McLellan
Vice President for Research and
Dean of the School of Graduate Studies

UTAH STATE UNIVERSITY
Logan, Utah

2015

Copyright © Blake W. Lance 2015

All Rights Reserved

ABSTRACT

Experimental Validation Data for CFD of Steady and Transient Mixed Convection on a Vertical Flat Plate

by

Blake W. Lance, Doctor of Philosophy

Utah State University, 2015

Major Professor: Dr. Barton L. Smith

Department: Mechanical and Aerospace Engineering

Simulations are becoming increasingly popular in science and engineering. One type of simulation is Computation Fluid Dynamics (CFD) that is used when closed forms solutions are impractical. The field of Verification & Validation emerged from the need to assess simulation accuracy as they often contain approximations and calibrations.

Validation involves the comparison of experimental data with simulation outputs and is the focus of this work. Errors in simulation predictions may be assessed in this way. Validation requires highly-detailed data and description to accompany these data, and uncertainties are very important.

The purpose of this work is to provide highly complete validation data to assess the accuracy of CFD simulations. This aim is fundamentally different from the typical discovery experiments common in research. The measurement of these physics was not necessarily original but performed with modern, high-fidelity methods. Data were tabulated through an online database for direct use in Reynolds-Averaged Navier-Stokes simulations. Detailed instrumentation and documentation were used to make the data more useful for validation. This work fills the validation data gap for steady and transient mixed convection.

The physics in this study included mixed convection on a vertical flat plate. Mixed convection is a condition where both forced and natural convection influence fluid momentum and heat transfer phenomena. Flow was forced over a vertical flat plate in a facility built for validation experiments. Thermal and velocity data were acquired for steady and transient flow conditions. The steady case included both buoyancy-aided and buoyancy-opposed mixed convection while the transient case was for buoyancy-opposed flow. The transient was a ramp-down flow transient, and results were ensemble-averaged for improved statistics. Uncertainty quantification was performed on all results with bias and random sources.

An independent method of measuring heat flux was devised to assess the accuracy of commercial heat flux sensors used in the heated wall. It measured the convective heat flux by the temperature gradient in air very near the plate surface. Its accuracy was assessed by error estimations and uncertainty quantification.

(127 pages)

PUBLIC ABSTRACT

Experimental Validation Data for CFD of Steady and Transient Mixed Convection on a Vertical Flat Plate

by

Blake W. Lance, Doctor of Philosophy

Utah State University, 2015

Major Professor: Dr. Barton L. Smith

Department: Mechanical and Aerospace Engineering

In this computer age, simulations are becoming common in science and engineering. One category of simulation, Computational Fluid Dynamics (CFD), begins with physical equations but adds approximations and calibrations in order to complete solutions. Translating these equations into computer languages may cause unintended errors. If simulation results are to be used for decision making, their accuracy needs to be assessed. This accuracy assessment is the theory behind the field of Verification & Validation.

Verification involves confirming the translation of physical equations to computer language was performed correctly. It also features methods to detect many types of code errors. Validation is quite different in that it involves the comparison of experimental data with simulation outputs. This way, errors in simulation predictions may be assessed. Validation requires highly-detailed data and description to accompany these data, and uncertainties in these data are very important. Ideally, the validation experiment measures all information required for simulation inputs. Matching inputs ensures that any possible differences in the outputs are only due to the model.

The purpose of this work is to provide highly complete validation data to assess the accuracy of CFD simulations. The physics were mixed convection. Convection is a heat transfer mode where heat is carried by a moving fluid. Mixed convection occurs where natural convection and forced convection forces are similar, such as in low-speed flows. A vertical flat plate is heated and used for a convection boundary condition. A wind tunnel that was built specifically for validation experiments was used. Air is the working fluid whose velocity is measured using a modern optical technique called Particle Image Velocimetry. Many thermocouples were used to measure the temperature of all four walls and the inlet air. Commercial heat flux sensors (HFSs) were used in the heated wall.

The two cases were steady and transient mixed convection. Steady mixed convection was studied in two orientations. First with buoyancy in the same direction of the flow and second with buoyancy in the opposite direction. The transient data were for a ramp-down flow transient. This unsteady flow was repeated many times for ensemble-averaging of the results. In both cases, uncertainty was estimated in all of the results. Additionally, the transient case was simulated with CFD, matching inputs, and a validation study was performed.

An additional study was conducted to assess the accuracy of the commercial HFSs as they were believed to be in error. The air temperature was measured very close to the wall surface. The temperature gradient is proportional to heat flux, the rate of heat energy transfer over an area. Potential errors of this method were estimated and a thorough uncertainty study was performed. Additionally, a study was performed to identify the error source of the HFSs.

ACKNOWLEDGMENTS

The assistance, creativity, and trust of Dr. Barton L. Smith are what made this work possible. Also the assistance and example of Jeff Harris was quite inspiring. My colleagues in the Experimental Fluid Dynamics Lab over the years, who are too numerous to name without a high probability of forgetting at least one, are also to thank for the assistance in analysis and in friendship.

My family; especially my wife Rebekah with our children Jacob, Emily, and the little one on the way; was amazingly supportive and patient. The trust and encouragement of my parents inspired me from a young age towards higher education. I also thank my counselors and mentors in my youth for believing in me and giving guidance.

This research was performed using funding received from the U. S. Department of Energy Office of Nuclear Energy's Nuclear Energy University Programs. Also the scholarship and fellowship support of the U. S. Nuclear Regulatory Commission is greatly appreciated.

Blake W. Lance

CONTENTS

	Page
ABSTRACT	iii
PUBLIC ABSTRACT	v
ACKNOWLEDGMENTS	vii
LIST OF TABLES	xi
LIST OF FIGURES	xii
NOTATION	xiv
ACRONYMS	xvii
1 INTRODUCTION	1
1.1 The Very High Temperature Reactor	1
1.2 Computational Fluid Dynamics Validation	1
1.3 Mixed Convection	5
1.4 Transient Convection	7
1.5 Wall Heat Flux	8
References	10
2 EXPERIMENTAL VALIDATION DATA FOR CFD OF STEADY MIXED CONVECTION ON A VERTICAL FLAT PLATE	13
2.1 Introduction	13
2.1.1 Computational Fluid Dynamics Validation	14
2.1.2 Mixed Convection	16
2.2 Experimental Facility	19
2.2.1 Rotatable Buoyancy Tunnel	19
2.2.2 Test Section	20
2.3 Analog Instrumentation and Signal Processing	22
2.3.1 Thermal Instrumentation	23
2.3.2 Particle Image Velocimetry	24
2.3.3 TC Probe	26
2.3.4 Atmospheric Instrumentation	27
2.3.5 Uncertainty Quantification	27
2.4 Boundary Conditions	28
2.4.1 BC Description	28
2.4.2 BC Data	31
2.5 Fluid and Material Properties	32
2.6 Test Conditions	32
2.7 System Response Quantities	32
2.7.1 SRQ Description	33
2.7.2 SRQ Data	38
2.8 Conclusions	39
References	40

3	EXPERIMENTAL VALIDATION DATA FOR CFD OF TRANSIENT MIXED CONVECTION ON A VERTICAL FLAT PLATE	42
3.1	Introduction	42
3.1.1	Computational Fluid Dynamics Validation	43
3.1.2	Transient Flows	45
3.1.3	Mixed Convection	47
3.2	Experimental Facility	47
3.2.1	Rotatable Buoyancy Tunnel	48
3.2.2	Test Section	49
3.3	Analog Instrumentation and Signal Processing	52
3.3.1	Thermal Instrumentation	52
3.3.2	Particle Image Velocimetry	53
3.3.3	Atmospheric Instrumentation	55
3.3.4	Uncertainty Quantification	56
3.4	Boundary Conditions	56
3.4.1	BC Description	56
3.4.2	BC Data	58
3.5	Fluid and Material Properties	59
3.6	Test Conditions	59
3.7	System Response Quantities	60
3.7.1	SRQ Description	60
3.7.2	SRQ Data	63
3.8	Conclusions	63
	References	65
4	WALL HEAT FLUX MEASUREMENTS IN A CONVECTING BOUNDARY LAYER	67
4.1	Introduction	67
4.2	Theory	69
4.3	Method	71
4.4	Results	75
4.5	Conclusions	81
	References	81
5	CONCLUSIONS	83
	APPENDICES	84
A	Unsteady Computational Fluid Dynamics Simulations	85
A.1	Introduction	85
A.2	Methods	85
A.3	Results	86
A.4	Conclusions	89
B	Processing and Post-processing Codes	91
B.1	Introduction	91
B.2	Particle Image Velocity Uncertainty	92
B.3	Inlet Analysis	93
B.4	Boundary Condition Statistics	93
B.5	Interpolation Codes for Boundary Conditions	93
B.6	Virtual Origin	93
B.7	System Response Quantity Analysis	93
B.8	Transient Image Organization	94
B.9	Transient Computational Fluid Dynamics Grid Convergence Index	94
B.10	TC Probe Analysis	94
B.11	Custom Functions	94

C	Mixed Convection Parameters	95
D	Heated Wall Conduction Analysis	98
E	Permission Letter for Steady Mixed Convection Work	101
	References	103
	CURRICULUM VITAE	104

LIST OF TABLES

Table	Page
2.1 The tabulated boundary conditions and system response quantities provided in this work . . .	14
2.2 Re_x , Gr_x , and Ri_x at the three locations in x at the spanwise center where SRQ data were acquired. The bulk velocity \bar{u}_{bulk} was 2.44 m/s. These apply for both cases presented.	17
2.3 Heated wall components and thicknesses with names from Fig. 2.4	22
2.4 PIV data parameters. Aided refers to buoyancy-aided case while Opposed refers to buoyancy-opposed case.	25
2.5 Boundary layer analysis results	31
2.6 Links to temperature boundary files for both cases	31
2.7 Links to velocity SRQ files for both cases	39
3.1 The available experimental data presented in this work separated into BC and SRQ types . . .	43
3.2 Gr_x as well as Re_x and Ri_x at the initial condition at the three locations in x at the spanwise center where data were acquired	48
3.3 Heated wall components and thicknesses with names from Fig. 3.4	51
3.4 PIV data parameters	54
4.1 Parameters for the Design of Experiment study	74
4.2 Boundary layer analysis results from velocity data at the inlet	79
4.3 Heat flux results for both cases from the HFSs and the TC Probe results at all three x locations	81

LIST OF FIGURES

Figure	Page
1.1 Very High Temperature Reactor core, [4]	2
1.2 Difficulty Spectrum of SRQs, after [5]. The variables y and x here are arbitrary.	4
1.3 Validation Hierarchy, after [9]	4
1.4 Wall heat flux comparing measurements with two correlations	9
2.1 The Validation Hierarchy, after [6]	16
2.2 System Response Quantity Difficulty Spectrum, after [3]. The variables y and x are arbitrary.	16
2.3 RoBuT flow components in the buoyancy-aided orientation	20
2.4 Heated wall cross section with component names as in Table 2.3. The relative thicknesses are to scale.	21
2.5 Particle images at x_2	26
2.6 TC probe with its reflection in the heated wall on the right	27
2.7 Measured temperatures on the test section boundaries	29
2.8 Measured streamwise velocity \bar{u} at the inlet for the buoyancy-opposed case	29
2.9 Normalized streamwise mean velocity \bar{u} and Reynolds normal stress $\overline{u'u'}$ at three locations in x for both cases	33
2.10 Measured streamwise mean velocity \bar{u} and streamwise Reynolds normal stress $\overline{u'u'}$ with buoyancy-aided (Aid), buoyancy-opposed (Opp), and their difference (Diff) at three locations in x	34
2.11 Measured temperature profiles for all three x locations for the opposed case	35
2.12 Measured wall heat flux plotted along streamwise direction x with correlations for mixed convection for the buoyancy-aided (Aid), buoyancy-opposed (Opp), and their difference (Aid-Opp). Heat Flux Sensor results are labeled as HFS and correlation results as Corr.	36
2.13 Streamwise mean velocity \bar{u} near the heated wall with linear fit for shear stress measurement of the buoyancy-opposed case	37
2.14 Mean streamwise velocity \bar{u} with several repeats at three locations in x for both cases	38
2.15 Measured mean streamwise Reynolds stress $\overline{u'u'}$ with several repeats at three locations in x for both cases	38

2.16	Scatter of instantaneous u' and v' at the y -location of largest $\overline{u'u'}$ for both cases at x_2	39
3.1	The Validation Hierarchy, after [6]	45
3.2	System Response Quantity Difficulty Spectrum, after [3]. The variables y and x are arbitrary.	45
3.3	RoBuT flow components as configured for transient data acquisition	49
3.4	Heated wall cross section with component names as in Table 3.3. The relative thicknesses are to scale.	50
3.5	Dewarped SRQ particle image at x_2 with mean background removed. Note the image scales are about a factor of nine different.	55
3.6	Measured temperatures on the test section boundaries	57
3.7	Measured streamwise velocity \bar{u} at the inlet and the initial condition	57
3.8	Bulk velocity across the inlet at the spanwise center ($z = 0$) through time	60
3.9	The streamwise velocity \bar{u} and Reynolds normal stress $\overline{u'u'}$ at three locations in x and five phases of the transient	62
3.10	High-resolution PIV data near the heated wall with linear fit	63
3.11	The heated wall heat flux and wall shear stress plotted over time	64
4.1	Important flow components of the Rotatable Buoyancy Tunnel	68
4.2	Heated wall cross section with relative thicknesses to scale. The HFS label is near the top.	69
4.3	Wall heat flux measurements with two correlations	70
4.4	TC Probe with its reflection in the heated wall on the right	72
4.5	Self-alignment process of the TC Probe with the heated wall	72
4.6	Factorial sketch of the DOE study	75
4.7	Measured temperature profiles for both cases and all three x locations	75
4.8	Measured temperature profiles near the heated wall with line fit for both cases for all three x locations. Note the unique wall temperature values T_s as the wall is nearly isothermal. T_s at x_1 is several degrees cooler than at x_2 and x_3	76
4.9	Measured nondimensional temperature profiles with the thermal law of the wall for air for both cases and all three x locations	77
4.10	Measured and predicted heat flux plotted in the streamwise direction	80
4.11	Factorial sketch of the DOE study with errors	80
A.1	The structured rectangular mesh with 1M cells	86
A.2	The streamwise velocity \bar{u} and turbulent kinetic energy \bar{k} for both PIV and CFD results	87
A.3	The heated wall heat flux and wall shear stress plotted over time	89

NOTATION

Lowercase Roman

dt	Time delay of Particle Image Velocimetry image pairs
$f\#$	Lens aperture f-number
g	Acceleration due to gravity
k	Thermal conductivity
\bar{k}	Time mean turbulent kinetic energy
q''	Heat flux
t	Time or thickness
t_{95}	Confidence level coefficient at the 95% level
\bar{u}	Time mean streamwise velocity
\bar{u}_{bulk}	Time mean streamwise bulk velocity
\bar{u}_{∞}	Time mean streamwise free-stream velocity
u'	Instantaneous fluctuation of u
u_{τ}	Shear velocity
$\overline{u'u'}$	Time mean streamwise Reynolds stress
\bar{v}	Time mean wall-normal velocity
v'	Instantaneous fluctuation of v
$\overline{v'v'}$	Time mean wall-normal Reynolds stress
$\overline{u'v'}$	Time mean Reynolds shear stress
\bar{w}	Time mean transverse velocity
$\overline{w'w'}$	Time mean transverse Reynolds stress
x	Coordinate in streamwise direction
\bar{x}	Arbitrary time mean variable
y	Coordinate normal to the heated wall
y^+	Nondimensional coordinate normal to the heated wall
z	Coordinate in the transverse direction

Uppercase Roman

$B_{\bar{x}}$	Bias uncertainty of variable \bar{x}
---------------	--

D	Experimental data
D_{TC}	Diameter of thermocouple wire in probe
E	Validation error
Gr_x	Local Grashof number
N	Number of samples
Nu_F	Nusselt number of forced convection
Nu_x	Local Nusselt number
Pr	Prandtl number
Re_x	Local Reynolds number
Ri_x	Local Richardson number
S	Simulation result
S_x	Standard deviation of x
$S_{\bar{x}}$	Random uncertainty of \bar{x}
St	Stanton number
T	Temperature
T_{max}	Maximum wall temperature in the DOE study
T^+	Nondimensional temperature
T_∞	Temperature of free-stream
T_s	Temperature of surface
U_D	Uncertainty of experimental data
U_ε	Uncertainty of error
U_{input}	Uncertainty of simulation input
U_{num}	Uncertainty of numerics
$U_{q''}$	Uncertainty of heat flux
U_{val}	Uncertainty of validation
$U_{\bar{x}}$	Uncertainty of variable \bar{x}

Lowercase Greek

β	Thermal coefficient of expansion
δ_2	Momentum thickness of boundary layer
ε	Error
μ	Dynamic viscosity of air

ν	Kinematic viscosity of air
ρ	Density of air
τ_s	Shear stress at surface
ξ	Distance to virtual origin upstream of leading edge

Uppercase Greek

ΔT	Change in temperature
Δy	Change in coordinate y

ACRONYMS

BC	Boundary Condition
CFD	Computational Fluid Dynamics
CJC	Cold Junction Compensation
DAQ	Data Acquisition
DOE	Design of Experiments
FOV	Field of View
HFS	Heat Flux Sensor
IC	Initial Condition
INL	Idaho National Laboratory
LDA	Laser Doppler Anemometry
LOFC	Loss of Forced Convection
M&S	Modeling & Simulation
NI	National Instruments
NRC	U. S. Nuclear Regulatory Commission
PIV	Particle Image Velocimetry
PTU	Programmable Timing Unit
RANS	Reynolds-averaged Navier-Stokes
RoBuT	Rotatable Buoyancy Tunnel
SRQ	System Response Quantity
TC	Thermocouple
TTL	Transistor-Transistor Logic
UQ	Uncertainty Quantification
URANS	Unsteady Reynolds-averaged Navier-Stokes
USU	Utah State University
V&V	Verification & Validation
VHTR	Very High Temperature Reactor

CHAPTER 1

INTRODUCTION

The motivation for studying transient mixed convection in detail came from a possible accident scenario of a new nuclear power plant design. Computational Fluid Dynamics (CFD) is a means to numerically model complex flows with heat transfer and is a major tool for accessing nuclear reactor safety. With the approximations of CFD come the necessity to validate results. This is done by comparing with experimental data to assess whether the model accuracy is sufficient for the intended use. Experiments were conducted to provide detailed measurements of steady and transient mixed convection. This work is in multi-paper format with three unique chapters that are independent of each other for publication. Because of this, some sections are repeated for completeness.

1.1 The Very High Temperature Reactor

The Very High Temperature Reactor (VHTR) concept is a prominent Next Generation Nuclear Plant design under consideration whose reactor core is shown in Fig. 1.1. There are several advantages to this design including improved efficiency from increased temperatures between 900-950°C, passive safety features, potential for process heat or hydrogen production at co-located plants, and an increase from a 40 to 60 year license cycle. The VHTR uses helium gas as the coolant so high temperatures can be realized and efficiency increased. The main core design is either a prismatic core where most of the reactor core is graphite with coolant and fuel passages or a pebble bed core with fuel elements the size of tennis balls. In either design, normal operation has helium forced downward through the core [1, 2]. In the event of a Loss of Forced Convection (LOFC) that may result from a problem with the blower, viscous and buoyant forces initially decrease flow rate. As the blower and helium inertia decreases, buoyancy effects reverse the flow in a chaotic event. Ultimately steady natural convection upward is the final state. Natural convection is the primary mode of heat removal from the core in a Pressured Conduction Cooled event such as this. This phenomenon has been identified as one of high importance and low knowledge by the U.S. Nuclear Regulatory Commission (NRC) [3].

1.2 Computational Fluid Dynamics Validation

Computational methods have been used for many decades to assess reactor design safety in accident

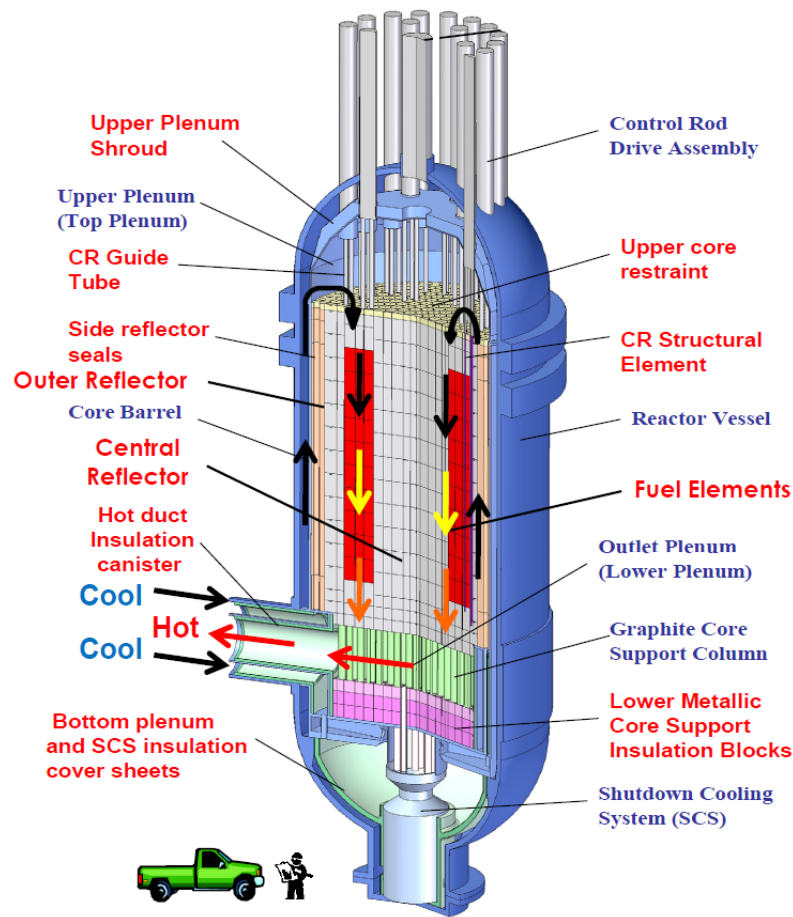


Fig. 1.1: Very High Temperature Reactor core, [4]

scenarios. Modern computational methods began in the 1960s with the programmable computer. Since that time, computational power has increased rapidly. At least over the last twenty years, the speed of the fastest supercomputer has increased by a factor of ten every four years [5]. With computational power increasing rapidly, more researchers and scientists are making use of Modeling & Simulation (M&S). Modeling and Simulation can be used to predict physical phenomena in fields of fluid dynamics, heat transfer, solid mechanics, genetics, finance, and many others where analytic solutions are impractical or impossible. Many M&S results are being used to make decisions, and some of them for high-consequence systems where public safety is of concern. The use of M&S was adopted early in the nuclear power industry for thermal-hydraulics safety codes to predict flow and heat transfer processes in accident scenarios as evidenced by the common use of system codes such as RELAP5.

With the increased use of M&S should also come improved means to assess simulation accuracy, especially for high-consequence systems. From this need, a discipline called Verification & Validation (V&V) emerged. The first of these, Verification, covers two main methods to determine software correctness, Code Verification and Solution Verification. There are several definitions of these terms that have been identified by different professional organizations to meet their individual needs. One of these is the American Society of Mechanical Engineers that defined these terms as [6]:

Verification: the process of determining that a computational model accurately represents the underlying mathematical model and its solution.

Validation: the process of determining the degree to which a model is an accurate representation of the real world from the perspective of the intended uses of the model.

The purpose of Code Verification is to assure software correctly implements the numerical algorithm and is free of programming errors or “bugs.” Solution Verification is the process of determining the accuracy of the simulation inputs, the accuracy of the solution, and that of the output. Validation is the means to determine how well the simulation predicts real-world behavior by comparing simulation results with experimental data [5]. Stating the definitions another way, verification is checking the math and has nothing to do with physics while validation only has to do with physics. Blottner stated these definitions in memorable terms as “Verification is solving the equations right” and “Validation is solving the right equations” [8]. The attitude in V&V is naturally skeptical and places higher demand on simulations than is common in practice [7].

Verification is solely the responsibility of those that develop models or *modelers*. Validation is a shared responsibility of modelers and experimentalists where the latter provide data that represent physical phenomena. The current work focuses on providing experimental data for validation activities.

The planning and execution of validation studies should include both modelers and experimentalists through all phases. In considering the design of validation systems, it is desirable to measure System Response Quantities (SRQs)—system outputs that are used for validation—from a wide range and high levels of difficulty as shown in Fig. 1.2. Comparing M&S results with experimental data from a wide range on the spectrum increases validation confidence. For example, integral quantities, such as fluid mass flow rate, generally have low experimental noise and random errors. Derivative quantities like fluid shear are more sensitive to non-ideal conditions. If a model and data are in good agreement at a high level, then it is likely that good agreement will be observed in lower levels. But, agreement at lower levels does not imply agreement at higher levels [5].

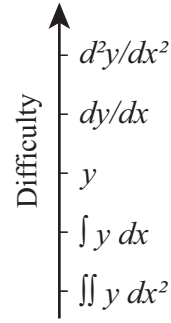


Fig. 1.2: Difficulty Spectrum of SRQs, after [5]. The variables y and x here are arbitrary.

There are several tiers or levels of validation studies as shown in Fig. 1.3. The levels range from the Complete System to Unit Problems. The Complete System is the highest tier and includes all relevant physics and geometry but for which measurements are coarse. Unit Problems have basic geometry and non-coupled physics with complete measurements but are far removed from the system. Different Complete Systems will appear very different from each other but often share many of the same phenomena of lower tiers, so lower-tiered validation studies may be useful for many systems [5].

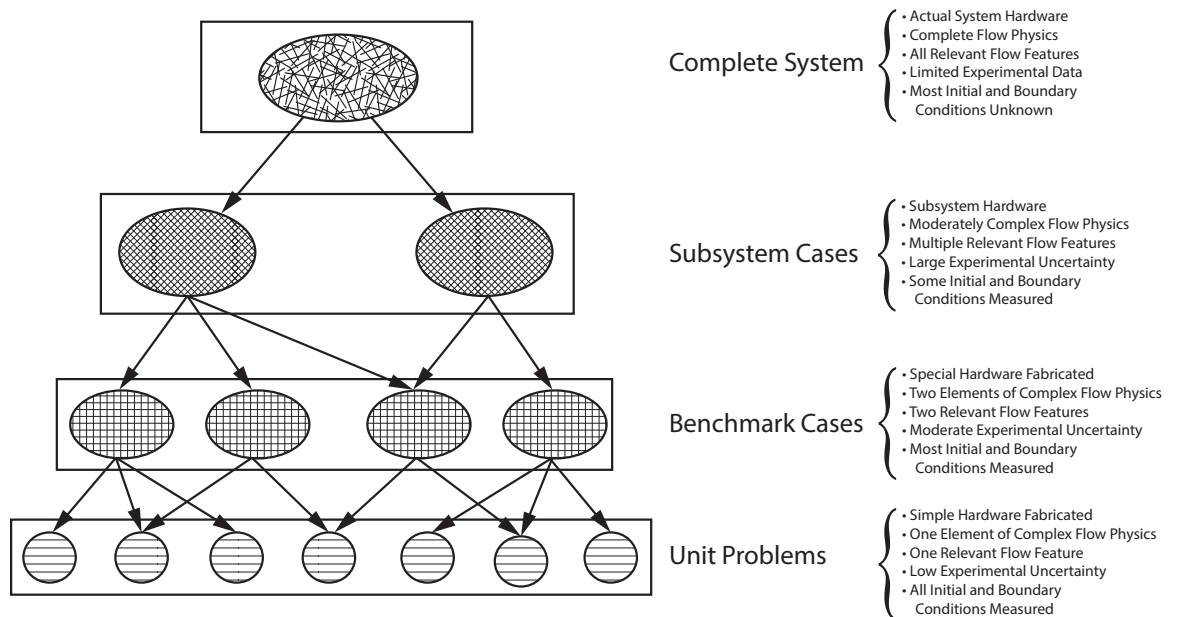


Fig. 1.3: Validation Hierarchy, after [9]

The Benchmark Tier, also called Separate Effects Testing, requires that most model inputs and many model outputs are measured and experimental uncertainty is included. This tier has specialized hardware, simplified geometry, and only some physics coupling [5]. The proposed work has coupled physics in fluid momentum and heat transfer as well as three-dimensional velocity development that keep it from being a Unit Problem. This Benchmark Case has simplified geometry and high detail of measurements and associated uncertainties make it useful for many systems.

There are several terms in common use that need to be defined in the context of validation. The domain of interest is the region in space and/or time where the physical phenomena being modeled occurs. This domain may have *boundary conditions* (BCs) where the external physical conditions are applied. It may also have *initial conditions* (ICs) which are a form of BC that exists at the initial time, but these conditions also extend into the domain of interest. Generally, experimental data are provided to the modeler in the form of BCs and/or ICs. The model output is called the *system response quantity of interest*, herein referred to as *system response quantity* or SRQ, and often there are several. The SRQ is either found within the domain of interest or at a boundary whose conditions are an output. It provides data to be used as a validation metric when assessing the accuracy of a model [5].

Generally, older experimental data from discovery experiments are not sufficiently described to be used for validation. Discovery experiments are common in research where new physical phenomena are measured, presented, and discussed. Validation experiments do not necessarily measure unique phenomena but the measurement process and description are more complete [10].

Several databases are available online for the purpose of CFD validation. An updated list of these is found at www.cfd-online.com/Links/refs.html. Data from many other sources are no longer available online as programs and technologies expire. The description associated with these databases is very light and rarely includes a complete set of necessary model inputs. Validation data should be highly described and regularly maintained by organizations that last longer than research programs to ensure the data are useful for as long as possible.

1.3 Mixed Convection

Mixed convection is a coupled fluid momentum and heat transfer phenomenon where both forced and natural convection contribute to the behavior. With forced convection, buoyant forces are negligible and flow is driven by a pressure gradient. Conversely, buoyant forces drive high density fluid above low density fluid [11].

There are generally three types of mixed convection that depend on the relative directions of buoyant and pressure forces. The first is *buoyancy-aided* where buoyant forces and forced flow have the same direction, the second *buoyancy-opposed* where these forces have opposite direction, and the third *transverse* where these forces are perpendicular [12].

Specifically mixed convection conditions are determined by the local Richardson number as

$$\text{Ri}_x = \text{Gr}_x / \text{Re}_x^2 \quad (1.1)$$

where

$$\text{Re}_x = \bar{u}_{\text{bulk}} x / \nu \quad (1.2)$$

and

$$\text{Gr}_x = g\beta(T_s - T_\infty)x^3 / \nu^2. \quad (1.3)$$

In these, g is acceleration due to gravity, β is fluid thermal coefficient of expansion, T_s and T_∞ are surface and fluid temperatures, respectively, x is local streamwise location, ν is fluid kinematic viscosity, and \bar{u}_{bulk} is time mean bulk velocity. Mixed convection is observed for buoyancy aided flow when $0.3 < \text{Ri}_x < 16$ and for $0.3 < \text{Ri}_x$ for opposed flow [11].

There have been many mixed convection studies on vertical plates and in vertical tubes. Several mixed convection experiments for vertical tubes are cited in a review article by Jackson *et al.* [13]. They surveyed literature and presented results for both laminar and turbulent flows, both theoretical and experimental studies. Results were compared and heat transfer correlations presented. They noted that heat transfer in buoyancy-aided turbulent flow is suppressed for moderate buoyancy levels while, on the other hand, it is augmented in buoyancy-opposed flows. This work provides heat transfer correlations for pipe flow that could be useful for comparison with the current work. They further recommend the use of Low Re models for mixed convection simulations.

Chen *et al.* [14] present correlations for laminar mixed convection on vertical, inclined, and horizontal plates and compare them to experiments performed by Ramachandran *et al.* [15]. Experiments of the latter provided point velocity and temperature measurements via a hot-wire anemometer. The data agreed very well with predictions and were sufficient for comparison to correlations with, but are not reported in sufficient detail for validation.

Kim *et al.* [16] summarize simulations that predict mixed convection in a vertical tube and compare the models to experimental data. The in-house code used published two-equation models and was written

to model developing mixed convection flow with variable properties. Consistent with previous works, laminarization of the turbulent flow was reported in the buoyancy-aided case and increased turbulent levels in the opposed case. None of the models investigated showed good agreement over the entire range of flow, suggesting further model development, or perhaps model calibration, could increase prediction capability for these flows.

Wang *et al.* [17] discuss both an experimental and a numerical study of a vertical plate under turbulent mixed convection. Two-component Laser Doppler Anemometry (LDA) was used to measure boundary layer velocity. Some temperature measurements were also made of the flow using a thermocouple (TC) rake. They reported moderate agreement between experimental data and simulation results, but noted that predictions for the buoyancy-opposed case were less accurate. Although this study provides valuable insight into this flow with plate geometry, the reported information lacks boundary conditions necessary for validation studies.

Mixed convection literature is abundant. However, all the papers found were performed as discovery experiments, not for the purpose of providing validation data. Most are for pipe flow, boundary and initial conditions are lacking, uncertainties are rarely presented, flow geometry description is simplified, and fluid properties are seldom given. Further, the techniques used were often intrusive, leading to unknown uncertainties, and often provided only point measurements. Modern measurement systems can provide higher fidelity data while disrupting the flow less.

1.4 Transient Convection

Transient convection is of consequence in a LOFC accident of the VHTR as the flow starts with forced convection downward and changes to natural convection upward in a ramp-type flow transient. Some studies of non-periodic transient flow have been performed, but as He & Jackson [18] note, it has only been somewhat recently that technology has allowed for comprehensive measurements of ensemble-averaged transient experiments. Most of the first experiments measured either temperature of tube walls or velocity, not both. A common observation was that accelerating flow suppresses turbulence while decelerating flow augments it.

The first work by Koshkin *et al.* was published in 1970 for turbulent air flow and reported measurements when changing electrical power and different flow transients, measuring and reporting temperature measurements [19]. Two similar studies were published in the 1970s and used electrochemical techniques with probes to measure velocity profiles inside a tube from a step change in flow rate [20, 21].

A study performed by Rouai where heat transfer experiments on ramp-up and ramp-down transients as well as periodic pulsating flow with a non-zero time mean were performed. Water was heated by passing

an alternating electrical current through a stainless steel tube. Temperature measurements were made by 24 thermocouples welded to this tube. Flow transients were prescribed by using a constant head tank and varying the flow through the test section by a valve. Wall heat flux remained constant and changes in wall temperature were measured. The observed Nusselt number departed more from the pseudo-steady values for faster transients and for decelerating flows, likely from the augmentation of turbulence [22].

Two researchers, He & Jackson, performed experiments in water using two-component LDA measurements in a clear, unheated tube. This non-intrusive velocity measurement was one of the first known for non-periodic flows. Ensemble-averaged results were used for mean and turbulent quantities. The turbulent results were original for this type of flow and were shown to deviate from pseudo-steady results for short transients. Several non-dimensional parameters were recommended for ramp-type transients [18].

In the previous studies, no coupling of velocity and thermal measurements was found for transients and buoyancy effects were negligible. Also, as these were discovery experiments, boundary conditions were not measured and provided as tabulated data, making the results of limited use for validation. The facility description is very basic and flow geometries simplified. The current study contributes high fidelity measurements of a ramp-down transient suitable for validation studies with simultaneous, non-intrusive velocity and thermal measurements to provide validation data on simplified geometry for three-dimensional simulations.

1.5 Wall Heat Flux

As will be discussed later in this work, the experimental facility test section was highly instrumented. Three thin-film heat flux sensors (HFSSs) were purchased and potted in the heated wall for heat flux measurements. Being commercial sensors from RdF Corp., they came with factory-calibrated sensitivities. Preliminary experiments have shown that the measured heat flux does not match fundamental trends as shown in Fig. 1.4, specifically decreasing heat flux with boundary layer development with increasing x . Two correlations are shown. The Kays trend is the heat flux from

$$St = \frac{Nu_x}{Re_x Pr} = \frac{0.0287 Re_x^{-0.2}}{0.169 Re_x^{-0.1} (13.2 Pr - 9.25) + 0.85} \quad (1.4)$$

where St is the Stanton number, Nu_x is the local Nusselt number, and Pr is the Prandtl number [11]. The Incropera trend is based on the correlation for convection over an isothermal flat plate [12] and is

$$Nu_x = 0.0296 Re_x^{4/5} Pr^{1/3}. \quad (1.5)$$

Once the Nusselt number is computed, heat flux is calculated as $q'' = \text{Nu}_x k (T_s - T_\infty) / x$ where q'' is heat flux and k is fluid thermal conductivity. Note that the correlation trends are not smooth, a result of the measured center-line plate temperature, which has small gradients.

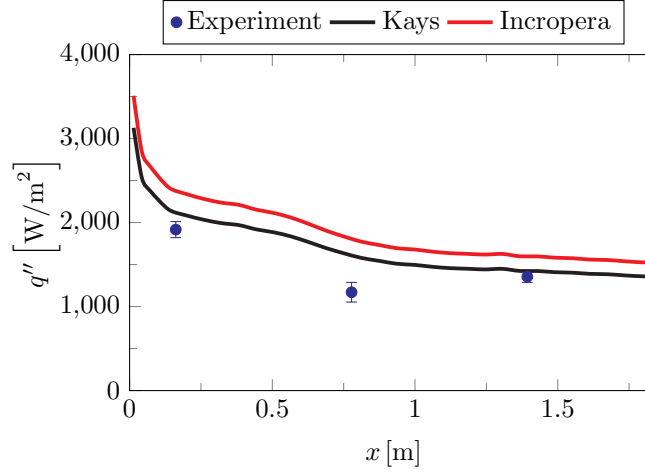


Fig. 1.4: Wall heat flux comparing measurements with two correlations

The difference in these trends was concerning and it was possible that the sensor sensitivities were mixed-up, had an installation error, or other manufacturer-supplied parameters were incorrect. As heat flux was a critical SRQ, developing a means to assess sensor accuracy was desired. Since the sensors were permanently potted, removing them for calibration was not an option. In situ heat flux measurements were made via an independent method. This method should not change heat transfer conditions in the area.

Installation error was possible if heat transfer conditions are different between calibration and use. The RdF sensors were calibrated to a reference sensor that was calibrated at 70°F in radiation using a blackbody source [23]. The heat transfer mode of the sensors in the heated wall was conduction. The different heat transfer modes, the elevated operation temperature, and the possibility of non-uniform thermal resistance in the sensor area have been identified as possible error sources [24].

There are several methods for heat flux calibration. The National Institute of Standards and Technology is an excellent source for heat flux sensor calibration services. They use a variable-temperature blackbody thermal radiation source with symmetric conditions for simultaneous measurements with a reference optical pyrometer and a user-supplied HFS [25]. This method was impractical for the current situation as the sensors could not be removed.

One common HFS design measured the temperature difference across a substrate of known thermal conductivity using a thermopile (array of thermocouples in series for increased output) [26]. Fourier's Law for conduction was the theory of this measurement and is [12]

$$q'' = -k \frac{dT}{dy} \approx -k \frac{\Delta T}{\Delta y} \quad (1.6)$$

where k is substrate thermal conductivity, T is temperature, and y is the direction of heat flux. This method was used in the purchased RdF thin-film sensors potted in the plate. Adding a reference HFS of this type would disrupt local convection conditions. The calorimeter method uses heat storage over time to measure flux [26], but this would change local conditions for the proposed experiment. The facility geometry and thermal resistance must remain constant in space.

An independent heat flux measurement technique was possible. The potted HFSs measured heat flux near the surface of the heated wall. The convective heat flux from the wall to the air should be equivalent, especially very near the wall and removed from the side walls. Very near the heated wall, within the viscous sublayer, the temperature profile is linear [11]. If the temperature profile can be measured within this region and the thermal conductivity of air k can be estimated by the measured temperature and reference data found in [27], it is possible to measure convective heat flux from a surface.

Others have made near-wall temperature measurements. An early study by Warner and Arpaci described the use of a butt-welded TC probe of 12.7 μm diameter oriented parallel to a vertical flat plate and perpendicular to the flow direction. It was traversed with a motor-driven carriage near the heated wall under turbulent natural convection. The position was accurate to 5.08 μm within the first 25.4 mm and to 15.2 μm farther from the wall. They were able to measure temperature profiles and subsequently heat flux [28]. In another study of a turbulent boundary layer under forced convection, temperature profiles were measured by a TC probe of 76.2 μm diameter and about 12.7 mm long suspended by 22-gauge hypodermic needles oriented parallel to the plate and perpendicular to the flow direction. This probe was also traversed with a traversing mechanism accurate to 25.4 μm . These results, along with velocity measurements, were used to present many heat flux, shear, and turbulent Prandtl number results for this fundamental flow [29].

References

- [1] U. S. Department of Energy, 2010, "Next Generation Nuclear Plant: A Report to Congress," Tech. rep., U. S. Department of Energy Office of Nuclear Energy.

- [2] Oh, C., Kim, E., Schultz, R., Patterson, M., Petti, D., and Kang, H., 2010, “Comprehensive Thermal Hydraulics Research of the Very High Temperature Gas Cooled Reactor,” *Nuclear Engineering and Design*, **240**(10), pp. 3361–3371, doi:[10.1016/j.nucengdes.2010.07.007](https://doi.org/10.1016/j.nucengdes.2010.07.007).
- [3] Woods, B. G., Jackson, R. B., and Nelson, B. L., 2009, “Scaling Analysis for the Very High Temperature Reactor Test Facility at Oregon State University,” Tech. rep., Oregon State University.
- [4] Idaho National Laboratory, *Module 05a Prismatic HTGR Core Design Description*, https://inlportal.inl.gov/portal/server.pt/community/ngnp_public_documents.
- [5] Oberkampf, W. L., and Roy, C. J., 2010, *Verification and Validation in Scientific Computing*, Cambridge University Press, doi:[10.1017/cbo9780511760396](https://doi.org/10.1017/cbo9780511760396).
- [6] ASME, 2006, *Guide for Verification and Validation in Computational Solid Mechanics*, ASME Standard V&V 10-2006, New York, NY.
- [7] Tetlock, P., 2005, *Expert Political Judgment: How Good Is It? How Can We Know?*, Princeton University Press, Princeton, NJ.
- [8] Blottner, F. G., 1990, “Accurate Navier-Stokes Results for the Hypersonic Flow Over a Spherical Nosedip,” *Journal of Spacecraft and Rockets*, **27**(2), pp. 113–122, doi:[10.2514/3.26115](https://doi.org/10.2514/3.26115).
- [9] AIAA, 1998, “Guide for the Verification and Validation of Computational Fluid Dynamics Simulations,” Tech. Rep. AIAA G-077-1998, American Institute of Aeronautics and Astronautics, Reston, VA, doi:[10.2514/4.472855](https://doi.org/10.2514/4.472855).
- [10] Roache, P. J., 2009, *Fundamentals of Verification and Validation*, Hermosa Publ.
- [11] Kays, W. M., Crawford, M. E., and Weigand, B., 2012, *Convective Heat and Mass Transfer*, 4th ed., McGraw-Hill.
- [12] Incropera, F. P., Dewitt, D. P., Bergman, T. L., and Lavine, A. S., 2007, *Fundamentals of Heat and Mass Transfer*, 6th ed., John Wiley & Sons.
- [13] Jackson, J. D., Cotton, M. A., and Axcell, B. P., 1989, “Studies of Mixed Convection in Vertical Tubes,” *International Journal of Heat and Fluid Flow*, **10**(1), pp. 2–15, doi:[10.1016/0142-727x\(89\)90049-0](https://doi.org/10.1016/0142-727x(89)90049-0).
- [14] Chen, T. S., Armaly, B. F., and Ramachandran, N., 1986, “Correlations for Laminar Mixed Convection Flows on Vertical, Inclined, and Horizontal Flat Plates,” *Journal of Heat Transfer*, **108**(4), p. 835, doi:[10.1115/1.3247020](https://doi.org/10.1115/1.3247020).
- [15] Ramachandran, N., Armaly, B. F., and Chen, T. S., 1985, “Measurements and Predictions of Laminar Mixed Convection Flow Adjacent to a Vertical Surface,” *Journal of Heat Transfer*, **107**(3), p. 636, doi:[10.1115/1.3247471](https://doi.org/10.1115/1.3247471).
- [16] Kim, W. S., Jackson, J. D., He, S., and Li, J., 2004, “Performance of a Variety of Low Reynolds Number Turbulence Models Applied to Mixed Convection Heat Transfer to Air Flowing Upwards in a Vertical Tube,” *Proceedings of the Institution of Mechanical Engineers, Part C: Journal of Mechanical Engineering Science*, **218**(11), pp. 1361–1372, doi:[10.1177/095440620421801107](https://doi.org/10.1177/095440620421801107).
- [17] Wang, J., Li, J., and Jackson, J., 2004, “A Study of the Influence of Buoyancy on Turbulent Flow in a Vertical Plane Passage,” *International Journal of Heat and Fluid Flow*, **25**(3), pp. 420–430, doi:[10.1016/j.ijheatfluidflow.2004.02.008](https://doi.org/10.1016/j.ijheatfluidflow.2004.02.008).
- [18] He, S., and Jackson, J. D., 2000, “A Study of Turbulence Under Conditions of Transient Flow in a Pipe,” *Journal of Fluid Mechanics*, **408**, pp. 1–38, doi:[10.1017/s0022112099007016](https://doi.org/10.1017/s0022112099007016).

- [19] Koshkin, V., Kalinin, E., Dreitser, G., Galitseisky, B., and Izosimov, V., 1970, “Experimental Study of Nonsteady Convective Heat Transfer in Tubes,” *International Journal of Heat and Mass Transfer*, **13**(8), pp. 1271–1281, doi:[10.1016/0017-9310\(70\)90068-2](https://doi.org/10.1016/0017-9310(70)90068-2).
- [20] Kataoka, K., Kawabata, T., and Miki, K., 1975, “The Start-up Response of Pipe Flow to a Step Change in Flow Rate,” *Journal of Chemical Engineering of Japan*, **8**(4), pp. 266–271, doi:[10.1252/jcej.8.266](https://doi.org/10.1252/jcej.8.266).
- [21] Maruyama, T., Kuribayashi, T., and Mizushima, T., 1976, “The Structure of the Turbulence in Transient Pipe Flows,” *Journal of Chemical Engineering of Japan*, **9**(6), pp. 431–439, doi:[10.1252/jcej.9.431](https://doi.org/10.1252/jcej.9.431).
- [22] Rouai, N. M., 1987, “Influence of Buoyancy and Flow Transients on Turbulent Convective Heat Transfer in a Tube,” Ph.D. thesis, University of Manchester, UK.
- [23] RdF, 2014, “Heat Flow Measurement: Calibration, Specifications & Accuracy,” Tech. rep., RdF, corp.
- [24] Holmberg, D. G., and Womeldorf, C. A., 1999, “Performance and Modeling of Heat Flux Sensors in Different Environments,” ASME Heat Transfer Division, pp. 71–77.
- [25] Tsai, B. K., Gibson, C. E., Murthy, A. V., Early, E. A., Dewitt, D. P., and Saunders, R. D., 2004, “NIST Measurement Services: Heat-Flux Sensor Calibration,” Tech. Rep. Special Publication 250-65, National Institute of Standards and Technology.
- [26] Diller, T. E., 1999, *The Measurement, Instrumentation, and Sensors Handbook*, chap. 34, Heat Flux, CRC Press.
- [27] Touloukian, Y. S., Liley, P. E., and Saxena, S. C., 1970, “Thermophysical Properties of Matter-The TPRC Data Series. Volume 3. Thermal Conductivity-Nonmetallic Liquids and Gases,” Tech. rep., DTIC Document.
- [28] Warner, C. Y., and Arpaci, V. S., 1968, “An Experimental Investigation of Turbulent Natural Convection in Air at Low Pressure Along a Vertical Heated Flat Plate,” *International Journal of Heat and Mass Transfer*, **11**(3), pp. 397–406, doi:[10.1016/0017-9310\(68\)90084-7](https://doi.org/10.1016/0017-9310(68)90084-7).
- [29] Blackwell, B. F., Kays, W. M., and Moffat, R. J., 1972, “The Turbulent Boundary Layer on a Porous Plate: an Experimental Study of the Heat Transfer Behavior with Adverse Pressure Gradients,” Tech. Rep. HMT-16, The National Aeronautics and Space Administration.

CHAPTER 2

EXPERIMENTAL VALIDATION DATA FOR CFD OF STEADY MIXED CONVECTION ON A VERTICAL FLAT PLATE¹

Abstract

Model validation for Computational Fluid Dynamics (CFD), where experimental data and model outputs are compared, is a key tool for assessing model uncertainty. In this work, mixed convection was studied experimentally for the purpose of providing validation data for CFD models with a high level of completeness. Experiments were performed in a facility built specifically for validation with a vertical, flat, heated wall. Data were acquired for both buoyancy-aided and buoyancy-opposed flows. Measured boundary conditions include as-built geometry, inflow mean and fluctuating velocity profiles, and inflow and wall temperatures. Additionally, room air temperature, pressure, and relative humidity were measured to provide fluid properties. Measured system responses inside the flow domain include mean and fluctuating velocity profiles, temperature profiles, wall heat flux, and wall shear stress. All of these data are described in detail and provided in tabulated format.

2.1 Introduction

The purpose of this work is to provide validation data for three-dimensional Computational Fluid Dynamics (CFD) models. Model validation will be discussed as well as the physical phenomenon of steady mixed convection. The following sections describe the experimental facility, the associated instrumentation, the boundary conditions (BCs), the fluid and material properties, the test conditions, and the System Response Quantities (SRQs). This content follows the Validation Experiment Completeness table of Oberkampf and Smith [1] to guide description of validation experiments. This guidance ensures important details are included with a high level of completeness. The work contained herein is a continuation of that by Harris *et al.* [2] which covered forced convection using similar methods and facilities.

This work presents the data in table format for direct use in validating models. The provided data include the BCs and SRQs shown in Table 2.1. The included BCs in this work should provide modelers with all required information, avoiding assumptions on model inputs and reducing model form uncertainty [3].

¹Authors: Blake W. Lance, Jeff R. Harris, and Barton L. Smith

The SRQ data are provided to modelers for direct comparison with model outputs. The experimental uncertainties of all provided data from bias and random sources are also provided and quantified at the 95% confidence level. Validation errors can be calculated with the nominal data and validation uncertainty from the uncertainty of the nominal data [4].

Table 2.1: The tabulated boundary conditions and system response quantities provided in this work

BCs	SRQs
As-built geometry	Mean velocity profiles
Wall & inflow temps.	Fluctuating velocity profiles
Inflow mean velocity	Mean temperature profiles ¹
Inflow fluctuating velocity	Wall heat flux
Atmospheric conditions	Wall shear stress

These files are accessible in an online database in the Digital Commons of Utah State University’s Library. The page dedicated to the data in this work is found at digitalcommons.usu.edu/all_datasets/8/. Links to specific files are included in this work with descriptive file names with the experimental case (buoyancy-aided or buoyancy-opposed), data type (BC or SRQ), and measured quantity included. All data files may be downloaded in the zipped file [Data](#). Generally, data are in table format as csv files.

2.1.1 Computational Fluid Dynamics Validation

To understand the need for experiments expressly aimed at providing validation data, one must first understand the different aims of validation and discovery experiments. Discovery experiments are common in research where new physical phenomena are measured, presented, and discussed. Validation experiments do not necessarily measure unique phenomena, but the measurement process and description are more complete [5]. In general, older experimental data from discovery experiments are not sufficiently described for use in validation. Unobtrusive measurement techniques are important in validation experiments since probes introduce unknown uncertainties to the data. These uncertainties can only be mitigated by including the probe in the CFD model.

The purpose of validation experiments is to provide the information required to quantify the uncertainty of a mathematical model. This uncertainty helps decision makers quantify model credibility. The ASME V&V 20 Standard [4] outlines an approach to estimate the validation comparison error and the validation

¹The SRQ mean temperature profiles are provided for the buoyancy-opposed case only.

uncertainty. The validation error E is the difference between the simulation result S and the validation experiment result D as

$$E = S - D. \quad (2.1)$$

Calculating the validation uncertainty estimates the confidence interval of the error by considering both numerical and experimental uncertainty. Validation uncertainty is calculated as

$$U_{\text{val}} = \sqrt{U_{\text{num}}^2 + U_{\text{input}}^2 + U_D^2}, \quad (2.2)$$

where U_{num} is the numerical uncertainty, U_{input} is the model input uncertainty, and U_D is the experimental data uncertainty. The numerical uncertainty is estimated from solution verification with sources such as iterative and discretization uncertainty. The latter two uncertainties come from the validation data. The uncertainty in the measured BCs that are used for model inputs is U_{input} . The uncertainty of SRQs—experimental data used to compare system outputs—is U_D . If $|E| \gg U_{\text{val}}$, one can conclude model error remains. But if $|E| \leq U_{\text{val}}$ and U_{val} is acceptably small for the intended use of the model, the validation error may be satisfactory. These general equations show validation data and their uncertainties are required to assess model accuracy via model validation.

There are several tiers of detail in validation experiments [6], often four as shown in Fig. 2.1. This work is considered a Benchmark Case that is second in simplicity to Unit Problems. The Benchmark Case, also called Separate Effects Testing, requires that all model inputs and most model outputs are measured and that experimental uncertainty is included. In this tier there is generally some level of multi-physics interaction, such as coupled fluid momentum and heat transfer, that prevents this work from being considered a Unit Problem. On the other hand, the non-prototypical geometry used in this work keeps it from being a Subsystem Case.

The planning and execution of validation studies should include both modelers and experimentalists through all phases. In considering the design of validation systems, SRQs should be measured from a wide range and high difficulty in the difficulty spectrum as shown in Fig. 2.2. Comparing simulation results with experimental data from a wide range on the spectrum increases validation confidence. For example, integral quantities, such as fluid mass flow rate, generally have low experimental noise and random errors. Derivative quantities like fluid shear are more sensitive to non-ideal conditions. If a model and data are in good agreement at a high level, then it is likely that good agreement will be observed in lower levels. But, agreement at lower levels does not imply agreement at higher levels [3].

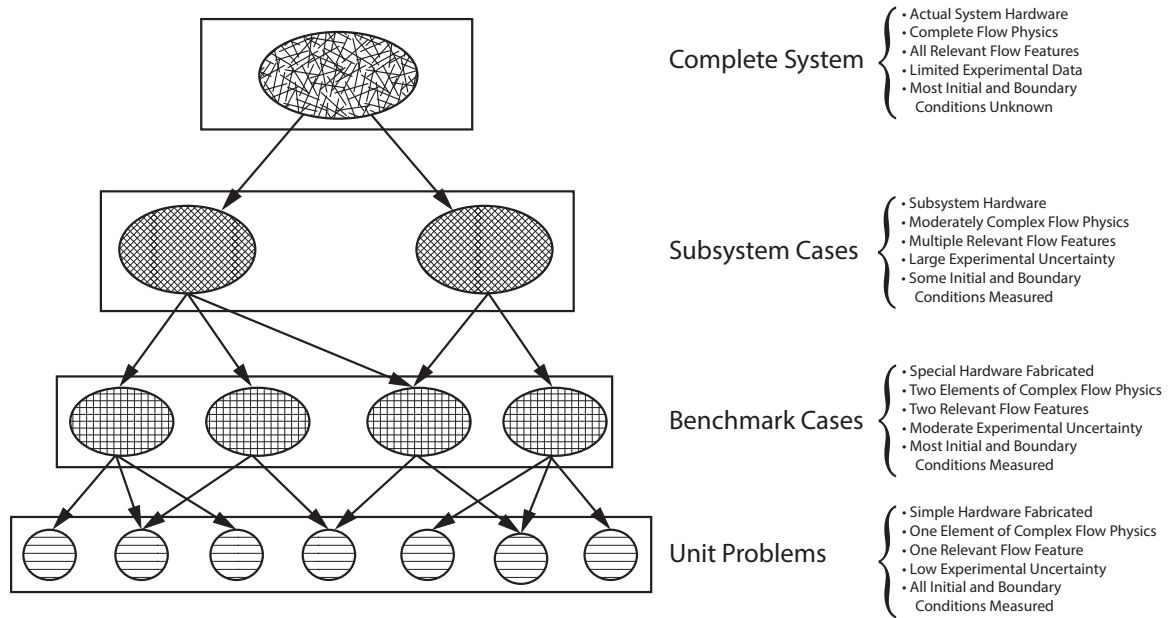
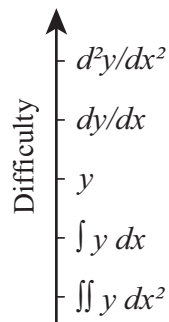


Fig. 2.1: The Validation Hierarchy, after [6]

Fig. 2.2: System Response Quantity Difficulty Spectrum, after [3]. The variables y and x are arbitrary.

2.1.2 Mixed Convection

Mixed convection is a coupled fluid momentum and heat transfer phenomenon where both forced and natural convection contribute to behavior. With forced convection, buoyant forces are negligible and flow is driven by a pressure gradient. Conversely, buoyant forces drive natural convection in the direction opposite to gravity as low density fluid rises over higher density fluid [7].

There are generally three types of mixed convection that depend on the relative direction of buoyant and pressure forces. The first is *buoyancy-aided*, where buoyant forces and forced flow have the same direction.

The second is *buoyancy-opposed*, where these forces have opposite directions. Finally the third is *transverse*, where these forces are perpendicular [8].

The mixed convection regime is defined by the local Richardson number as

$$\text{Ri}_x = \text{Gr}_x / \text{Re}_x^2 \quad (2.3)$$

where

$$\text{Re}_x = \bar{u}_{\text{bulk}} x / \nu \quad (2.4)$$

and

$$\text{Gr}_x = g\beta(T_s - T_\infty)x^3 / \nu^2. \quad (2.5)$$

In these equations, g is acceleration due to gravity, β is fluid thermal coefficient of expansion, T_s and T_∞ are surface and fluid temperatures respectively, x is local streamwise location, ν is fluid kinematic viscosity, and \bar{u}_{bulk} is bulk time mean velocity. Mixed convection is commonly thought to occur for buoyancy-aided flow when $0.3 < \text{Ri}_x < 16$ and for buoyancy-opposed flow when $0.3 < \text{Ri}_x$ [7].

Some flow parameters in this study are given in Table 2.2. Note that external coordinates are used because the flow was not fully developed in the test section as it would be for pipe flow. The flow at x_1 was not in the mixed convection regime; but, as will be shown, buoyancy effects are still observable. The temperature of the heated wall was near the safety limit of the materials, and the air velocity was near the low side of the turbulent regime (large turbulent trips were installed upstream of the test section to enforce boundary layer turbulence at these lower Reynolds numbers).

Table 2.2: Re_x , Gr_x , and Ri_x at the three locations in x at the spanwise center where SRQ data were acquired. The bulk velocity \bar{u}_{bulk} was 2.44 m/s. These apply for both cases presented.

	x [m]	Re_x	Gr_x	Ri_x
x_1	0.16	13,000	1.55×10^7	0.09
x_2	0.78	63,000	1.73×10^9	0.43
x_3	1.39	110,000	9.93×10^9	0.77

There have been many mixed convection studies on vertical plates and in vertical tubes. Some will be described now. Several mixed convection experiments for vertical tubes are cited in a review article by Jackson *et al.* [9]. They surveyed literature and presented results for both laminar and turbulent flows, both theoretical and experimental studies. Results were compared and heat transfer correlations presented. They

noted that heat transfer in buoyancy-aided turbulent flow is suppressed for moderate buoyancy levels while, on the other hand, it is augmented in buoyancy-opposed flows. This work provides heat transfer correlations for pipe flow that could be useful for comparison with the current work. They further recommend the use of Low Re models for mixed convection simulations.

Chen *et al.* [10] present correlations for laminar mixed convection on vertical, inclined, and horizontal plates and compare them to experiments performed by Ramachandran *et al.* [11]. Experiments of the latter provided point velocity and temperature measurements via a hot-wire anemometer. The data agreed very well with predictions and were sufficient for comparison to correlations with, but are not reported in sufficient detail for validation.

Kim *et al.* [12] summarize simulations that predict mixed convection in a vertical tube and compare the models to experimental data. The in-house code used published two-equation models and was written to model developing mixed convection flow with variable properties. Consistent with previous works, laminarization of the turbulent flow was reported in the buoyancy-aided case and increased turbulent levels in the opposed case. None of the models investigated showed good agreement over the entire range of flow, suggesting further model development, or perhaps model calibration, could increase prediction capability for these flows.

Wang *et al.* [13] discuss both an experimental and a numerical study of a vertical plate under turbulent mixed convection. Two-component Laser Doppler Anemometry (LDA) was used to measure boundary layer velocity. Some temperature measurements were also made of the flow using a thermocouple (TC) rake. They reported moderate agreement between experimental data and simulation results, but noted that predictions for the buoyancy-opposed case were less accurate. Although this study provides valuable insight into this flow with plate geometry, the reported information lacks boundary conditions and inflow parameters necessary for validation studies.

Mixed convection literature is abundant. However, all the papers found were performed as discovery experiments, not for the purpose of providing validation data. Most are for pipe flow, boundary and initial conditions are lacking, uncertainties are rarely presented, flow geometry description is simplified, and fluid properties are seldom given. Further, the techniques used were often intrusive, leading to unknown uncertainties, and often provided only point measurements. Modern measurement systems can provide higher fidelity data while disrupting the flow less.

2.2 Experimental Facility

All experiments were performed in the Rotatable Buoyancy Tunnel (RoBuT), which will be described in detail. Benchmark-level validation data were acquired with simple geometry and some multi-physics interaction. The square test section allowed easy characterization using optical velocity measurements. The simple geometry is easy to represent numerically and helps isolate model errors.

2.2.1 Rotatable Buoyancy Tunnel

The RoBuT was an open-circuit air tunnel with a large 4.81-m diameter ‘Ferris wheel’ design that allowed rotation, thus changing the relative direction of forced flow and buoyant forces without changing the facility. Many important tunnel components are shown in Fig. 2.3, which is in the buoyancy-aided orientation. Note the coordinate system with the origin on the heated wall at the inlet and the spanwise center. The streamwise distance is x , wall-normal distance is y , and spanwise distance is z with zero along the centerline. The laser and camera were part of a Particle Image Velocimetry (PIV) system that will be described in Sec. 2.3.2.

The test section had a 0.305×0.305 m square cross section and was 2 m long. It had three clear walls for optical access and a heated wall for a thermal BC. More details of the test section are provided in Sec. 2.2.2. The contraction and outlet were made of fiberglass-reinforced plastic with a glass-smooth, black gel-coat.

The contraction had an area ratio of 6.25:1 and was 0.914 m long. The contraction bell at the leading edge had a 102 mm radius. Between the contraction and bell were four modular sections that contained—in order of flow direction—a single row, aluminum fin/copper tube, chilled water heat exchanger (Super Radiator Coils Model 30x30-01R-0.625/048); a settling length section; a precision aluminum honeycomb flow straightener; and two high porosity screens. Square turbulence trips 3.175 mm wide were installed along all four walls and located about 0.12 m upstream of the test section inlet.

The outlet expanded the flow downstream of the test section, had a total included angle of 8.2° , and was 0.686 m long. The blower drew air through the test section and rejected it into the room. It included an inline centrifugal fan assembly, TCF/Aerovent model 14-CBD-3767-5. It was belt driven by a 5 HP, TEFC, 230-460 VAC induction motor, Toshiba model B0052FLF2AMH03. The motor was powered by a Toshiba variable frequency drive, model VFS11-2037PM-WN.

Two Laskin Nozzles [14] were used to atomize olive oil tracer particles. These were measured to have a mean diameter of about $1\mu\text{m}$ with a TSI Aerodynamic Particle Size Spectrometer at the outlet. These particles were mixed with air and injected into a PVC pipe distribution system upstream of the contraction

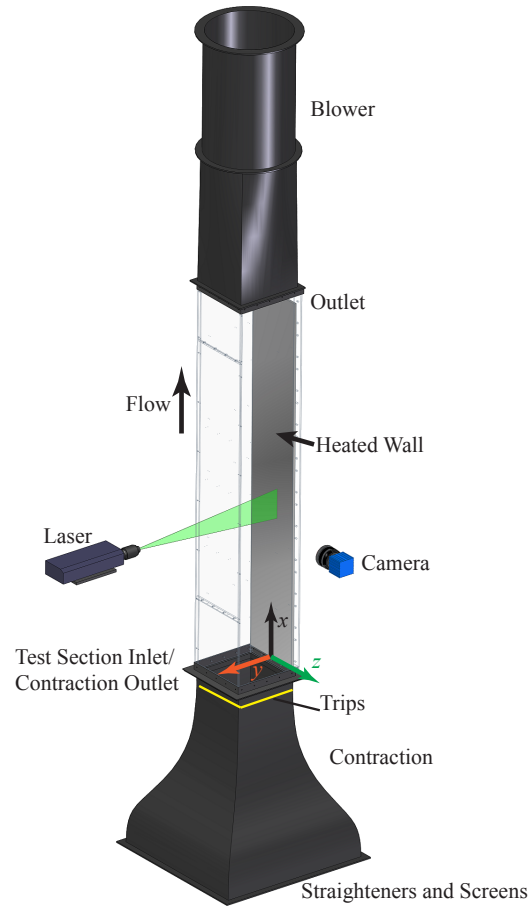


Fig. 2.3: RoBuT flow components in the buoyancy-aided orientation

assembly. A peg board was placed between this system and the beginning of the contraction to help mix particles throughout the flow. It had holes 6.35 mm in diameter and were spaced 25.4 mm apart in a square pattern.

2.2.2 Test Section

The test section had four walls, an inlet, and an outlet that will be described in detail. The heated wall was custom designed with many layers to provide a heated surface for convection and featured embedded instrumentation. Its cross section is shown in Fig. 2.4. This wall was heated to approximately 138°C for this study. It was made of several layers of aluminum, had six silicon rubber heaters arranged in the streamwise direction, and contained thermal insulation to drive most of the heat inward. A list of materials and thicknesses is available in Table 2.3. The surface was nickel plated to reduce thermal radiation which resulted

in a predicted and measured emissivity around 0.03 [2]. Aluminum 2024, though more expensive than the common alloy 6061, was used because its thermal conductivity is well known [15]. The heated portion was 279 mm wide and 1.89 m long. The left and right sides were thermally insulated by 17.5-mm thick Teflon[®] that extended into grooves in the side walls. Two additional 12.7-mm thick Teflon[®] insulators were placed upstream and downstream of the heated wall. There were six heaters, each spanning the width of the heated wall and one sixth of the length. Three HP 6439B power supplies were connected to two heaters each and were used to control the temperature of the wall via a closed-loop PI controller. Three controllers, one for each power supply, allowed the heated wall to be heated in independent sections in the streamwise direction to increase temperature uniformity.

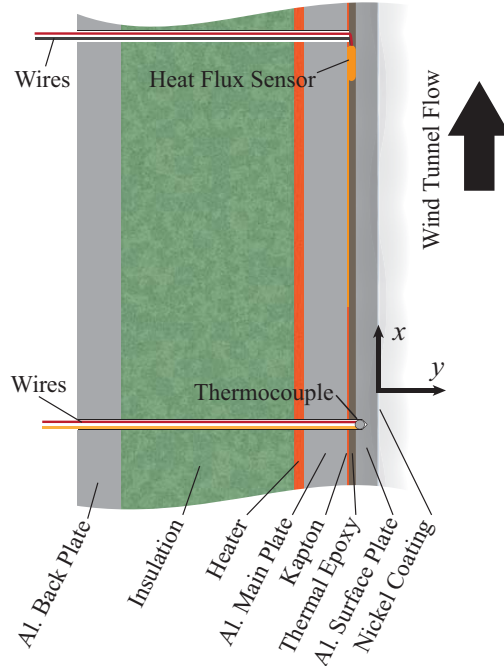


Fig. 2.4: Heated wall cross section with component names as in Table 2.3. The relative thicknesses are to scale.

The other three walls were clear Lexan[®] polycarbonate for optical access and were 12.7 mm thick. From the perspective of standing on the heated wall at the inlet, they are termed left ($z=-152$ mm), top ($y=305$ mm), and right ($z=152$ mm) walls. The top wall had a removable center portion for cleaning and maintenance. This wall also had three 25.4-mm ports for probe insertion that were used for the TC probe described in Sec. 2.3.3.

The as-built geometry was measured to compensate for differences between the as-designed and as-built

Table 2.3: Heated wall components and thicknesses with names from Fig. 2.4

Name	Material	t [mm]
Nickel Coating	Bright Nickel	~ 0.05
Al. Surface Plate	Al. 2024-T3	3.18
Thermal Epoxy	Dow Corning 3-6751	1.02
Kapton [®]	Kapton [®] HN Film	0.254
Al. Main Plate	Al. 6061-T651	6.35
Heater	Tempco Silicone Rubber	1.59
Insulation	Mineral Wool	25.4
Al. Back Plate	Al. 6061-T651	6.35

test section geometry. The differences were small, but the measurements are presented for completeness. An internal micrometer was used to measure the internal dimensions of the fully assembled test section. Height measurements were performed at the left, center, and right as well as width measurements at the top, middle, and bottom. This was done at seven locations in x and performed three times for a measure of random uncertainty. Modelers may use these dimensions when constructing the simulation domain to ensure greater similarity. A sketch of the measurement locations may be accessed from the online database by the link [All-BC-AsBuiltSketch](#) in the digital version of this work. The nominal values are in [All-BC-AsBuiltMeasurements](#) and uncertainties in [All-BC-AsBuiltMeasurementUncertainties](#). A Parasolid model created from the as-built measurements is available in [All-BC-AsBuiltGeometry](#).

A warm-up procedure was followed each time the RoBuT was used for experiments. Ideally, the HVAC system would be kept active at all times for stable room conditions. The heated wall was first heated to the setpoint temperature. Once this was reached, the blower was set to the desired speed for the experiment and the heater controllers would accordingly increase power. Once the temperature was again stable for at least five minutes, the facility was ready for data acquisition. If the blower setpoint speed was changed, the controller would stabilize temperature and a waiting period was repeated for at least five minutes.

Between data acquisition for the different cases, such as between the aided and opposed cases, the entire test section was cleaned with Ethyl Alcohol and delicate task wipes to ensure optical quality. The cover on the top wall was removed for inside cleaning. High-vacuum grease was used on test section joints to reduce air leakage and was removed and reapplied each time a panel of the test section was adjusted.

2.3 Analog Instrumentation and Signal Processing

Validation experiments require high fidelity instrumentation. Thermocouples were used to measure boundary temperatures, heat flux sensors (HFSs) for heat flux through the heated wall, and PIV for inflow

and boundary layer air velocity. Other sensors measured room air conditions. These systems will now be described in detail.

2.3.1 Thermal Instrumentation

A total of 307 TCs were used to measure boundary temperatures. All test section TCs were 30 gauge Type K from Omega Engineering with Special Limits of Error. They were each welded to length with an Argon-shielded welder. Each TC was calibrated with an Isotherm FASTCAL-M with an accuracy of 0.3°C over a range of $25\text{--}190^{\circ}\text{C}$ with data at every 5°C . Because every TC calibration was very similar and made from the same spool, an average calibration curve was applied. An array of 3×5 TCs, three in y and five in z , was suspended on the downstream side of the honeycomb for inlet air temperature measurements. Each of the three clear walls had 21 TCs with seven rows spaced in x and three across in y for the left and right walls or in z for the top wall. The bulk of the heated wall had 5×32 TCs with five in z and 32 in x . The Teflon[®] edges each had embedded TCs with five across the leading edge in z and 32 along the sides in x . All TCs were embedded to within 3.18 mm of the inside surface using thermal epoxy with enhanced thermal conductivity.

Three HFSs were embedded into the heated wall along the spanwise center at the x -locations found in Table 2.2. They were model 20457-3 from RdF Corporation and were a thin-film type with a thermopile around a Kapton[®] substrate. The manufacturer supplied unique calibration coefficients for each sensor. The manufacturer-specified uncertainty was 5% of reading. An embedded Type T TC was used to measure sensor temperature and correct readings with the supplied multiplication factor curve to compensate for changes in thermal conductivity of the substrate. The HFSs were placed adjacent to the Kapton[®] layer of similar thermal resistance to reduce measurement errors. A thermal resistance network analysis showed only a 2.4% difference in heat flux between HFS and non-HFS conduction paths.

The TC and HFS output voltages were small, so special data acquisition (DAQ) devices were selected. National Instruments (NI) products were used as they interfaced well with the LabVIEW software that was used for system control and thermal data recording. Twenty one NI-9213 TC modules were housed in five NI-cDAQ-9188 chassis. The narrow voltage range of ± 78 mV, 24-bit ADC, and open channel detection made them well suited for these measurements. The built-in CJC was used for TCs. The total uncertainty of the calibrated TCs with these DAQs was 1°C , largely attributable to the CJC uncertainty of 0.8°C . Data from thermal instrumentation was recorded on-demand. Twelve sets of instantaneous measurements were recorded, one to accompany every set of PIV data for each case.

2.3.2 Particle Image Velocimetry

The PIV system allowed for non-intrusive, full-field velocity measurements at several locations. The system consisted of a laser, camera, and timing unit. The laser was a New Wave Research Solo PIV III. It was a dual cavity, frequency-doubled Nd:Yag model with about 22 mJ/pulse and a wavelength of 532 nm. Two LaVision camera designs were used as equipment was upgraded: an Imager Intense CCD camera for buoyancy-aided data and an Imager sCMOS for buoyancy-opposed data. The former had a 12-bit CCD sensor with 1376×1040 pixels and a pixel size of $6.45 \mu\text{m}$. The latter had a 16-bit sCMOS sensor with 2560×2160 pixels and a pixel size of $6.5 \mu\text{m}$. An internal, LaVision standard version PTU 9 timing unit provided accurate timing of the system and had a resolution of 10 ns and jitter of <1 ns. Two Nikon lenses were used: one AF Nikkor 28 mm f/2.8 D for the large field of view inflow and one AF Micro-Nikkor 105 mm f/2.8 D for high resolution SRQ data near the heated wall.

Images were acquired with LaVision DaVis 8.1 software and processed with DaVis 8.2. The optical configuration of the system is shown in Fig. 2.3 with the laser sheet normal to the heated wall and camera viewing angle parallel with it. The equipment was moved manually in the x direction. The inflow was measured in the same configuration with Velmex BiSlide[®] traverses to move the laser and camera consistently in the z direction. In this way, nine planes were measured to map the inflow.

PIV calibration was performed in two ways. The inflow used a conventional two-component ‘ruler’ calibration over a span of about 280 mm since the laser sheet and camera were normal to each other. The SRQ data near the heated wall was calibrated with a single-plane calibration target and the pinhole model as the camera was angled into the wall by $3\text{-}5^\circ$. This angle was required to avoid image diffraction by the large temperature gradient very near the wall. Because this flow had very little through-plane motion, errors in v velocity from through-plane motion appearing as in-plane motion are expected to be small (they are a function of the sine of the angle). The pinhole model was applicable since refraction between the Lexan[®] and air was also small.

Prior to acquisition, the quality of the particle images was checked to ensure proper particle density, diameter, and displacement as well as laser beam overlap and image focus quality. Many of these data parameters and others from the acquired images are found in Table 2.4. The diameter, density, and displacement are spatial averages over the entire image. Both particle diameter and density were determined by methods found in [16] with the local maximum method for density estimation.

The processing of particle images was performed with the window deformation method in DaVis. A mask was carefully defined to remove the influence of walls on the correlation. Round interrogation windows

Table 2.4: PIV data parameters. Aided refers to buoyancy-aided case while Opposed refers to buoyancy-opposed case.

Parameter	Aided-Inlet	Opposed-Inlet
N image pairs	500	1000
sample frequency [Hz]	4	10
dt [μ s]	1000	750
lens	28 mm	28 mm
extension [mm]	–	–
calibration [mm/pixel]	0.223	0.124
$f\#$	5.6	11
diameter [pixels]	1.45	1.39
density [$\#$ / 32×32]	70.8	19.3
displacement [pixels]	11.4	15.7
Parameter	Aided-SRQ	Opposed-SRQ
N image pairs	1000	1000
sample frequency [Hz]	4	10
dt [μ s]	76	62–65
lens	105 mm	105 mm
extension [mm]	39.5	39.5
calibration [mm/pixel]	0.0116	0.0103
$f\#$	5.6	11
diameter [pixels]	3.98–4.89	3.07–3.16
density [$\#$ / 32×32]	6.36–8.99	4.76–8.47
displacement [pixels]	13.8	12.2

were used for reduced noise. The first two passes were at 64×64 pixels and 75% overlap and the final four passes were at 32×32 pixels and 75% overlap. Vector post-processing was performed where vectors were removed if the peak ratio was less than two. Then a two-pass median filter of ‘strongly remove & iteratively replace’ corrected spurious vectors. Vectors were removed if their difference from average was more than one standard deviation of neighbors and subsequently replaced if the difference from average was less than two standard deviations of neighbors.

Particle images had a sliding background removed where the background is the average of nine images symmetrically taken around the image of interest. The pixel range was sometimes narrowed in the flow direction to reduce disk space while keeping at least 512 pixels in this direction. Examples of particle images with background subtracted for both orientations acquired with two cameras are shown in Fig. 2.5. Note that the heated wall is on opposite sides since the tunnel orientation was changed between cases. Also, the buoyancy-aided case used the Imager Intense camera with fewer pixels than the sCMOS used in the buoyancy-opposed case.

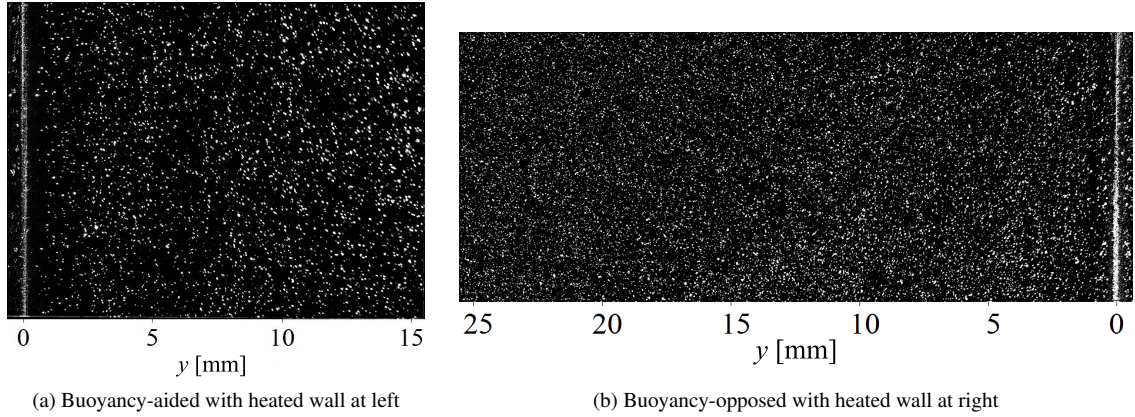


Fig. 2.5: Particle images at x_2

2.3.3 TC Probe

In order to provide an additional SRQ, it was necessary to measure the fluid temperature in the boundary layer. Since the RoBuT is an open-loop air tunnel with a large volume flow rate, optical measurement techniques requiring specialized particles are not practical. Thus, a TC probe was designed similar to that used in [17] with care taken to reduce the size and subsequent disruption of the flow. As this probe was intrusive and changed the flow, it was used after acquiring all other types of data so that its influence is only seen on the measured temperature profiles.

The junction of the probe was formed by type K wires of diameter $D_{TC} = 0.051$ mm from Omega Engineering. The two lead wires are aligned parallel to the wall with a length of 15.3 mm ($\sim 300D_{TC}$) to reduce conduction losses as shown in Fig. 2.6. The junction was formed by spot welding the overlapped wires. After welding, the wire was pulled taut and epoxied in place. The fine wire was welded to thicker 0.511-mm wire that spanned the pivot and was connected to the DAQ. The brace shown in Fig. 2.6 was rigid enough to keep the wire tight. To correct for small misalignments that could cause measurement errors, a pivot was designed into the probe so it could be aligned with the wall before each measurement. This was done by moving the probe into the wall until both ends of the brace were pressed firmly and any angle corrected, then pulling the probe away from the wall. This probe was measured with the same NI-9213 TC modules described in Sec. 2.3.1 and was used in the spanwise center of the tunnel.

The probe may be subject to conduction losses that could lead to measurement error. This error was estimated using a 1-D fin equation. The measured temperature and velocity profiles were used to estimate fluid properties and heat transfer coefficients. Heat conduction was considered from the TC junction to the leads and then convecting to the lower temperature air. The largest error was estimated at 0.03°C at the wall

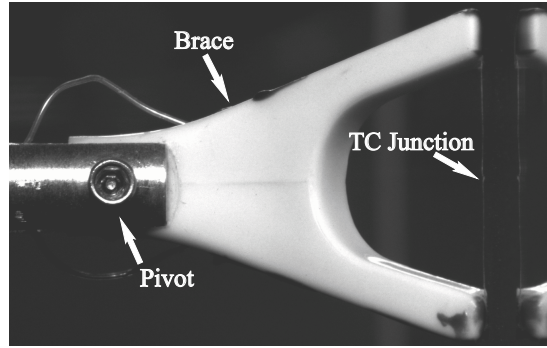


Fig. 2.6: TC probe with its reflection in the heated wall on the right

at x_1 .

This TC probe assembly was supported by a stainless steel tube with 3.76-mm outside diameter that spanned the test section. This tube contained the TC wires and was connected to a Velmex Inc. UniSlide® traverse model B4015Q2J. This traverse was used for small, incremental movements. The distance from the wall was estimated by fitting a line to the temperature profile very near the wall to the wall temperature measured by embedded TCs. The largest uncertainty in position resulted from the stepper motor resolution. With 200 steps/rev. and an assumed 1/2 step resolution, the uncertainty was 2.5 μm . The pitch uncertainty was much smaller at 0.04 mm/25.4 cm or 0.0315 μm for a 200 μm step.

2.3.4 Atmospheric Instrumentation

Air temperature, relative humidity, and atmospheric pressure in the RoBuT room were measured to determine air properties. Both temperature and humidity were measured with an Omega HX93A probe. Pressure was measured with an Apogee Instruments BPS 1006 sensor. The output voltage of these sensors was measured by a NI USB-9215A 4-channel ± 10 V analog input DAQ. The uncertainty of temperature was 0.6°C, humidity was 2.5% for readings 20-80% and 3.1% otherwise, and pressure was 3% of reading. These data were sampled at 1 Hz, then averaged and recorded once per minute.

2.3.5 Uncertainty Quantification

Thermal and atmospheric data uncertainty quantification (UQ) is described here following methods of Coleman and Steele [18]. UQ for PIV was considered by other methods and is described later. Bias uncertainty parameters were obtained from sensor documentation at the 95% confidence level. The random

uncertainty of a general mean quantity \bar{x} was calculated by

$$S_{\bar{x}} = t_{95} \frac{S_x}{\sqrt{N}} \quad (2.6)$$

where t_{95} is the confidence level coefficient (taken as 1.96 for 95% confidence and number of samples $N > 30$) and S_x is the sample standard deviation. Bias and random sources are combined as

$$U_{\bar{x}} = \sqrt{B_{\bar{x}}^2 + S_{\bar{x}}^2} \quad (2.7)$$

where $B_{\bar{x}}$ is the expanded bias uncertainty. The data provided with this paper generally specifies the unique bias, random, and total uncertainty numbers with the mean results.

Uncertainty of the PIV results was calculated from the Uncertainty Surface Method that estimates instantaneous bias and random uncertainties due to the effects of particle displacement, particle image density, particle image size, and shear. This method was originally described in [19] and improved on with methods from [16]. The uncertainties of the velocity statistics propagated from the instantaneous uncertainties were calculated by methods of Wilson & Smith [20]. Total uncertainty was calculated as in Eqn. 2.7. The confidence level on all UQ results in this work is 95%.

2.4 Boundary Conditions

This section contains a description of all expected requisite BCs for CFD model inputs. The types of BCs were shown in Table 2.1. The as-built geometry is a BC, but was discussed previously in Sec. 2.2.2.

2.4.1 BC Description

The measured BC temperatures are mapped onto the test section geometry in Fig. 2.7. Note the high measurement resolution on the heated wall and the development of the thermal boundary layer on the right wall as air travels from the inlet to the right of the figure.

As mentioned previously, the inflow was measured in nine planes spaced in z with points concentrated near the side walls. The time-mean streamwise velocity \bar{u} at the inlet is shown in Fig. 2.8 for the buoyancy-opposed case. Gray lines indicate PIV measurement locations that span across y . Data are highly-resolved in y but not in z . Data may be interpolated from the information given. Another approach is to use the high-resolution data near the unheated top wall ($y=305$ mm) boundary layer to the left and right walls which are also unheated.

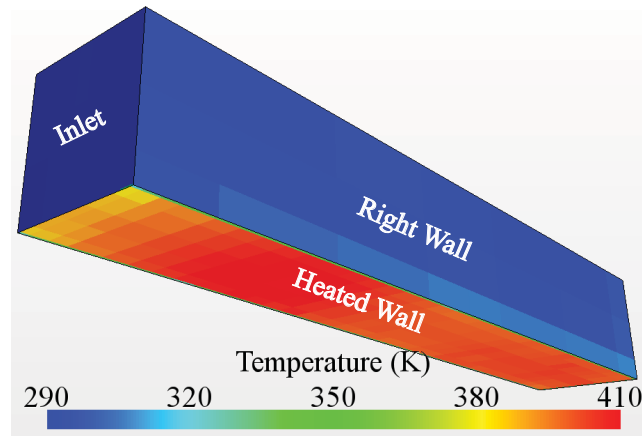


Fig. 2.7: Measured temperatures on the test section boundaries

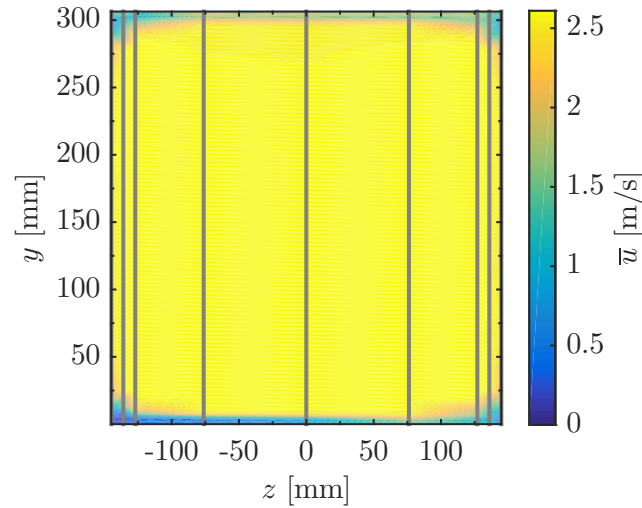


Fig. 2.8: Measured streamwise velocity \bar{u} at the inlet for the buoyancy-opposed case

The atmospheric conditions include atmospheric pressure, relative humidity, and room temperature and were recorded at the time of data acquisition.

Data acquisition procedures were followed to control test conditions. The following list describes the steps followed for acquisition of both BC and SRQ data:

1. Begin heating of the heated wall
2. Upon reaching setpoint temperature, start blower
3. Align traverses, laser, and camera with test section at measurement location

4. Align laser sheets
5. Focus camera on particle images
6. Align calibration plane with laser sheet and calibrate camera
7. Determine optimal dt for particle displacement, proper seeding density, and proper laser intensity
8. Record measurement location and other PIV parameters
9. Confirm stability of wall temperature and room conditions
10. Record PIV data, atmospheric and thermal conditions

This process was repeated for PIV measurement locations for the nine inflow and the three SRQ data sets. Inflow data were acquired in a single day, so only the last three steps were repeated after the first set. Data for PIV were recorded at twelve locations (nine at the inlet and three along the heated wall). Atmospheric conditions and thermal measurements were recorded with each PIV data set.

Since the velocity at the inlet is partially developed, some external flow parameters are included. The momentum thickness was measured from PIV data at the spanwise center ($z = 0$) location using the integral

$$\delta_2 = \int_0^\infty \frac{\bar{u}}{\bar{u}_\infty} \left(1 - \frac{\bar{u}}{\bar{u}_\infty} \right) dy \quad (2.8)$$

where \bar{u}_∞ is the free-stream velocity and constant density has been assumed [7]. The boundary layers on both walls were considered from $y = 0 - 0.305$ m and the result divided by two. Constant density is a good approximation at the inlet but not for downstream locations where the near-wall air was heated.

The concept of a virtual origin may also help predict the equivalent length of a flat plate extending upstream of the inlet. This allows for the impact of the contraction to be assessed. Assuming the flow was always turbulent, others have determined the relationship [7]

$$\frac{\delta_2}{x} = \frac{0.036\nu^{0.2}}{\bar{u}_\infty^{0.2}x^{0.2}} = 0.036\text{Re}_x^{-0.2}. \quad (2.9)$$

The left two portions can be arranged to isolate x as in

$$\xi = \frac{\delta_2^{1.25}\bar{u}_\infty^{0.25}}{0.0157\nu^{0.25}} \quad (2.10)$$

where ξ has been substituted for x and is the distance upstream to a virtual origin given δ_2 defined earlier. The results from these analyses are given in Table 2.5. It is reasonable to add these virtual origin distances to the x values in Table 2.2 when comparing to more canonical flows. Also Re_x and subsequently Ri_x numbers may also be adjusted. As will be presented, it is reasonable that the buoyancy-opposed case had a larger boundary layer at the inlet in this low speed flow as this case showed larger layers downstream.

Table 2.5: Boundary layer analysis results

Parameter	Aided	Opposed
δ_2 [mm]	1.61	1.81
ξ [mm]	417	485

2.4.2 BC Data

These data are available for both the buoyancy-aided and opposed cases on the inflow and all four walls of the test section. There is one file for the measured temperature of each surface that can be found in Table 2.6. The files may be opened by the links in the digital version. The format for all BC files works directly with Star-CCM+ and is easily adaptable to other CFD codes. The columns X, Y, and Z are used throughout this work; adhere to the global coordinates; and are presented in meters. The column ‘T[K]’ is the mean temperature in Kelvin, ‘B-T[K]’ is the bias uncertainty, ‘S-T[K]’ is the random uncertainty, and ‘U-T[K]’ is the total uncertainty.

Table 2.6: Links to temperature boundary files for both cases

Aided	Opposed
Aid-BC-InletTemp	Opp-BC-InletTemp
Aid-BC-HeatedWallTemp	Opp-BC-HeatedWallTemp
Aid-BC-LeftWallTemp	Opp-BC-LeftWallTemp
Aid-BC-TopWallTemp	Opp-BC-TopWallTemp
Aid-BC-RightWallTemp	Opp-BC-RightWallTemp

The data for the inflow mean and fluctuating velocities are found in the files [Aid-BC-Inlet-Vel](#) and [Opp-BC-Inlet-Vel](#). The columns ‘u’, ‘v’, and ‘w’ are mean velocities in the x , y , and z directions respectively. The columns ‘u’u’, ‘v’v’, ‘w’w’, and ‘u’v’ are specific Reynolds stresses. Uncertainties of \bar{u} , \bar{v} , and \bar{w} compose

the remaining columns. Reynolds stresses have unique upper and lower uncertainties with ‘Uuup’ being the plus uncertainty of $\overline{u'u'}$ and so on. The units of velocity and velocity uncertainty are [m/s] while those of Reynolds stresses and their uncertainty are [m²/s²].

Note that inflow out-of-plane velocities \overline{w} and $\overline{w'w'}$ were assumed to be the same as \overline{v} and $\overline{v'v'}$ respectively. This assumption was proved valid in previous work in this facility by measuring the inflow in both directions with two-component PIV and comparing data where measurement planes intersect [2]. Buoyancy-aided inflow data for the plane nearest the right wall was questionable and replaced with data nearest the left wall. As the geometry and thermal conditions are symmetric about $z = 0$, this was considered justified.

The atmospheric measurements, together with their uncertainties, are found in the files [Aid-BC-AtmCond](#) and [Opp-BC-AtmCond](#).

2.5 Fluid and Material Properties

As air is the working fluid, measurements of temperature, pressure, and relative humidity discussed in Sec. 2.4.2 are satisfactory to define all fluid properties. It is important to note that the working pressure is different from that at sea level as the experiment was conducted in Logan, Utah, which is 1460 meters above sea level.

Material properties of the test section can easily be obtained from the information provided in Sec. 2.2.2 about the construction of the test section. It is not necessary to model the heated wall since temperature measurements were made very near the surface, but the information is provided for completeness.

2.6 Test Conditions

The RoBuT room was configured with modern HVAC systems and thermal insulation for stable conditions. Controls were independent of other systems in the building. The refrigerated air conditioning had a $\sim 0.56^\circ\text{C}$ (1°F) deadband. The maximum measured temperature spread for both cases near the inflow location during data acquisition is 0.7°C ($\sim 1.3^\circ\text{F}$). To reduce the rate of temperature change from the on/off behavior of this system, outside air was mixed with refrigerated air before being injected into the room. Heating was performed with a steam heat exchanger with attached fan. The original fan and control system were replaced with a variable speed, tuned, PI-controlled system implemented with the main LabVIEW program, giving the heating system tight control of the room temperature.

2.7 System Response Quantities

The SRQs are the experimental results used to compare with simulation outputs and were listed in

Table 2.1. Since they are similar, the mean velocity profiles and fluctuating velocity profiles in the form of Reynolds stresses are presented together. Temperature profiles from the TC probe are presented for the opposed case. Additionally, scalars of wall heat flux and wall shear stress are also provided.

2.7.1 SRQ Description

Normalized streamwise velocity and Reynolds stress for the buoyancy-aided and buoyancy-opposed cases are shown in Fig. 2.9 for three measurement locations in x . The bulk velocity $\bar{u}_{\text{bulk}} = 2.44$ m/s measured across the inlet is used for normalization. The profile locations correspond to the vertical center of the camera sensor for reduced perspective error. Uncertainty bands are provided on both profiles that are unique for each data point. In other words, the uncertainty of $\bar{u}/\bar{u}_{\text{bulk}}$ and $\overline{u'u'}/(\bar{u}_{\text{bulk}})^2$ varies over y .

The influence of buoyancy is apparent in several regards. The boundary layer velocity and Reynolds stress is nearly constant for all x in the buoyancy-aided case, indicating little growth in the boundary layer thickness. The buoyancy-opposed case, however, shows rapid boundary layer growth. Also apparent is evidence of laminarization in the aided case and the augmentation of Reynolds stresses for the buoyancy-opposed case typical of mixed convection flows as described in previous works [9, 12].

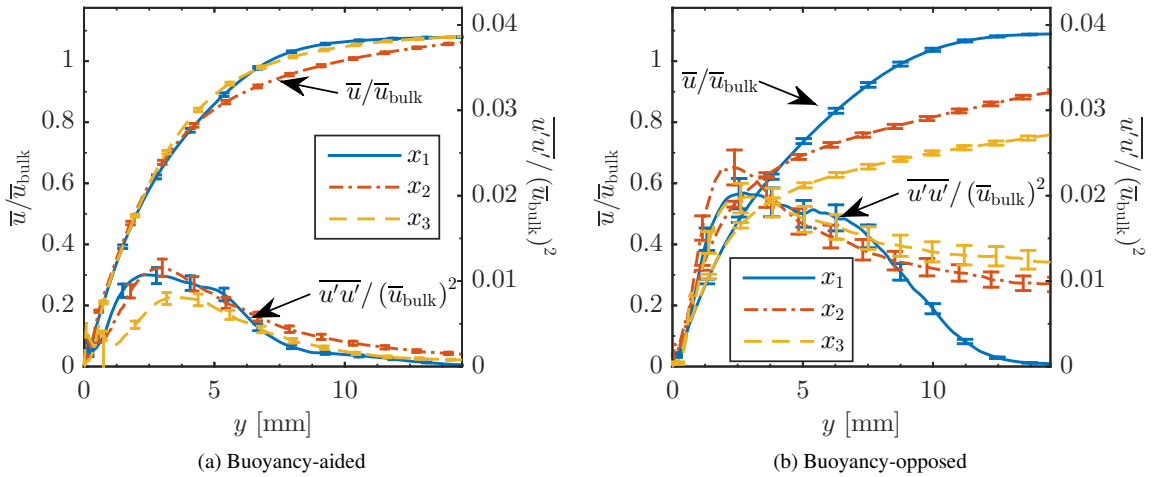


Fig. 2.9: Normalized streamwise mean velocity \bar{u} and Reynolds normal stress $\overline{u'u'}$ at three locations in x for both cases

The difference in the two cases reveals the influence of buoyancy on streamwise velocity and streamwise Reynolds normal stress. This is shown in Fig. 2.10. In these plots, the difference is labeled Diff and is the buoyancy-aided (Aid) minus the buoyancy-opposed (Opp) results. Buoyancy effects accelerate the boundary

layer velocity, but this influence is localized near the heated wall. As in the findings of other researchers in mixed convection, turbulence levels as quantified by $\overline{u'u'}$ are increased for the opposed case. Here the difference is about a factor of two. There is a subtle two-peak nature to $\overline{u'u'}$ that is most apparent in their difference at x_1 . This may be caused by the 3.175-mm-wide turbulence trips that are upstream of the test section, especially considering that this profile feature dies out farther downstream.

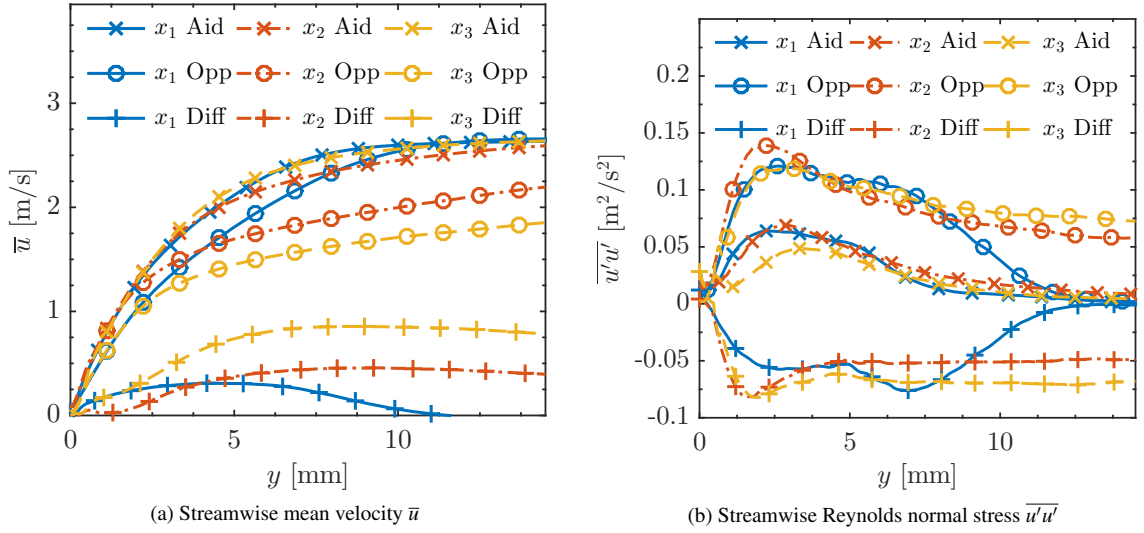


Fig. 2.10: Measured streamwise mean velocity \bar{u} and streamwise Reynolds normal stress $\overline{u'u'}$ with buoyancy-aided (Aid), buoyancy-opposed (Opp), and their difference (Diff) at three locations in x

The measured temperature profile from the TC probe for the buoyancy-opposed case is shown in Fig. 2.11a. The development of the thermal boundary layer is observable in x . The temperature in the near-wall region and line fit are shown in Fig. 2.11b. Errors in distance from the wall are corrected by fitting the line through the measured wall temperature. The first point is not considered as it is likely to have position error. Only data within $y^+ \leq 6.6$ are used in the fit as they should be contained in the inner portion of the viscous or laminar sublayer where linear temperatures are expected. Temperature fluctuations are not included as the mass of the TC wire rendered it insensitive to the higher frequencies in this flow. These frequencies were determined with a 50.8- μm diameter tungsten hot-film probe with much less thermal mass.

The intrusive nature of the probe caused an increase in wall heat flux observable in the HFS data acquired at the time. The largest error of wall heat flux occurred when the probe was touching the heated wall and steadily decreased as the probe was retracted from the wall. Maximum errors of 18.7%, 10.4%, and 7.93% were measured at locations x_1 , x_2 , and x_3 , respectively. This effect will only bias the temperature data

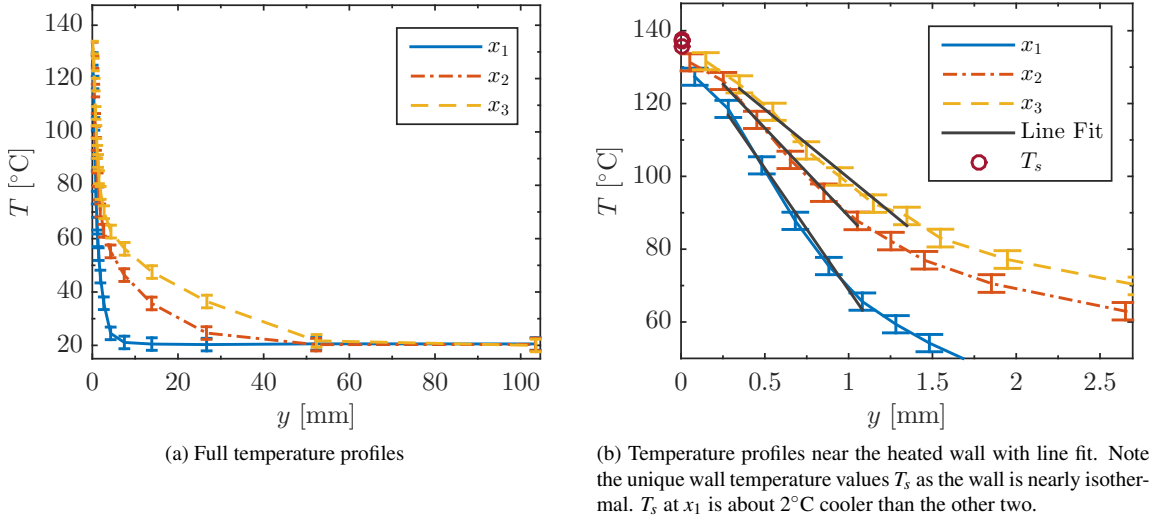


Fig. 2.11: Measured temperature profiles for all three x locations for the opposed case

provided as all other BC and SRQ data were acquired at other times. Intrusive probes should be avoided in validation experiments as the effect of their presence is often difficult to quantify. As such, the use of these temperature data is recommended for qualitative analysis but may not be appropriate for quantitative assessment as an SRQ.

Wall heat flux, as measured by the HFSs, is shown in Fig. 2.12. In laminar flows, buoyancy-aided mixed convection produces higher heat flux values than for buoyancy-opposed [7]. The current experiments show the opposite, suggesting turbulence levels are a major contributor to the flux. These observations are consistent with turbulent mixed convection. As there are no known heat transfer correlations for mixed convection in developing channel flow, the correlation for fully developed flow in vertical tubes was used as Eqn. 6 in the work of Jackson *et al.* [9]. These are consistent with the observed heat flux as the buoyancy opposed case generated higher heat flux. The correlation values have been adjusted to consider an unheated starting length with distances from the virtual origin analysis described earlier. The local Nusselt number was adjusted by

$$\text{Nu}_x = \frac{\text{Nu}_x|_{\xi=0}}{\left[1 - (\xi/x)^{9/10}\right]^{1/9}} \quad (2.11)$$

where the local Nusselt number Nu_x and $\text{Nu}_x|_{\xi=0}$ was measured from the leading edge of the unheated starting length [8].

The measured trends in the streamwise direction x are inconsistent with expected results. The HFS at x_2 gives a smaller reading than that at x_3 for both cases. It is possible that this trend is caused by an installation

error of the potted sensors in the heated wall. Even though the cause is unknown, the likelihood of this error existing is supported by the monotonic decrease in the temperature gradient near the wall with streamwise distance x as observed in Fig. 2.11b. This decrease suggests a decrease in wall heat flux with x , consistent with theory.

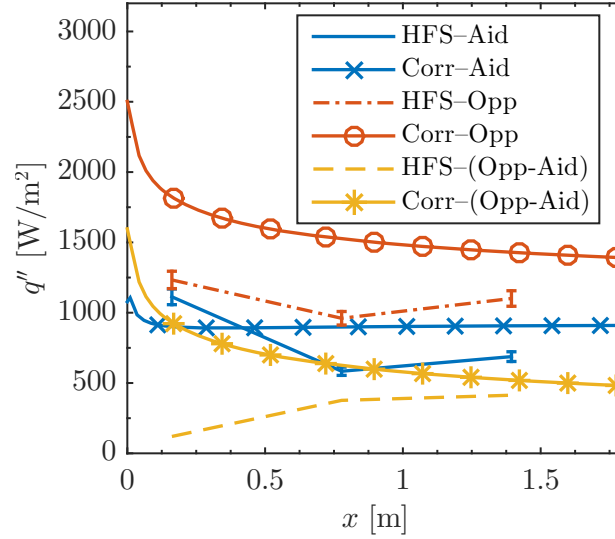


Fig. 2.12: Measured wall heat flux plotted along streamwise direction x with correlations for mixed convection for the buoyancy-aided (Aid), buoyancy-opposed (Opp), and their difference (Aid-Opp). Heat Flux Sensor results are labeled as HFS and correlation results as Corr.

Previous methods to quantify wall shear have fit experimental turbulent velocity data with empirical models such as Spalding or Musker profiles with high accuracy [21]. This method works well for fully turbulent boundary layer data where the models are an accurate representation of velocity, but not for the data in this study due to significant buoyancy effects. Therefore, wall shear stress was estimated directly from PIV data as $\tau_s = \mu \frac{\partial u}{\partial y} \big|_{y=0}$ where τ_s is wall shear stress and μ is dynamic viscosity. High-resolution PIV data were used to fit a line to velocity data where $y^+ = y u_\tau / \nu \leq 3$ to find $\frac{\partial u}{\partial y} \big|_{y=0}$, where $u_\tau = \sqrt{\tau_s / \rho}$ and ρ is the fluid density [7]. Initially 10 points were included in the fit and a stable iterative method was used to calculate τ_s and the number of data points to fit within $y^+ \leq 3$. The wall was located by the particle images with a mask carefully defined. The linear fit was performed using linear regression with more weight given to velocity data with lower uncertainty [22]. The high-resolution PIV data and associated linear fit are shown in Fig. 2.13. The dynamic viscosity was evaluated using Sutherland's Law at the wall temperature. The fit uncertainty was combined with the viscosity uncertainty using the Taylor Series Method [18].

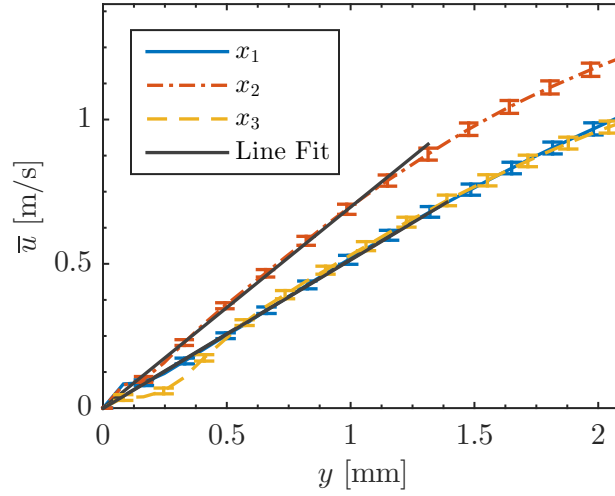


Fig. 2.13: Streamwise mean velocity \bar{u} near the heated wall with linear fit for shear stress measurement of the buoyancy-opposed case

Data acquisition was repeated several times for each case to determine the level of repeatability. There are generally two versions of the same data with the exception of the buoyancy-aided case at x_1 , which has three. Data were acquired between one to ten months apart and, in the buoyancy-opposed case, with a different camera. The acquisitions were also performed by two different users. The test section was disassembled, repaired, and reassembled between the second (R2) and third (R3) series for the buoyancy-aided case. The PIV equipment was removed, replaced, and recalibrated between series. The tabulated data included in this work are from the series R1 in both cases. The results for the mean streamwise velocity are shown in Figs. 2.14a & 2.14b for the buoyancy-aided and opposed cases respectively. They show only small differences that are more apparent in the buoyancy-opposed case.

Repeatability plots for mean streamwise Reynolds stress $\overline{u'u'}$ are shown in Figs. 2.15a & 2.15b for the two cases. The Reynolds stresses are less repeatable than the mean velocity, but only by a moderate amount. The results at x_1 have the largest difference, which may be due to differences in the inflow that become less important with streamwise development.

As mentioned previously, there is a large difference in turbulence levels between the buoyancy-aided and opposed cases. Another method for representing the differences is the scatter plot of $\overline{u'v'}$. There is little scatter in the buoyancy-aided case (Fig. 2.16a) compared to the buoyancy-opposed case (Fig. 2.16b), suggesting laminarization is occurring in the buoyancy-aided case. These results are consistent with the findings of other works in turbulent mixed convection. The results show the typical predominance of events

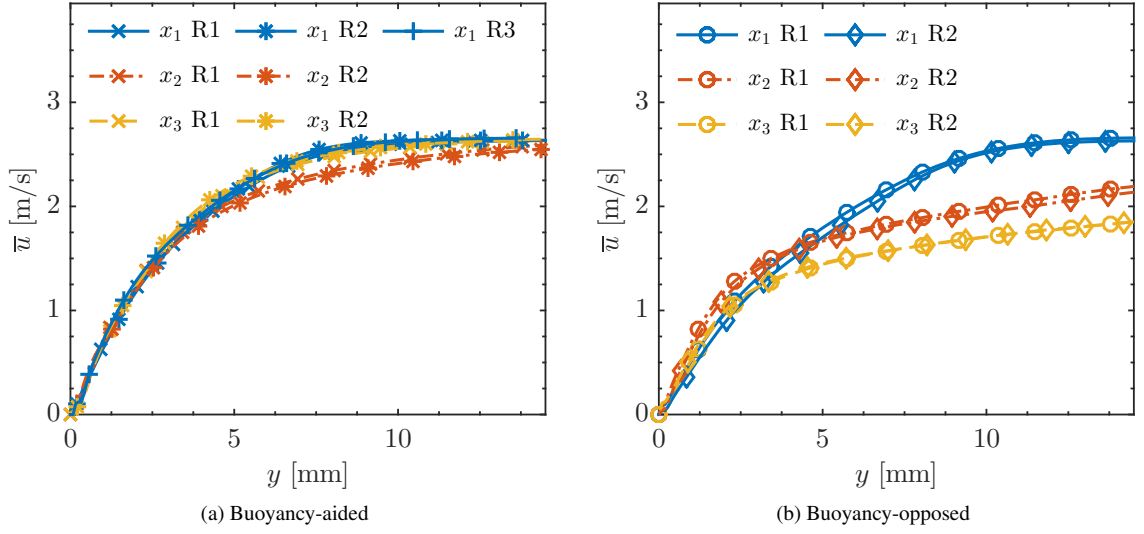


Fig. 2.14: Mean streamwise velocity \bar{u} with several repeats at three locations in x for both cases

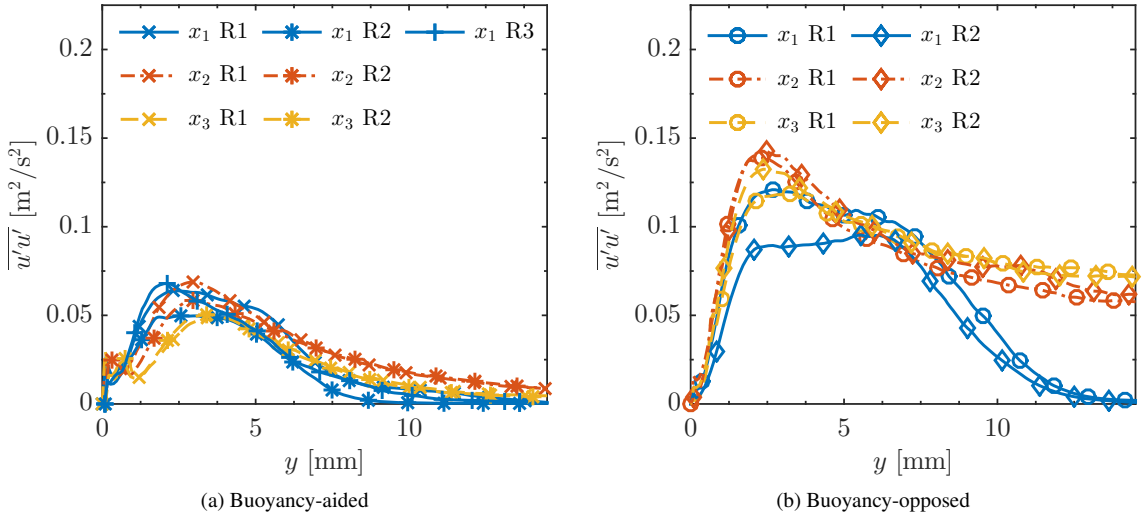


Fig. 2.15: Measured mean streamwise Reynolds stress $\overline{u'u'}$ with several repeats at three locations in x for both cases

in quadrants 2 and 4, which are related to turbulent ejections and sweeps respectively.

2.7.2 SRQ Data

These data are generally found in one file for each x location with unique files for each orientation. For all SRQ files, the same global coordinate system is used and units are included in column headers. Links to

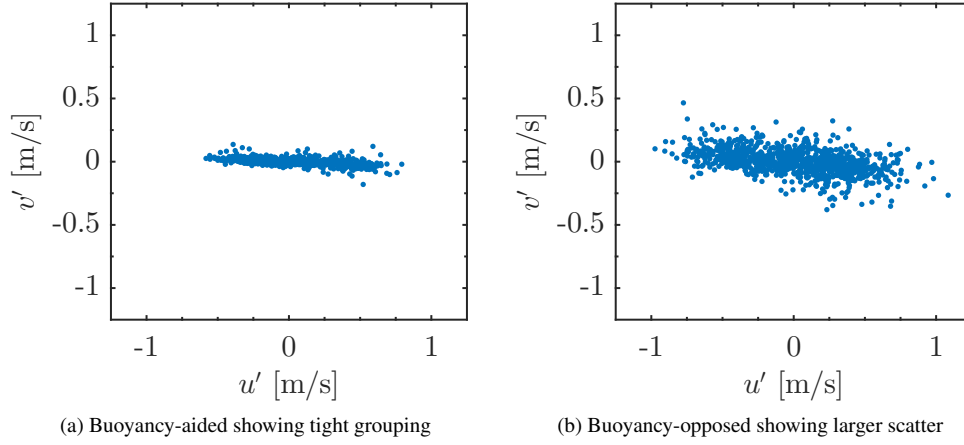


Fig. 2.16: Scatter of instantaneous u' and v' at the y -location of largest $\overline{u'u'}$ for both cases at x_2

the velocity results are found in Table 2.7. Velocities and Reynolds stresses in both measured directions are given as well as Reynolds shear stress. Uncertainties are provided for all provided quantities as before.

Table 2.7: Links to velocity SRQ files for both cases

Aided	Opposed
Aid-SRQ-Vel_x1	Opp-SRQ-Vel_x1
Aid-SRQ-Vel_x2	Opp-SRQ-Vel_x2
Aid-SRQ-Vel_x3	Opp-SRQ-Vel_x3

Temperature profile data are available for the buoyancy-opposed case at all three x locations in files [Opp-SRQ-T_x1](#), [Opp-SRQ-T_x2](#), and [Opp-SRQ-T_x3](#). Tabulated results for the scalar wall heat flux are compiled into the files [Aid-SRQ-HeatFlux](#) and [Opp-SRQ-HeatFlux](#). Shear results are similarly compiled into files [Aid-SRQ-Shear](#) and [Opp-SRQ-Shear](#).

2.8 Conclusions

This work has presented a highly detailed study on turbulent mixed convection along a vertical, flat plate using high fidelity instrumentation. The data and description are believed to be sufficient for a CFD validation study of these physics to determine validation error (Eqn. 2.1) and validation uncertainty (Eqn. 2.2). The effects of buoyancy were investigated in two orientations, buoyancy-aided and buoyancy-opposed. Buoyancy was found to have a laminarizing effect on the boundary layer flow in the buoyancy-aided case that suppressed

heat transfer. The buoyancy-opposed case had increased turbulence levels and higher heat flux. All requisite BCs were measured and provided with their uncertainties. A variety of SRQs were reported for comparison with simulation outputs. Tabulated data were provided by digital links for direct use. This method of data description and dissemination can greatly enhance the ability of modelers to assess simulation accuracy. Furthermore, the inclusion of this information in published works increases their availability.

Acknowledgments

This research was performed using funding received from the DOE Office of Nuclear Energy's Nuclear Energy University Programs, and their support is gratefully acknowledged.

References

- [1] Oberkampf, W. L., and Smith, B. L., 2014, "Assessment Criteria for Computational Fluid Dynamics Validation Benchmark Experiments," 52nd Aerospace Sciences Meeting of AIAA.
- [2] Harris, J. R., Lance, B. W., and Smith, B. L., 2015, "Experimental Validation Data for Computational Fluid Dynamics of Forced Convection on a Vertical Flat Plate," *Journal of Fluids Engineering*, **138**(1), p. 011401, doi:[10.1115/1.4031007](https://doi.org/10.1115/1.4031007).
- [3] Oberkampf, W. L., and Roy, C. J., 2010, *Verification and Validation in Scientific Computing*, Cambridge University Press, doi:[10.1017/cbo9780511760396](https://doi.org/10.1017/cbo9780511760396).
- [4] ASME, 2009, "ASME V&V 20-2009: Standard for Verification and Validation in Computational Fluid Dynamics and Heat Transfer," Standard, American Society of Mechanical Engineers.
- [5] Roache, P. J., 2009, *Fundamentals of Verification and Validation*, Hermosa Publ.
- [6] AIAA, 1998, "Guide for the Verification and Validation of Computational Fluid Dynamics Simulations," Tech. Rep. AIAA G-077-1998, American Institute of Aeronautics and Astronautics, Reston, VA, doi:[10.2514/4.472855](https://doi.org/10.2514/4.472855).
- [7] Kays, W. M., Crawford, M. E., and Weigand, B., 2012, *Convective Heat and Mass Transfer*, 4th ed., McGraw-Hill.
- [8] Incropera, F. P., Dewitt, D. P., Bergman, T. L., and Lavine, A. S., 2007, *Fundamentals of Heat and Mass Transfer*, 6th ed., John Wiley & Sons.
- [9] Jackson, J. D., Cotton, M. A., and Axcell, B. P., 1989, "Studies of Mixed Convection in Vertical Tubes," *International Journal of Heat and Fluid Flow*, **10**(1), pp. 2–15, doi:[10.1016/0142-727x\(89\)90049-0](https://doi.org/10.1016/0142-727x(89)90049-0).
- [10] Chen, T. S., Armaly, B. F., and Ramachandran, N., 1986, "Correlations for Laminar Mixed Convection Flows on Vertical, Inclined, and Horizontal Flat Plates," *Journal of Heat Transfer*, **108**(4), p. 835, doi:[10.1115/1.3247020](https://doi.org/10.1115/1.3247020).
- [11] Ramachandran, N., Armaly, B. F., and Chen, T. S., 1985, "Measurements and Predictions of Laminar Mixed Convection Flow Adjacent to a Vertical Surface," *Journal of Heat Transfer*, **107**(3), p. 636, doi:[10.1115/1.3247471](https://doi.org/10.1115/1.3247471).

- [12] Kim, W. S., Jackson, J. D., He, S., and Li, J., 2004, "Performance of a Variety of Low Reynolds Number Turbulence Models Applied to Mixed Convection Heat Transfer to Air Flowing Upwards in a Vertical Tube," *Proceedings of the Institution of Mechanical Engineers, Part C: Journal of Mechanical Engineering Science*, **218**(11), pp. 1361–1372, doi:[10.1177/095440620421801107](https://doi.org/10.1177/095440620421801107).
- [13] Wang, J., Li, J., and Jackson, J., 2004, "A Study of the Influence of Buoyancy on Turbulent Flow in a Vertical Plane Passage," *International Journal of Heat and Fluid Flow*, **25**(3), pp. 420–430, doi:[10.1016/j.ijheatfluidflow.2004.02.008](https://doi.org/10.1016/j.ijheatfluidflow.2004.02.008).
- [14] Kähler, C. J., Sammler, B., and Kompenhans, J., 2002, "Generation and Control of Tracer Particles for Optical Flow Investigations in Air," *Experiments in Fluids*, **33**, pp. 736–742, doi:[10.1007/s00348-002-0492-x](https://doi.org/10.1007/s00348-002-0492-x).
- [15] Touloukian, Y. S., and Ho, C. Y., 1977, *Thermophysical Properties of Selected Aerospace Materials Part II: Thermophysical Properties of Seven Materials*, Purdue University, West Lafayette.
- [16] Warner, S. O., and Smith, B. L., 2014, "Autocorrelation-based Estimate of Particle Image Density for Diffraction Limited Particle Images," *Measurement Science and Technology*, **25**(6), p. 065201, doi:[10.1088/0957-0233/25/6/065201](https://doi.org/10.1088/0957-0233/25/6/065201).
- [17] Blackwell, B. F., Kays, W. M., and Moffat, R. J., 1972, "The Turbulent Boundary Layer on a Porous Plate: an Experimental Study of the Heat Transfer Behavior with Adverse Pressure Gradients," Tech. Rep. HMT-16, The National Aeronautics and Space Administration.
- [18] Coleman, H. W., and Steele, W. G., 2009, *Experimentation, Validation, and Uncertainty Analysis for Engineers*, John Wiley & Sons, doi:[10.1002/9780470485682](https://doi.org/10.1002/9780470485682).
- [19] Timmins, B. H., Wilson, B. W., Smith, B. L., and Vlachos, P. P., 2012, "A Method for Automatic Estimation of Instantaneous Local Uncertainty in Particle Image Velocimetry Measurements," *Experiments in Fluids*, **53**(4), pp. 1133–1147, doi:[10.1007/s00348-012-1341-1](https://doi.org/10.1007/s00348-012-1341-1).
- [20] Wilson, B. M., and Smith, B. L., 2013, "Taylor-series and Monte-Carlo-method Uncertainty Estimation of the Width of a Probability Distribution Based on Varying Bias and Random Error," *Meas. Sci. Technol.*, **24**(3), p. 035301, doi:[10.1088/0957-0233/24/3/035301](https://doi.org/10.1088/0957-0233/24/3/035301).
- [21] Kendall, A., and Koochesfahani, M., 2007, "A Method for Estimating Wall Friction in Turbulent Wall-bounded Flows," *Exp Fluids*, **44**(5), pp. 773–780, doi:[10.1007/s00348-007-0433-9](https://doi.org/10.1007/s00348-007-0433-9).
- [22] Bevington, P. R., and Robinson, D. K., 2003, *Data Reduction and Error Analysis*, McGraw–Hill, New York.

CHAPTER 3

EXPERIMENTAL VALIDATION DATA FOR CFD OF TRANSIENT MIXED CONVECTION ON A VERTICAL FLAT PLATE

Abstract

Transient convection was investigated experimentally for the purpose of providing Computational Fluid Dynamics (CFD) validation data. A specialized facility for validation experiments called the Rotatable Buoyancy Tunnel was used to acquire thermal and velocity measurements of flow over a smooth, vertical heated plate. The initial condition was forced convection downward with subsequent transition to mixed convection, ending with natural convection upward after a flow reversal. Data acquisition through the transient was repeated for ensemble-averaged results. With simple flow geometry, validation data were acquired at the benchmark level. All boundary conditions (BCs) were measured and their uncertainties quantified. Temperature profiles on all four walls and the inlet were measured, as well as as-built test section geometry. Inlet velocity profiles and turbulence levels were quantified using Particle Image Velocimetry. System Response Quantities (SRQs) were measured for comparison with CFD outputs and include velocity profiles, wall heat flux, and wall shear stress. Extra effort was invested in documenting and preserving the validation data. Details about the experimental facility, instrumentation, experimental procedure, materials, BCs, and SRQs are made available through this paper. The latter two are available for download and the other details are included in this work.

3.1 Introduction

The purpose of this work is to provide validation data for three-dimensional Computational Fluid Dynamics (CFD) models. Model validation will be discussed as well as the physical phenomenon of mixed convection. The following sections describe the experimental facility, the associated instrumentation, the boundary conditions (BCs), the fluid and material properties, the test conditions, and the System Response Quantities (SRQs). This content follows the Validation Experiment Completeness table of Oberkampf and Smith [1] to guide description of validation experiments. This guidance ensures important details are included with a high level of completeness. The work contained herein is a continuation of that by Harris *et al.* [2] which covered forced convection using similar methods and facilities.

This work presents the data in table format for direct use in validating models. The provided data include the BCs and SRQs shown in Table 3.1. The included BCs in this work should provide modelers with all required information, avoiding assumptions on model inputs and reducing model form uncertainty [3]. The SRQ data are provided to modelers for direct comparison with model outputs. The experimental uncertainties of all provided data from bias and random sources are also provided and quantified at the 95% confidence level. Validation errors can be calculated with the nominal data and validation uncertainty from the uncertainty of the nominal data [4].

Table 3.1: The available experimental data presented in this work separated into BC and SRQ types

BCs	SRQs
As-Built Geometry	Velocity Profiles
Wall Temperatures	Reynolds Stress Profiles
Inlet Temperature	Wall Heat Flux
Inlet Velocity	Wall Shear
Atmospheric Conditions	

These files are accessible in an online database in the Digital Commons of Utah State University's Library. The page dedicated to the data in this work is found at digitalcommons.usu.edu/all_datasets/8/. Links to specific files are included in this work with descriptive file names with the experimental case (Trans), data type (BC or SRQ), and measured quantity. All data files may be downloaded in the zipped file [Data](#). Generally, data are in table format as csv files.

3.1.1 Computational Fluid Dynamics Validation

To understand the need for experiments expressly aimed at providing validation data, one must first understand the different aims of validation and discovery experiments. Discovery experiments are common in research where new physical phenomena are measured, presented, and discussed. Validation experiments do not necessarily measure unique phenomena, but the measurement process and description are more complete [5]. In general, older experimental data from discovery experiments are not sufficiently described for use in validation. Unobtrusive measurement techniques are important in validation experiments since probes introduce unknown uncertainties to the data. These uncertainties can only be mitigated by including the probe in the CFD model.

The purpose of validation experiments is to provide the information required to quantify the uncertainty

of a mathematical model. This uncertainty helps decision makers quantify model credibility. The ASME V&V 20 Standard [4] outlines an approach to estimate the validation comparison error and the validation uncertainty. The validation error E is the difference between the simulation result S and the validation experiment result D as

$$E = S - D. \quad (3.1)$$

Calculating the validation uncertainty estimates the confidence interval of the error by considering both numerical and experimental uncertainty. Validation uncertainty is calculated as

$$U_{\text{val}} = \sqrt{U_{\text{num}}^2 + U_{\text{input}}^2 + U_D^2}, \quad (3.2)$$

where U_{num} is the numerical uncertainty, U_{input} is the model input uncertainty, and U_D is the experimental data uncertainty. The numerical uncertainty is estimated from solution verification with sources such as iterative and discretization uncertainty. The latter two uncertainties come from the validation data. The uncertainty in the measured BCs that are used for model inputs is U_{input} . The uncertainty of SRQs—experimental data used to compare system outputs—is U_D . If $|E| \gg U_{\text{val}}$, one can conclude model error remains. But if $|E| \leq U_{\text{val}}$ and U_{val} is acceptably small for the intended use of the model, the validation error may be satisfactory. These general equations show validation data and their uncertainties are required to assess model accuracy via model validation.

There are several tiers of detail in validation experiments [6], often four as shown in Fig. 3.1. This work is considered a Benchmark Case that is second in simplicity to Unit Problems. The Benchmark Case, also called Separate Effects Testing, requires that all model inputs and most model outputs are measured and that experimental uncertainty is included. In this tier there is generally some level of multi-physics interaction, such as coupled fluid momentum and heat transfer, that prevents this work from being considered a Unit Problem. On the other hand, the non-prototypical geometry used in this work keeps it from being a Subsystem Case.

The planning and execution of validation studies should include both modelers and experimentalists through all phases. In considering the design of validation systems, SRQs should be measured from a wide range and high difficulty in the difficulty spectrum as shown in Fig. 3.2. Comparing simulation results with experimental data from a wide range on the spectrum increases validation confidence. For example, integral quantities, such as fluid mass flow rate, generally have low experimental noise and random errors. Derivative quantities like fluid shear are more sensitive to non-ideal conditions. If a model and data are in

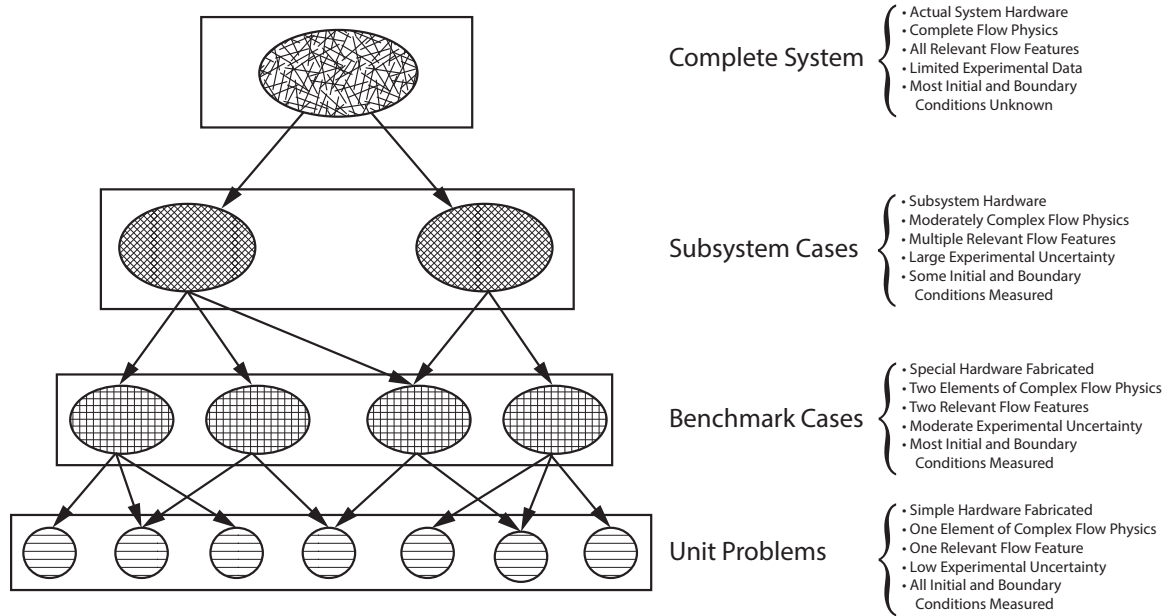


Fig. 3.1: The Validation Hierarchy, after [6]

good agreement at a high level, then it is likely that good agreement will be observed in lower levels. But, agreement at lower levels does not imply agreement at higher levels [3].

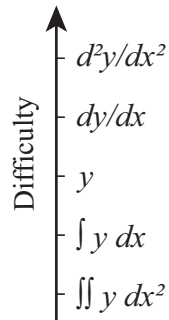


Fig. 3.2: System Response Quantity Difficulty Spectrum, after [3]. The variables y and x are arbitrary.

3.1.2 Transient Flows

Some studies of non-periodic transient flow have been performed, but as He & Jackson note, only recently has technology allowed for comprehensive measurements of ensemble averaged transient experiments [7]. This review covers adiabatic and convective ramp-type flow transients. Most of the first experi-

ments measured either temperature of tube walls or velocity, but not both. A common observation was that accelerating flow suppresses turbulence while decelerating flow augments it.

The first known work by Koshkin *et al.* was published in 1970 for turbulent air flow. This study reported measurements during a change in electrical power and different flow transients, measuring and reporting temperature [8]. Two similar studies were published in the 1970s and used electrochemical techniques with probes to measure velocity profiles inside a tube from a step change in flow rate [9, 10].

Rouai [11] performed heat transfer experiments on ramp-up and ramp-down transients as well as periodic pulsating flow with a non-zero time mean. Water was heated by passing an alternating electrical current through a stainless steel tube. Temperature measurements were made by 24 thermocouples (TCs) welded to this tube. Flow transients were prescribed by using a constant head tank and varying the flow through the test section by a valve. Wall heat flux remained constant and changes in wall temperature were measured. The observed Nusselt number departed more from the pseudo-steady values for faster transients and for decelerating flows, likely from the augmentation of turbulence.

Jackson *et al.* performed a study on non-periodic ramping transients in a water tube [12]. It was similar to that by Rouai but measured local fluid temperature with a TC probe and improved computer control and data logging for greater repeatability and ensemble averaging. The TC probe was small enough to capture turbulent fluctuations. They also found a suppression of turbulence and consequently wall heat transfer for accelerating ramps and augmentation during decelerating ramps. They also observed a peak in temperature fluctuations soon after the start of the ramps.

He & Jackson performed experiments in water using two-component LDA measurements in a clear, unheated tube. This non-intrusive velocity measurement was one of the first known to the authors for non-periodic flows. Ensemble averaged results were used for mean and turbulent quantities. The turbulent results were shown to deviate from pseudo-steady results for short transients. Several nondimensional parameters were recommended for ramp-type transients [7].

Barker and Williams [13] reported high speed measurements of an unsteady flow with heat transfer in air. They used a hot wire anemometer, a cold wire temperature probe, and a surface heat flux sensor to measure heat transfer coefficients for fully-developed turbulent pipe flow. Most results were for periodic flows, but some were presented for ramp-type transients with negligible buoyancy effects. The measurements were basic and provided data for conceptual model development.

In the previous studies, little coupling of velocity and thermal measurements was found for flow transients and buoyancy effects were negligible. Also, as these were discovery experiments, boundary conditions

were not measured and provided as tabulated data, making the results of limited use for validation. The facility description is very basic and flow geometries simplified. The current study contributes high fidelity measurements of a ramp-down transient suitable for validation studies with simultaneous, non-intrusive velocity and thermal measurements to provide validation data on simplified geometry for three-dimensional simulations.

3.1.3 Mixed Convection

The physics in this study include a flow transient with buoyancy effects, phenomena that have not been studied together in the known literature. Convective flows with notable buoyancy effects are considered mixed or combined convection [14]. The Richardson number Ri is a measure of the relative magnitudes of buoyant and inertial forces and is defined by

$$Ri_x = Gr_x / Re_x^2 \quad (3.3)$$

where

$$Gr_x = g\beta(T_s - T_\infty)x^3/\nu^2 \quad (3.4)$$

and

$$Re_x = \bar{u}_{bulk}x/\nu. \quad (3.5)$$

In these, g is acceleration due to gravity, β is fluid thermal coefficient of expansion, $T_s = 130^\circ$ and $T_\infty = 20$ are surface and fluid temperatures, respectively, x is local streamwise location, ν is fluid kinematic viscosity, and \bar{u}_{bulk} is bulk mean velocity. Mixed convection is observed for buoyancy-aided flow when $0.3 < Ri_x < 16$ and for $0.3 < Ri_x$ for opposed flow [14].

Table 3.2 shows the streamwise locations x where data were acquired at the spanwise center with the associated Gr_x , as well as Re_x and Ri_x at the initial condition. External coordinates were used as the boundary layers generally do not meet as in fully-developed pipe flow. Fluid properties were evaluated at the film temperature. Initially buoyancy effects were small but became dominant at later phases of the transient.

3.2 Experimental Facility

All experiments were performed in the Rotatable Buoyancy Tunnel (RoBuT), which will be described in detail. Benchmark-level validation data were acquired with simple geometry and some multi-physics interaction. The square test section allowed easy characterization using optical velocity measurements. The

Table 3.2: Gr_x as well as Re_x and Ri_x at the initial condition at the three locations in x at the spanwise center where data were acquired

	x [m]	Gr_x	$Re_x (t=0)$	$Ri_x (t=0)$
x_1	0.16	1.46×10^7	23,300	0.027
x_2	0.78	1.62×10^9	112,000	0.129
x_3	1.39	9.32×10^9	201,000	0.231

simple geometry is easy to represent numerically and helps isolate model errors.

3.2.1 Rotatable Buoyancy Tunnel

The RoBuT was an open-circuit air tunnel with a large 4.81-m diameter ‘Ferris wheel’ design that allowed rotation, thus changing the relative direction of forced flow and buoyant forces without changing the facility. Many important tunnel components are shown in Fig. 3.3, which is in the buoyancy-opposed orientation. Note the coordinate system with the origin on the heated wall at the inlet and the spanwise center. The streamwise distance is x , wall-normal distance is y , and spanwise distance is z with zero along the centerline. The laser and cameras were part of a Particle Image Velocimetry (PIV) system that will be described in Sec. 3.3.2.

The test section had a 0.305×0.305 m square cross section and was 2 m long. It had three clear walls for optical access and a heated wall for a thermal BC. More details of the test section are provided in Sec. 3.2.2. The contraction and outlet were made of fiberglass-reinforced plastic with a glass-smooth, black gel-coat.

The contraction had an area ratio of 6.25:1 and was 0.914 m long. The contraction bell at the leading edge had a 102 mm radius. Between the contraction and bell were four modular sections that contained—in order of flow direction—a single row, aluminum fin/copper tube, chilled water heat exchanger (Super Radiator Coils Model 30x30-01R-0.625/048); a settling length section; a precision aluminum honeycomb flow straightener; and two high porosity screens. Square turbulence trips 3.175 mm wide were installed along all four walls and located about 0.12 m upstream of the test section inlet.

The outlet expanded the flow downstream of the test section, had a total included angle of 8.2° , and was 0.686 m long. The blower drew air through the test section and rejected it into the room. It included an inline centrifugal fan assembly, TCF/Aerovent model 14-CBD-3767-5. It was belt driven by a 5 HP, TEFC, 230-460 VAC induction motor, Toshiba model B0052FLF2AMH03. The motor was powered by a Toshiba variable frequency drive, model VFS11-2037PM-WN.

Two Laskin Nozzles [15] were used to atomize olive oil tracer particles. These were measured to have

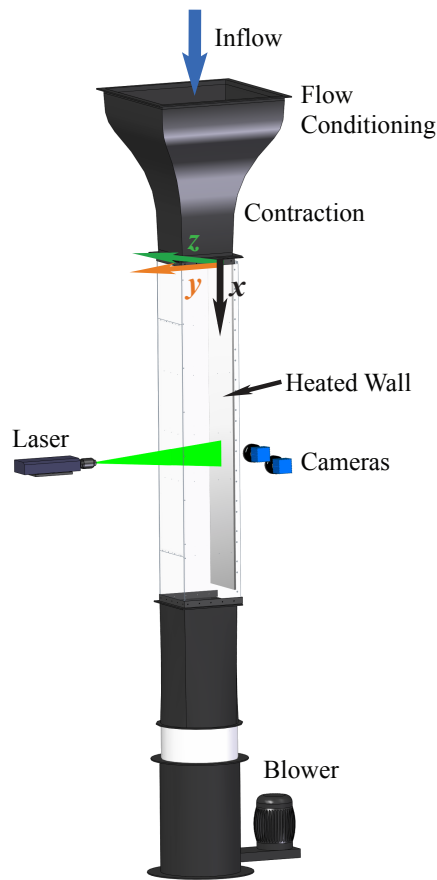


Fig. 3.3: RoBuT flow components as configured for transient data acquisition

a mean diameter of about $1\mu\text{m}$ with a TSI Aerodynamic Particle Size Spectrometer at the outlet. These particles were mixed with air and injected into a PVC pipe distribution system upstream of the contraction assembly. A peg board was placed between this system and the beginning of the contraction to help mix particles throughout the flow. It had holes 6.35 mm in diameter and were spaced 25.4 mm apart in a square pattern.

3.2.2 Test Section

The test section had four walls, an inlet, and an outlet that will be described in detail. The heated wall was custom designed with many layers to provide a heated surface for convection and featured embedded instrumentation. Its cross section is shown in Fig. 3.4. This wall was heated to approximately 130°C for this study. It was made of several layers of aluminum, had six silicon rubber heaters arranged in the streamwise direction, and contained thermal insulation to drive most of the heat inward. A list of materials and thick-

nesses is available in Table 3.3. The surface was nickel plated to reduce thermal radiation which resulted in a predicted and measured emissivity around 0.03 [2]. Aluminum 2024, though more expensive than the common alloy 6061, was used because its thermal conductivity is well known [16]. The heated portion was 279 mm wide and 1.89 m long. The left and right sides were thermally insulated by 17.5-mm thick Teflon[®] that extended into grooves in the side walls. Two additional 12.7-mm thick Teflon[®] insulators were placed upstream and downstream of the heated wall. There were six heaters, each spanning the width of the heated wall and one sixth of the length. Three HP 6439B power supplies were connected to two heaters each and were used to control the temperature of the wall via a closed-loop PI controller. Three controllers, one for each power supply, allowed the heated wall to be heated in independent sections in the streamwise direction to increase temperature uniformity.

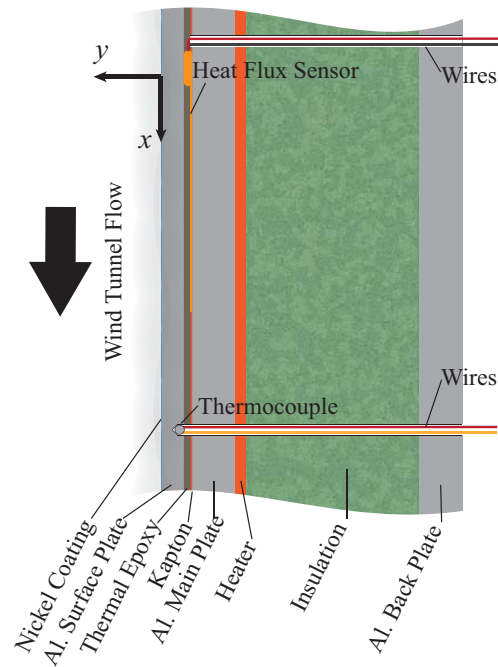


Fig. 3.4: Heated wall cross section with component names as in Table 3.3. The relative thicknesses are to scale.

The other three walls were clear Lexan[®] polycarbonate for optical access and were 12.7 mm thick. From the perspective of standing on the heated wall at the inlet, they are termed left ($z=-152$ mm), top ($y=305$ mm), and right ($z=152$ mm) walls. The top wall had a removable center portion for cleaning and maintenance. This wall also had three 25.4-mm ports for probe insertion.

Table 3.3: Heated wall components and thicknesses with names from Fig. 3.4

Name	Material	t [mm]
Nickel Coating	Bright Nickel	~ 0.05
Al. Surface Plate	Al. 2024-T3	3.18
Thermal Epoxy	Dow Corning 3-6751	1.02
Kapton [®]	Kapton [®] HN	0.254
Al. Main Plate	Al. 6061-T651	6.35
Heater	Tempco Silicone Rubber	1.59
Insulation	Mineral Wool	25.4
Al. Back Plate	Al. 6061-T651	6.35

The as-built geometry was measured to compensate for differences between the as-designed and as-built test section geometry. The differences were small, but the measurements are presented for completeness. An internal micrometer was used to measure the internal dimensions of the fully assembled test section. Height measurements were performed at the left, center, and right as well as width measurements at the top, middle, and bottom. This was done at seven locations in x and performed three times for a measure of random uncertainty. Modelers may use these dimensions when constructing the simulation domain to ensure greater similarity. A sketch of the measurement locations may be accessed from the online database by the link [All-BC-AsBuiltSketch](#) in the digital version of this work. The nominal values are in [All-BC-AsBuiltMeasurements](#) and uncertainties in [All-BC-AsBuiltMeasurementUncertainties](#). A Parasolid model created from the as-built measurements is available in [All-BC-AsBuiltGeometry](#).

A warm-up procedure was followed each time the RoBuT was used for experiments. Ideally, the HVAC system would be kept active at all times for stable room conditions. The heated wall was first heated to the setpoint temperature. Once this was reached, the blower was set to the desired speed for the experiment and the heater controllers would accordingly increase power. Once the temperature was again stable for at least five minutes, the facility was ready for data acquisition. If the blower setpoint speed was changed, the controller would stabilize temperature and a waiting period was repeated for at least five minutes.

Between acquiring different series of data, the entire test section was cleaned with Ethyl Alcohol and delicate task wipes to ensure optical quality. The cover on the top wall was removed for inside cleaning. High-vacuum grease was used on test section joints to eliminate air leakage and was removed and reapplied each time a panel of the test section was adjusted.

3.3 Analog Instrumentation and Signal Processing

Validation experiments require high fidelity instrumentation. Thermocouples were used to measure boundary temperatures, heat flux sensors (HFSs) for heat flux through the heated wall, and PIV for inflow and boundary layer air velocity. Other sensors measured room air conditions. These systems will now be described in detail.

3.3.1 Thermal Instrumentation

A total of 307 TCs were used to measure boundary temperatures. All test section TCs were 30 gauge Type K from Omega Engineering with Special Limits of Error. They were each welded to length with an Argon-shielded welder. Each TC was calibrated with an Isotherm FASTCAL-M with an accuracy of 0.3°C over a range of $25\text{--}190^{\circ}\text{C}$ with data at every 5°C . Because every TC calibration was very similar and made from the same spool, an average calibration curve was applied. An array of 3×5 TCs, three in y and five in z , was suspended on the downstream side of the honeycomb for inlet air temperature measurements. Each of the three clear walls had 21 TCs with seven rows spaced in x and three across in y for the left and right walls or in z for the top wall. The bulk of the heated wall had 5×32 TCs with five in z and 32 in x . The Teflon[®] edges each had embedded TCs with five across the leading edge in z and 32 along the sides in x . All TCs were embedded to within 3.18 mm of the inside surface using thermal epoxy with enhanced thermal conductivity.

Three HFSs were embedded into the heated wall along the spanwise center at the x -locations found in Table 3.2. They were model 20457-3 from RdF Corporation and were a thin-film type with a thermopile around a Kapton[®] substrate. The manufacturer supplied unique calibration coefficients for each sensor. The manufacturer-specified uncertainty was 5% of reading. An embedded Type T TC was used to measure sensor temperature and correct readings with the supplied multiplication factor curve to compensate for changes in thermal conductivity of the substrate. The HFSs were placed adjacent to the Kapton[®] layer of similar thermal resistance to reduce measurement errors. A thermal resistance network analysis showed only a 2.4% difference in heat flux between HFS and non-HFS conduction paths.

The TC and HFS output voltages were small, so special data acquisition (DAQ) devices were selected. National Instruments (NI) products were used as they interfaced well with the LabVIEW software that was used for system control and thermal data recording. Twenty one NI-9213 TC modules were housed in five NI-cDAQ-9188 chassis. The narrow voltage range of ± 78 mV, 24-bit ADC, and open channel detection made them well suited for these measurements. The built-in CJC was used for TCs. The total uncertainty of the calibrated TCs with these DAQs was 1°C , largely attributable to the CJC uncertainty of 0.8°C . Data from

thermal instrumentation were recorded throughout each transient run.

Data from thermal instrumentation was recorded through 2400 runs of the transient. These data were ensemble-averaged and the bias, random, and total uncertainty were quantified.

3.3.2 Particle Image Velocimetry

The PIV system allowed for non-intrusive, full-field velocity measurements at several locations. The system consisted of a laser, camera, and timing unit. The laser was a New Wave Research Solo PIV III. It was a dual cavity, frequency-doubled Nd:Yag model with about 22 mJ/pulse and a wavelength of 532 nm. The cameras were model Imager sCMOS that featured a 16-bit sCMOS sensor with 2560×2160 pixels with a pixel size of 6.5 μm . An internal, standard version timing unit was used for the stringent timing requirements of PIV and had a resolution of 10 ns and jitter of <1 ns. Two Nikon lenses were used. The first was an AF Nikkor 28 mm f/2.8 D used for the large field of view (FOV) inflow and the large FOV SRQ data that spanned the 0.305-m test section. The second was an AF Micro-Nikkor 105 mm f/2.8 D for high resolution (small FOV) SRQ data near the heated wall.

DaVis 8.2 software was used to acquire and process images. The optical configuration of Fig. 3.3 was used with the laser sheet normal to the heated wall and cameras viewing angles nearly parallel with it. The equipment was moved manually in the x direction. The inflow was measured in the same orientation but Velmex BiSlide[®] traverses were used to move the laser and camera consistently in the z direction. In this way five planes were measured to map the inflow.

PIV calibration was performed in two ways. The inflow used a conventional two-component ‘ruler’ calibration over a span of about 280 mm since the laser sheet and camera were normal to each other. The SRQ data were acquired with two independent two-component cameras, one that spans the entire test section and one that provides high resolution data near the heated wall. The SRQ data that spanned the test section used a custom two-plane calibration target that filled the image. The SRQ data near the heated wall was calibrated with a single-plane calibration target. Both SRQ sets used the pinhole model as the cameras were angled generally less than 5° . The pinhole model was applicable as refraction between the Lexan[®] and air was small. The near-wall SRQ camera angle was required to avoid image diffraction by the large temperature gradient very near the wall. Because this flow had very little through-plane motion, errors in v velocity from through-plane motion appearing as in-plane motion are expected to be small (they are a function of the sine of the angle).

Prior to acquisition, the quality of the particle images was checked to ensure proper particle density,

diameter, and displacement as well as laser beam overlap and image focus quality. Many of these data parameters and others from the acquired images are found in Table 3.4. The diameter, density, and displacement are spatial averages over the entire image. The maximum displacement was set between 8–32 pixels for all phases of the transient. To optimize dynamic range, two values of dt were used for each PIV data set. These are represented with a i/j in the table with the former being used for early phases and the latter for later phases. Since the reported values are spatially averaged, some may appear different from ideal simply due to their non-uniformity in space and in time. These data were taken from a phase near the middle of the transient. Both particle diameter and density were determined by methods found in [17] with the local maximum method for density estimation.

Table 3.4: PIV data parameters

Parameter	Inlet	SRQ-Large FOV	SRQ-Small FOV
N image pairs	100/200	100	100
Sample frequency [Hz]	5	5	5
dt [μ s]	860/3150	385/1541	96/385
lens	28 mm	28 mm	105 mm
extension [mm]	–	–	39.5
Calibration [mm/pixel]	0.123	0.121	0.0137
$f\#$	4	4	8
diameter [pixels]	1.98	1.98–2.55	2.68–3.00
density [$\#$ / 32×32]	86.7	57.3–88.1	8.04–11.8
displacement [pixels]	5.35–31.9	1.34–30.3	2.71–29.8

A MATLAB code was written to reorganize images. During acquisition, a set was recorded over all phases of the transient. The code would copy images from all runs for a given phase and create a new set. This process was repeated for all runs so data within each phase could be ensemble-averaged and fluctuations quantified.

The processing of particle images was performed using the window deformation method in DaVis. A mask was carefully defined to remove the influence of walls on the correlation. Round interrogation windows were used for reduced noise. The first two passes were at 128×128 pixels, the next two at 64×64 pixels, and the final four passes were at 32×32 pixels. The overlap on every pass was 75%. Vector post-processing was performed where vectors were removed if the peak ratio was less than two. Then a two-pass median filter of ‘strongly remove & iteratively replace’ corrected spurious vectors. Vectors were removed if their difference

from average was more than one standard deviation of neighbors and subsequently replaced if the difference from average was less than two standard deviations of neighbors.

Particle images have a sliding background removed where the background is the average of the set. The pixel range was narrowed in the flow direction to reduce disk space and processing time and was 340 pixels for the inflow images and 512 pixels for the SRQ images. Examples of dewarped particle images with background subtracted are shown in Fig. 3.5. The heated wall is on right of both images.

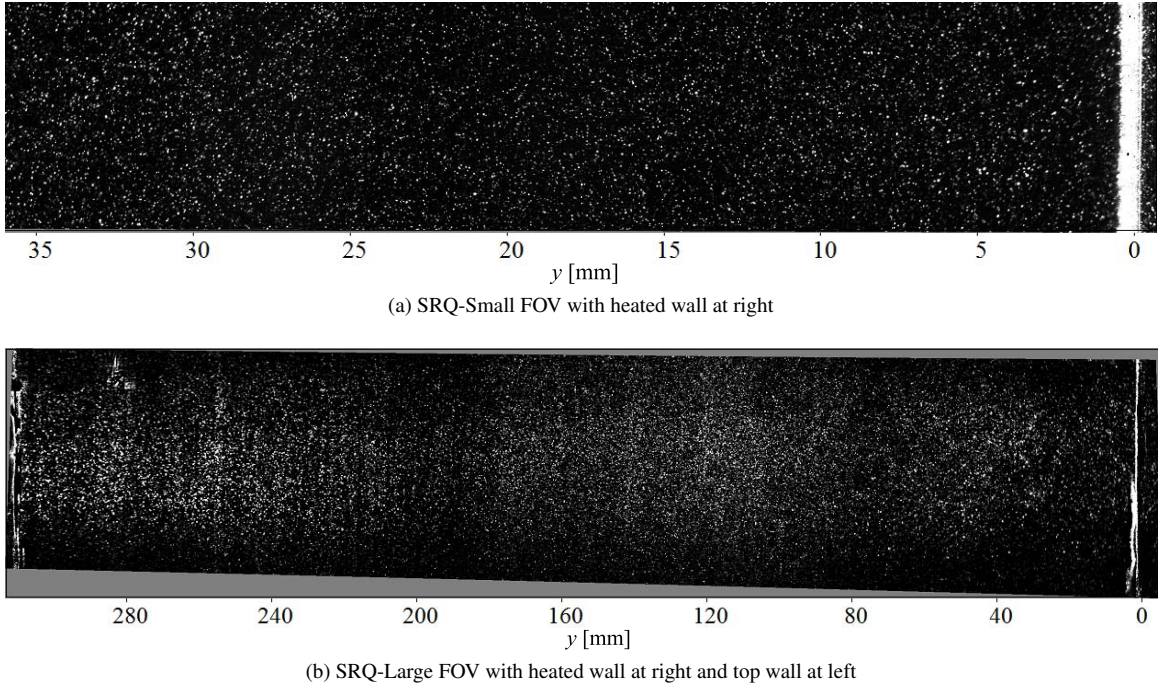


Fig. 3.5: Dewarped SRQ particle image at x_2 with mean background removed. Note the image scales are about a factor of nine different.

3.3.3 Atmospheric Instrumentation

Air temperature, relative humidity, and atmospheric pressure in the RoBuT room were measured to determine air properties. Both temperature and humidity were measured with an Omega HX93A probe. Pressure was measured with an Apogee Instruments BPS 1006 sensor. The output voltage of these sensors was measured by a NI USB-9215A 4-channel ± 10 V analog input DAQ. The uncertainty of temperature was 0.6°C , humidity was 2.5% for readings 20-80% and 3.1% otherwise, and pressure was 3% of reading. These data were sampled at 1 Hz, then averaged and recorded once per minute.

3.3.4 Uncertainty Quantification

Thermal and atmospheric data uncertainty quantification (UQ) is described here following methods of Coleman and Steele [18]. UQ for PIV was considered by other methods and is described later. Bias uncertainty parameters were obtained from sensor documentation at the 95% confidence level. The random uncertainty of a general mean quantity \bar{x} was calculated by

$$S_{\bar{x}} = t_{95} \frac{S_x}{\sqrt{N}} \quad (3.6)$$

where t_{95} is the confidence level coefficient (taken as 1.96 for 95% confidence and number of samples $N > 30$) and S_x is the sample standard deviation. Bias and random sources are combined as

$$U_{\bar{x}} = \sqrt{B_{\bar{x}}^2 + S_{\bar{x}}^2} \quad (3.7)$$

where $B_{\bar{x}}$ is the expanded bias uncertainty. The data provided with this paper generally specifies the unique bias, random, and total uncertainty numbers with the mean results.

Uncertainty of the PIV results was calculated from the Uncertainty Surface Method that estimates instantaneous bias and random uncertainties due to the effects of particle displacement, particle image density, particle image size, and shear. This method was originally described in [19] and improved on with methods from [17]. The uncertainties of the velocity statistics propagated from the instantaneous uncertainties were calculated by methods of Wilson & Smith [20]. Total uncertainty was calculated as in Eqn. 3.7. The confidence level on all UQ results in this work is 95%.

3.4 Boundary Conditions

This section contains a description of all expected requisite BCs for CFD model inputs. The types of BCs are shown in Table 3.1. The as-built geometry is a BC, but was discussed previously in Sec. 3.2.2.

3.4.1 BC Description

The measured BC temperatures are mapped onto the test section geometry in Fig. 3.6. Note the high measurement resolution on the heated wall and the development of the thermal boundary layer on the right wall as air travels from the inlet to the right of the figure.

As mentioned previously, the inflow was measured in five planes spaced in z with locations concentrated near the side walls. The time mean streamwise velocity \bar{u} at the inlet is shown in Fig. 3.7 at the initial

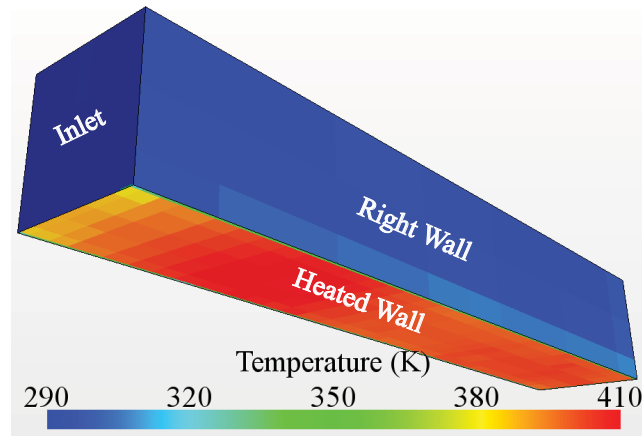


Fig. 3.6: Measured temperatures on the test section boundaries

condition. Gray lines indicate PIV measurement locations that span across y (two are at the left and right edges). Data are highly-resolved in y but not in z . Data may be interpolated from the information given. Another approach is to use the high-resolution data near the unheated top wall ($y=305$ mm) boundary layer to the left and right walls which are also unheated.

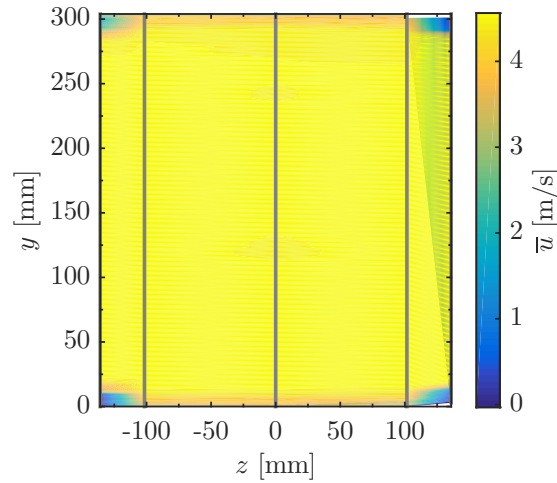


Fig. 3.7: Measured streamwise velocity \bar{u} at the inlet and the initial condition

The atmospheric conditions include atmospheric pressure, relative humidity, and room temperature and were recorded at the time of data acquisition.

Data acquisition procedures were followed to control test conditions. The following list describes the steps followed for acquisition of both BC and SRQ data:

1. Begin heating of the heated wall
2. Upon reaching setpoint temperature, start blower
3. Align traverses, laser, and camera with test section at measurement location
4. Align laser sheets
5. Focus camera on particle images
6. Align calibration plane with laser sheet and calibrate camera(s)
7. Determine optimal dt for particle displacement, proper seeding density, and proper laser intensity
8. Record measurement location and other PIV parameters
9. Confirm stability of wall temperature and room conditions
10. Record PIV data, atmospheric and thermal conditions

This process was repeated for PIV measurement locations for the five inflow and the three SRQ data sets. The acquisitions were automated by a LabVIEW program which controlled the conditions, determined when they were stable, initiated the transient and data acquisition (both thermal and PIV), and repeated.

3.4.2 BC Data

These data are available for all phases of the transient on the inflow and all four walls of the test section. There is one file for each surface that can be found through the following links: [Trans-BC-InletTemp](#), [Trans-BC-HeatedWallTemp](#), [Trans-BC-LeftWallTemp](#), [Trans-BC-RightWallTemp](#), and [Trans-BC-TopWallTemp](#). The format for all BC files works directly with Star-CCM+ and is easily adaptable to other CFD codes. The columns X, Y, and Z are used throughout this work; adhere to the global coordinates; and are presented in meters. The column 'T(K)' is the mean temperature in Kelvin, 'B.T(K)' is the bias uncertainty, 'S.T(K)' is the random uncertainty, and 'U.T(K)' is the total uncertainty. Additionally the time stamps are included for each column header as in 'T(K)[t=0s]', 'T(K)[t=0.2s]' and so forth.

The data file for the inflow mean and fluctuating velocities is found in [Trans-BC-Inlet-Vel](#). Here X, Y, and Z are again used as before and are presented in meters. The columns 'u', 'v', and 'w' are mean velocities in the x, y, and z directions, respectively. The columns 'u'u'', 'v'v'', 'w'w'', and 'u'v'' are specific Reynolds stresses. Uncertainties compose the remaining columns with the uncertainty of \bar{u} , \bar{v} , and \bar{w} . Reynolds stresses have unique plus and minus uncertainties with 'Uuup' being the plus uncertainty of $\overline{u'u'}$ and so on. The

units of velocity and velocity uncertainty are [m/s] while those of Reynolds stresses and their uncertainty are [m²/s²]. Again, time stamps are included in column headers.

Note that inflow out-of-plane velocities \bar{w} and $\overline{w'w'}$ were assumed to be the same as \bar{v} and $\overline{v'v'}$ respectively. This assumption was proved valid in previous work in this facility by measuring the inflow in both directions with two-component PIV and comparing data where measurement planes intersect [2]. The atmospheric measurements, together with their uncertainties, are found in the file [Trans-BC-AtmCond](#).

3.5 Fluid and Material Properties

As air is the working fluid, measurements of temperature, pressure, and relative humidity discussed in Sec. 3.4.2 are satisfactory to define all fluid properties. It is important to note that the working pressure is different from that at sea level as the experiment was conducted in Logan, Utah, which is 1460 meters above sea level.

Material properties of the test section can easily be obtained from the information provided in Sec. 3.2.2 about the construction of the test section. It is not necessary to model the heated wall since temperature measurements were made very near the surface, but the information is provided for completeness.

3.6 Test Conditions

For improved statistics, the data were ensemble-averaged over repeated runs. A total of 2400 runs were used, with 100-200 for each PIV acquisition location and dt . Steady thermal conditions triggered data acquisitions and simultaneously cut power to the blower, initiating transient conditions. Heater power was fixed through each run.

LabView was used to control the conditions and to acquire thermal data via a National Instruments data acquisition system. This system created the master TTL clock and also triggered the PIV system for synchronized thermal and velocity data acquisition. Data were acquired at 5 Hz for a period of 20.2 s. The initial condition was forced convection downward with the heated wall at 130°C. Blower power was removed and the drum-type blower was allowed to coast to a stop, which took about 10 s. This resulted in ramp-down bulk velocity and subsequent flow reversal by natural convection. The bulk velocity at the test section inlet at the centerline plane is shown in Fig. 3.8. The bulk velocity approaches zero at the end since there is both natural convection upward near the heated wall and recirculating flow downward far from the wall. There was measurable delay in the blower drive system, so $t = 0$ was prescribed as the last phase where the bulk velocity matched the initial condition. Thus, the useful transient time spans $0 \leq t \leq 18.2$ s and data are presented in this range.

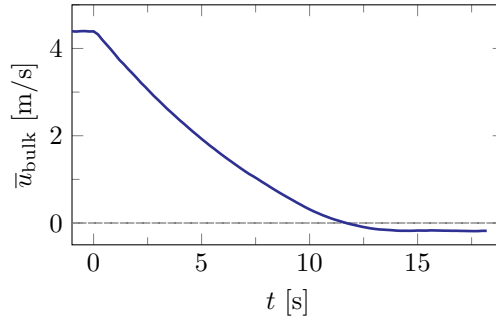


Fig. 3.8: Bulk velocity across the inlet at the spanwise center ($z = 0$) through time

The RoBuT room was configured with modern HVAC systems and thermal insulation for stable conditions. Controls were independent of other systems in the building. The refrigerated air conditioning had a $\sim 0.56^\circ\text{C}$ (1°F) deadband. The maximum measured temperature spread during data acquisition was 0.9°C ($\sim 1.6^\circ\text{F}$). To reduce the rate of temperature change from the on/off behavior of this system, outside air was mixed with refrigerated air before being injected into the room. Heating was performed with a steam heat exchanger with attached fan. The original fan and control system were replaced with a variable speed, tuned, PI-controlled system implemented with the main LabVIEW program, giving the heating system tight control of the room temperature.

3.7 System Response Quantities

The SRQs are the experimental results used to compare with simulation outputs and were listed in Table 3.1. They are included for all phases of the transient and include uncertainty on all results. Since they are similar, the ensemble-average and fluctuating velocity profiles in the form of Reynolds stresses are presented together. Additionally scalars of wall heat flux and wall shear stress are also included.

3.7.1 SRQ Description

Profiles of streamwise velocity \bar{u} and Reynolds normal stress $\overline{u'u'}$ are shown in Fig. 3.9 at three locations in x for the top (x_1), middle (x_2), and bottom (x_3). The boundary layer thickness increases in the streamwise direction x as evidenced in both the \bar{u} and $\overline{u'u'}$ profiles at the initial condition as expected. The velocity profile shape generally remains similar but is reduced in magnitude during the first four seconds. At $t = 8$ s, the contribution from natural convection begins affecting the profiles near the heated wall ($y = 0$). At $t = 12$ s the profiles show a strong influence from natural convection. The changes from $t = 12 - 16$ s are subtle as

steady natural convection is asymptotically reached. The results for Reynolds normal stress $\overline{u'u'}$ show larger uncertainty, but this is expected as fluctuations are more challenging to quantify than averages. Initially $\overline{u'u'}$ is elevated near both walls as expected. The influence of natural convection increases $\overline{u'u'}$ near the heated wall initially. The area of elevated $\overline{u'u'}$ moves away from the wall over time. The phase of $t = 12$ s has the highest levels, likely from a chaotic flow reversal. The final measured state has reduced stresses and may still be decreasing.

Uncertainty of the PIV results was calculated from the Uncertainty Surface Method which estimates instantaneous bias and random uncertainties due to the effects of particle displacement, particle image density, particle image size, and shear originally described in [19] and improved upon with methods from [17]. The uncertainties of the velocity statistics propagated from the instantaneous uncertainties were calculated by methods of Wilson & Smith [20]. Total uncertainty was calculated as in Eqn. 3.7. The confidence level on all UQ results in this work is 95%.

Previous methods to quantify wall shear have fit experimental velocity data with empirical correlations such as Spalding or Musker profiles with high accuracy [21]. This method works well for steady boundary layer data where the profiles are an accurate representation of velocity, but not for the transient conditions in the current study. Therefore wall shear stress was estimated directly from PIV data as $\tau_s = \mu \frac{\partial \bar{u}}{\partial y} \big|_{y=0}$ where τ_s is wall shear stress and μ is dynamic viscosity. High-resolution PIV data were used to fit a line to velocity data where $y^+ = y u_\tau / \nu \leq 5$ for $\frac{\partial \bar{u}}{\partial y} \big|_{y=0}$, where $u_\tau = \sqrt{\tau_s / \rho}$ and ρ is the fluid density [14]. Initially 10 points were included in the fit and a stable iterative method was used to calculate τ_s and the number of data points to fit within $y^+ \leq 5$. The wall was located by the particle images with a mask carefully defined. The linear fit was performed using linear regression with more weight given to velocity data with lower uncertainty [22]. The high-resolution PIV data at x_2 and associated linear fit are shown in Fig. 3.10 for five phases of the transient. The fit was not forced to the wall as wall location errors would be compounded and not easily quantifiable in the uncertainty estimation. The dynamic viscosity was evaluated using Sutherland's Law at the wall temperature. The fit uncertainty was combined with the viscosity uncertainty using the Taylor Series Method [18].

Results for the scalars of wall heat flux and wall shear stress are shown in Fig. 3.11 at the same three x locations through time with their associated uncertainty bands. The experimental heat flux came from the Heat Flux Sensors (HFSs) using the manufacturer-calibrated sensitivity. The uncertainty included 5% bias while the random values were measured. The experimental results from the HFSs show a low sensitivity to convection due to the thermal capacitance of the heated wall in which they were embedded. The wall shear

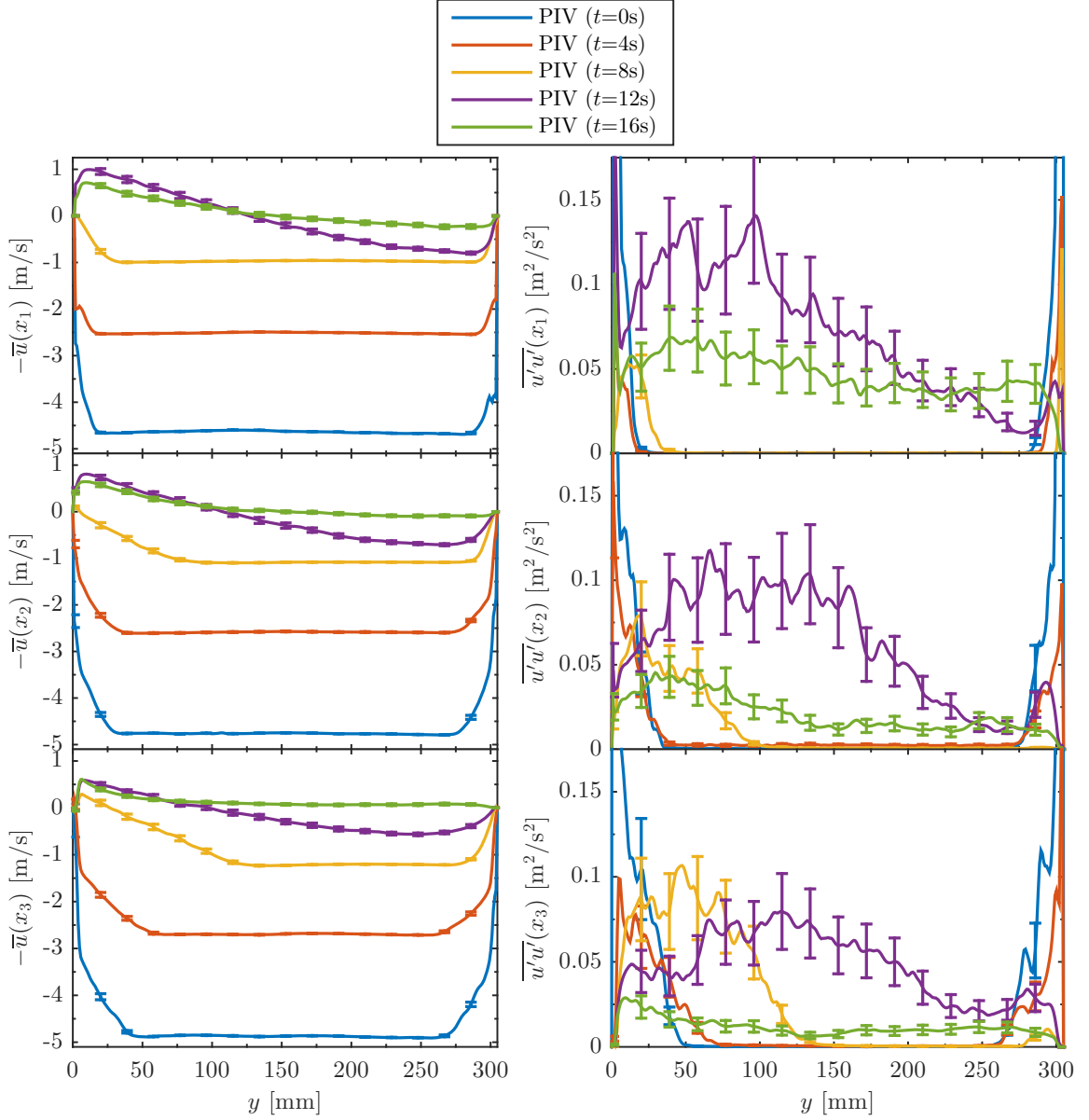


Fig. 3.9: The streamwise velocity \bar{u} and Reynolds normal stress $\overline{u'u'}$ at three locations in x and five phases of the transient

results are somewhat noisy at high levels of shear, likely from the decreased accuracy of PIV data near walls with large velocity gradients and the relatively lower number of points in the fit. When the shear decreases, more points can be used in the fit for smoother results with decreased uncertainty. The shear smoothly changes sign as the near-wall flow reverses.

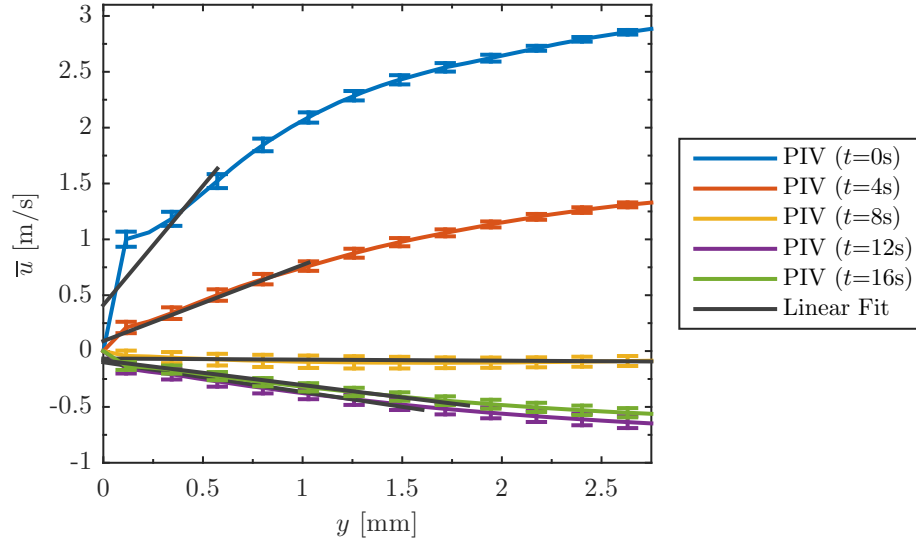


Fig. 3.10: High-resolution PIV data near the heated wall with linear fit

3.7.2 SRQ Data

Like the BC data, the SRQ data and their uncertainties are tabulated for use in validation studies. They are contained in comma separated files with the *.csv extension and can be opened in a spreadsheet program or a simple text editor. All resulting PIV data are made available from both cameras with headers similar to the BC PIV data presented earlier. They contain data at all three x locations as specified in the files. As with the BC data, the full uncertainties at 95% confidence are provided with unique positive and negative uncertainties for Reynolds stresses. The small FOV data are found in the file [Trans-SRQ-Vel-SmallFOV](#) and the large FOV in [Trans-SRQ-Vel-LargeFOV](#).

Wall heat flux results are given for all three sensors along x with specified bias, random, and total uncertainty and found in the file [Trans-SRQ-HeatFlux](#). Wall shear is similarly formatted, has the total uncertainty, and is found in the file [Trans-SRQ-Shear](#).

3.8 Conclusions

This paper presented the study of a ramp-down flow transient with heat transfer and buoyancy effects in simplified geometry to provide CFD validation data. Repeated runs provide high resolution data for ensemble-averaging and turbulent statistics of high resolution data. The provided BCs and SRQs, listed in Table 3.1 for the conditions in Table 3.2, are tabulated and available for download. Uncertainty is also included for all presented data. The data contain rich and comprehensive coverage of this flow. They enable

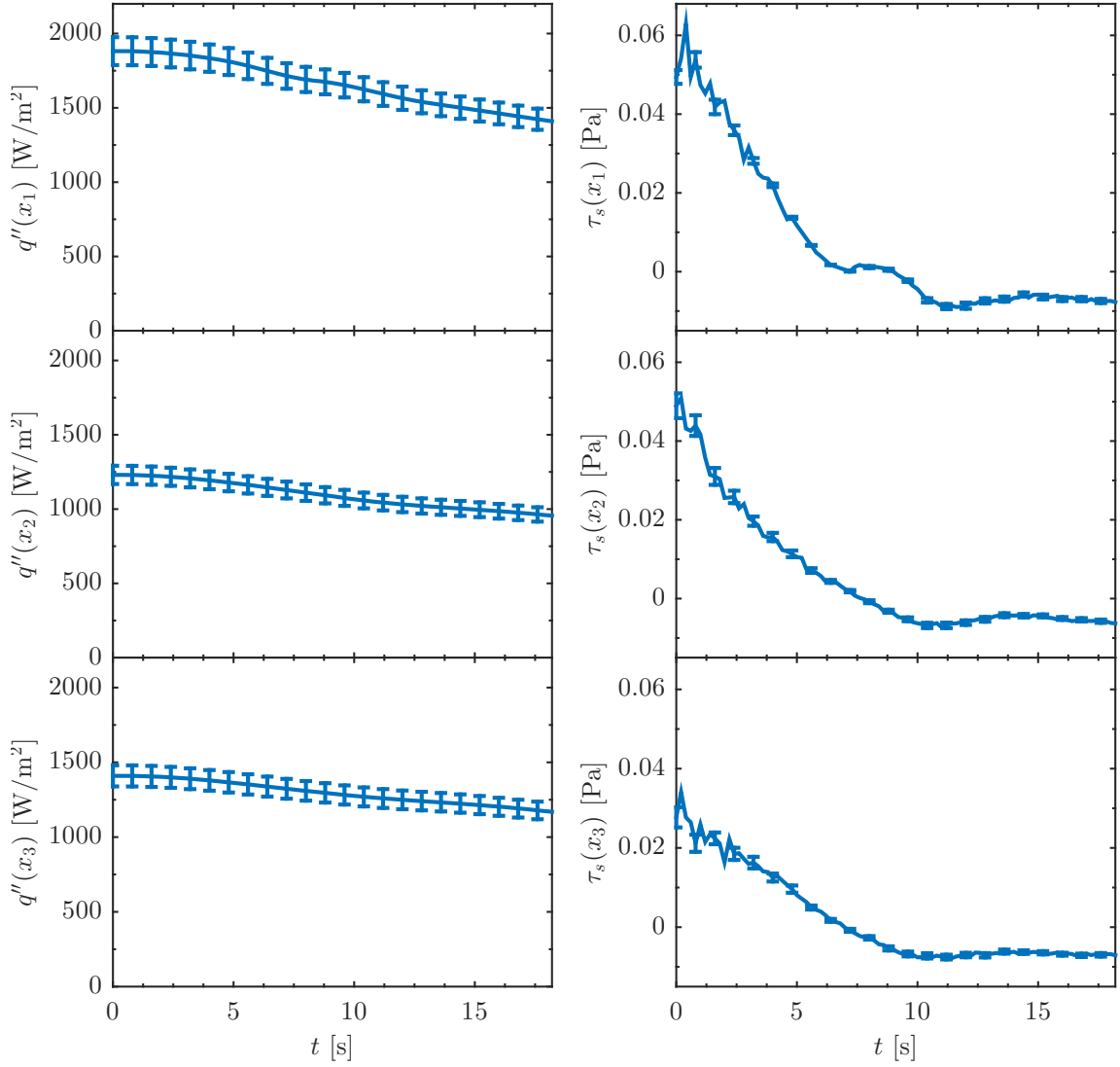


Fig. 3.11: The heated wall heat flux and wall shear stress plotted over time

validation studies to assess model accuracy and are necessary to calculate simulation uncertainty.

Acknowledgments

This research was performed using funding received from the DOE Office of Nuclear Energy's Nuclear Energy University Programs, and their support is gratefully acknowledged. Also, the authors appreciate Dr. Nam Dinh who originally suggested transient convection for CFD validation.

References

- [1] Oberkampf, W. L., and Smith, B. L., 2014, “Assessment Criteria for Computational Fluid Dynamics Validation Benchmark Experiments,” 52nd Aerospace Sciences Meeting of AIAA.
- [2] Harris, J. R., Lance, B. W., and Smith, B. L., 2015, “Experimental Validation Data for Computational Fluid Dynamics of Forced Convection on a Vertical Flat Plate,” *Journal of Fluids Engineering*, **138**(1), p. 011401, doi:[10.1115/1.4031007](https://doi.org/10.1115/1.4031007).
- [3] Oberkampf, W. L., and Roy, C. J., 2010, *Verification and Validation in Scientific Computing*, Cambridge University Press, doi:[10.1017/cbo9780511760396](https://doi.org/10.1017/cbo9780511760396).
- [4] ASME, 2009, “ASME V&V 20-2009: Standard for Verification and Validation in Computational Fluid Dynamics and Heat Transfer,” Standard, American Society of Mechanical Engineers.
- [5] Roache, P. J., 2009, *Fundamentals of Verification and Validation*, Hermosa Publ.
- [6] AIAA, 1998, “Guide for the Verification and Validation of Computational Fluid Dynamics Simulations,” Tech. Rep. AIAA G-077-1998, American Institute of Aeronautics and Astronautics, Reston, VA, doi:[10.2514/4.472855](https://doi.org/10.2514/4.472855).
- [7] He, S., and Jackson, J. D., 2000, “A Study of Turbulence Under Conditions of Transient Flow in a Pipe,” *Journal of Fluid Mechanics*, **408**, pp. 1–38, doi:[10.1017/s0022112099007016](https://doi.org/10.1017/s0022112099007016).
- [8] Koshkin, V., Kalinin, E., Dreitser, G., Galitseisky, B., and Izosimov, V., 1970, “Experimental Study of Nonsteady Convective Heat Transfer in Tubes,” *International Journal of Heat and Mass Transfer*, **13**(8), pp. 1271–1281, doi:[10.1016/0017-9310\(70\)90068-2](https://doi.org/10.1016/0017-9310(70)90068-2).
- [9] Kataoka, K., Kawabata, T., and Miki, K., 1975, “The Start-up Response of Pipe Flow to a Step Change in Flow Rate,” *Journal of Chemical Engineering of Japan*, **8**(4), pp. 266–271, doi:[10.1252/jcej.8.266](https://doi.org/10.1252/jcej.8.266).
- [10] Maruyama, T., Kuribayashi, T., and Mizushima, T., 1976, “The Structure of the Turbulence in Transient Pipe Flows,” *Journal of Chemical Engineering of Japan*, **9**(6), pp. 431–439, doi:[10.1252/jcej.9.431](https://doi.org/10.1252/jcej.9.431).
- [11] Rouai, N. M., 1987, “Influence of Buoyancy and Flow Transients on Turbulent Convective Heat Transfer in a Tube,” Ph.D. thesis, University of Manchester, UK.
- [12] Jackson, J. D., Büyükalaca, O., and He, S., 1999, “Heat Transfer in a Pipe Under Conditions of Transient Turbulent Flow,” *International Journal of Heat and Fluid Flow*, **20**(2), pp. 115–127, doi:[10.1016/s0142-727x\(98\)10056-5](https://doi.org/10.1016/s0142-727x(98)10056-5).
- [13] Barker, A. R., and Williams, J. E. F., 2000, “Transient Measurements of the Heat Transfer Coefficient in Unsteady, Turbulent Pipe Flow,” *International Journal of Heat and Mass Transfer*, **43**(17), pp. 3197–3207, doi:[10.1016/s0017-9310\(99\)00305-1](https://doi.org/10.1016/s0017-9310(99)00305-1).
- [14] Kays, W. M., Crawford, M. E., and Weigand, B., 2012, *Convective Heat and Mass Transfer*, 4th ed., McGraw-Hill.
- [15] Kähler, C. J., Sammler, B., and Kompenhans, J., 2002, “Generation and Control of Tracer Particles for Optical Flow Investigations in Air,” *Experiments in Fluids*, **33**, pp. 736–742, doi:[10.1007/s00348-002-0492-x](https://doi.org/10.1007/s00348-002-0492-x).
- [16] Touloukian, Y. S., and Ho, C. Y., 1977, *Thermophysical Properties of Selected Aerospace Materials Part II: Thermophysical Properties of Seven Materials*, Purdue University, West Lafayette.
- [17] Warner, S. O., and Smith, B. L., 2014, “Autocorrelation-based Estimate of Particle Image Density for Diffraction Limited Particle Images,” *Measurement Science and Technology*, **25**(6), p. 065201, doi:[10.1088/0957-0233/25/6/065201](https://doi.org/10.1088/0957-0233/25/6/065201).

- [18] Coleman, H. W., and Steele, W. G., 2009, *Experimentation, Validation, and Uncertainty Analysis for Engineers*, John Wiley & Sons, doi:[10.1002/9780470485682](https://doi.org/10.1002/9780470485682).
- [19] Timmins, B. H., Wilson, B. W., Smith, B. L., and Vlachos, P. P., 2012, "A Method for Automatic Estimation of Instantaneous Local Uncertainty in Particle Image Velocimetry Measurements," *Experiments in Fluids*, **53**(4), pp. 1133–1147, doi:[10.1007/s00348-012-1341-1](https://doi.org/10.1007/s00348-012-1341-1).
- [20] Wilson, B. M., and Smith, B. L., 2013, "Taylor-series and Monte-Carlo-method Uncertainty Estimation of the Width of a Probability Distribution Based on Varying Bias and Random Error," *Meas. Sci. Technol.*, **24**(3), p. 035301, doi:[10.1088/0957-0233/24/3/035301](https://doi.org/10.1088/0957-0233/24/3/035301).
- [21] Kendall, A., and Koochesfahani, M., 2007, "A Method for Estimating Wall Friction in Turbulent Wall-bounded Flows," *Exp Fluids*, **44**(5), pp. 773–780, doi:[10.1007/s00348-007-0433-9](https://doi.org/10.1007/s00348-007-0433-9).
- [22] Bevington, P. R., and Robinson, D. K., 2003, *Data Reduction and Error Analysis*, McGraw–Hill, New York.

CHAPTER 4

WALL HEAT FLUX MEASUREMENTS IN A CONVECTING BOUNDARY LAYER

Abstract

Wall heat flux measurements were made by measuring the temperature gradient in air very near a heated plate under convection conditions. Air thermal conductivity was predicted using the locally-measured temperature and reference data. A fine-wire thermocouple probe was designed, built, and used for these measurements and has the ability to self-align to the surface. Commercial sensors that were potted inside the plate were compared with this first-principles method for accuracy assessment.

4.1 Introduction

Heat flux is one desirable measurement for computational fluid dynamics (CFD) validation experiments performed with the Rotatable Buoyancy Tunnel (RoBuT) at Utah State University. Model Validation is done by matching inputs and comparing outputs of experiments and simulations. Simulation accuracy can be assessed by this comparison. Validation is more rigorous with derivative quantities such as heat flux as they are more susceptible to experimental noise and numerical errors compared to integral quantities [1].

Validation experiments are the main purpose of the RoBuT, whose major flow components are shown in Fig. 4.1. The components shown were mounted in a rotating ‘Ferris wheel’ structure to change the relative direction of natural convection and forced convection. The test section had three clear walls for optical access and one heated wall for a convection boundary condition. The cross section was 0.305 m square and the test section 2 m long. Three thin-film heat flux sensors (HFSs) from RdF Corporation were potted inside the heated wall in the streamwise (x) direction at the spanwise center. These sensors were based on the spatial temperature gradient method and are shown, along with the many layers of the heated wall, in Fig. 4.2.

The sensors were model 20457-3 and had a thermopile around a Kapton® substrate. The manufacturer supplied unique calibration coefficients for each sensor. The manufacturer-specified uncertainty was 5% of reading. An embedded Type T thermocouple (TC) was used to measure sensor temperature. This temperature was used to correct readings for changes in thermal conductivity of the substrate with a multiplication factor curve. The HFSs were placed adjacent to the Kapton® layer of similar thermal resistance to reduce measurement errors by non-uniform conduction paths. An initial thermal resistance network analysis between HFS

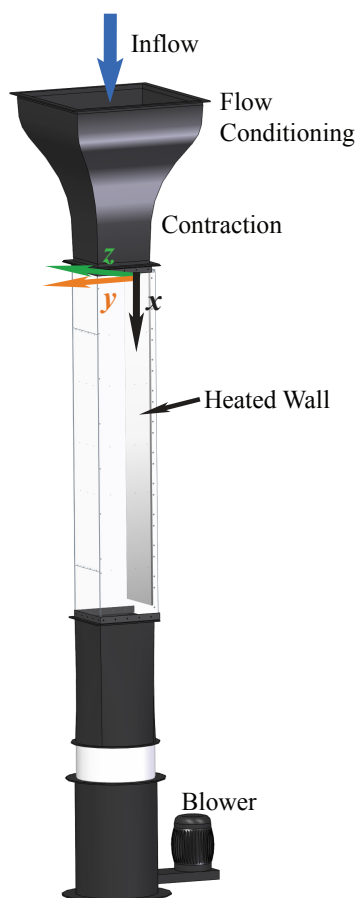


Fig. 4.1: Important flow components of the Rotatable Buoyancy Tunnel

and non-HFS conduction paths showed only a 2.4% difference in heat flux.

Preliminary experiments have shown that the measured heat flux does not match fundamental trends as shown in Fig. 4.3, specifically decreasing heat flux with boundary layer development with increasing x . Two correlations are shown with the experimental results [2, 3]. The correlation trends are not smooth, a result of the measured center-line wall temperature, which has small gradients. The trend was concerning and it was possible that the sensor sensitivities were mixed-up, the sensors had an installation error, or other manufacturer-supplied parameters were incorrect. As heat flux was important to this experiment, developing a means to assess sensor accuracy and possibly quantify errors was desired. Since they were potted inside the heated wall, only in-situ methods were possible without damaging the heated wall.

Installation error is possible if heat transfer conditions were different between calibration and use. The RdF sensors were calibrated to a reference sensor that was calibrated at 70°F in radiation using a blackbody

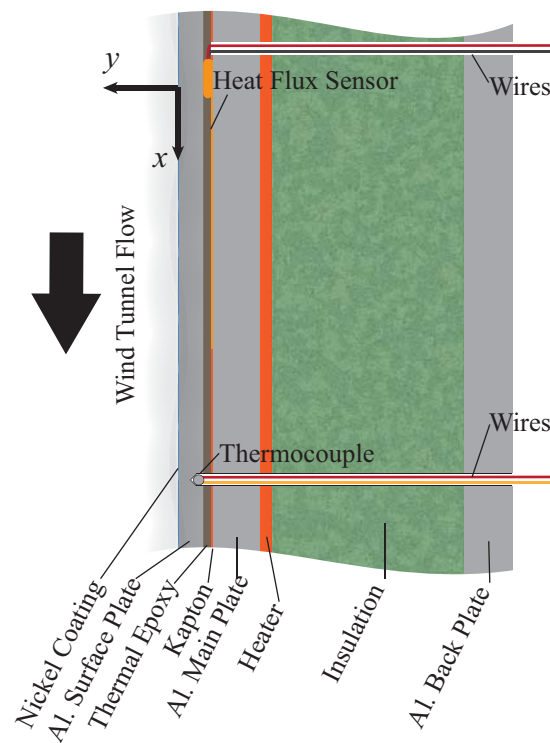


Fig. 4.2: Heated wall cross section with relative thicknesses to scale. The HFS label is near the top.

source [4]. Since the sensors were potted in the heated wall, the heat transfer mode was conduction. The different heat transfer modes, the elevated operation temperature, and the possibility of non-uniform thermal resistance in the sensor area have been identified as possible error sources [5].

4.2 Theory

Heat flux measurements can be challenging due to the complex thermal environments involved and multi-mode heat transfer which is often present. All known sensors are intrusive and are likely to disrupt thermal conditions where they are placed. Several commercial sensor options are available, but care must be taken to maintain uniform thermal resistance around the sensors [6].

The three main methods for measuring heat flux are based on: 1) spatial temperature gradients, 2) temperature change with time, and 3) surface heating [6]. The spatial temperature gradient method is used in the purchased RdF thin-film sensors. Adding a reference HFS of this type to the surface would disrupt local convection conditions. The calorimeter method uses heat storage over time to measure flux, but this assumes the temperature throughout the body is uniform. The heated wall was likely to have temperature

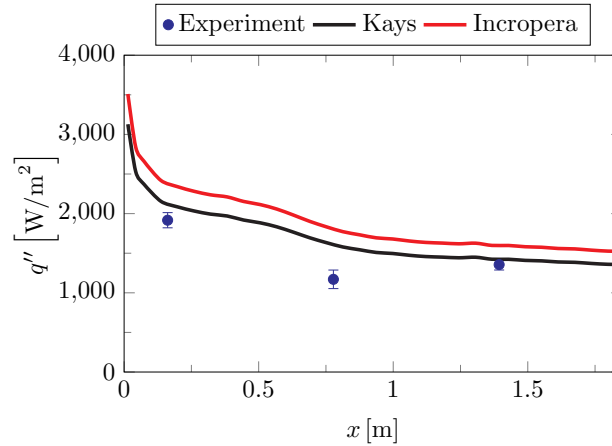


Fig. 4.3: Wall heat flux measurements with two correlations

gradients through the thickness, especially in the epoxy where the thermal conductivity was about 1/100 of that of the adjacent aluminum. Temperature gradients were also likely in both spanwise directions. Surface heating methods were not well developed nor described and were not a good option.

Sensors based on spatial temperature gradients are common and will be described in greater detail. Fourier's law is essential to their operation and is

$$q'' = -k \frac{dT}{dy} \approx -k \frac{\Delta T}{\Delta y} \quad (4.1)$$

where q'' is heat flux, k is the substrate thermal conductivity, T is temperature, and y is the direction of heat flux [3]. The temperature gradient is often estimated by a differential temperature measurement (ΔT) across a thermopile (array of differential TCs) across a substrate, such as in the RdF sensors. Generally, the substrate thickness (Δy) and thermal conductivity are not known accurately enough for the overall desired accuracy, so sensor calibration is commonly performed.

An independent heat flux measurement technique was desirable to assess the accuracy of the potted HFSs. The HFSs measured heat flux near the surface of the heated wall. The convective heat flux from the wall to the air should be equivalent, especially very near the wall and departed from the side walls. Radiation heat transfer was minimized by the nickel plating on the heated wall meant to reduce thermal radiation. The predicted and measured emissivity was around 0.03 [7]. Very near the wall, within the inner portion of the viscous sublayer, the temperature profile should be linear [2]. If the temperature profile can be measured within this region and the thermal conductivity of air k can be estimated by the measured temperature and

reference data [8], convective heat flux measurements from a surface are possible.

Others have made near-wall temperature measurements. An early study by Warner and Arpaci used a butt-welded TC probe of $12.7\ \mu\text{m}$ diameter oriented parallel to a vertical flat plate and perpendicular to the flow direction. It was traversed with a motor-driven carriage near the heated wall under turbulent natural convection. The position was accurate to $5.08\ \mu\text{m}$ within the first $25.4\ \text{mm}$ and to $15.2\ \mu\text{m}$ farther from the wall. They were able to measure temperature profiles and subsequently heat flux [9]. In another study of a turbulent boundary layer under forced convection, temperature profiles were measured by a TC probe of $76.2\ \mu\text{m}$ diameter and about $12.7\ \text{mm}$ long suspended by 22-gauge hypodermic needles oriented parallel to the plate and perpendicular to the flow direction. This probe was also traversed with a mechanism that was accurate to $25.4\ \mu\text{m}$. These results, along with velocity measurements, were used to present many heat flux, shear, and turbulent Prandtl number results for this canonical flow [10].

4.3 Method

An independent heat flux measurement was conceived to assess the accuracy of the HFSs inside the heated wall. After several iterations of design and testing, the final sensor was able to measure heat flux with an uncertainty of less than 10% while disrupting the actual heat flux only moderately. The design was based on the spatial temperature gradient like the thin-film sensors, but measured heat flux in air very near the heated wall. The heat transfer inside the wall was by conduction. At the surface, heat transfer was mainly due to convection. As mentioned previously, thermal radiation from the heated wall was minimized by a nickel coating.

The sensor design was similar to that used by Blackwell *et al.* [10] and was a TC oriented parallel to the wall and perpendicular to the flow direction. The new design is shown in Fig. 4.4 with the pivot, brace, and TC junction identified. The junction of the probe was formed by type K wires of diameter $D_{\text{TC}} = 0.051\ \text{mm}$ from Omega Engineering. The two lead wires were aligned parallel to the wall with a length of $15.3\ \text{mm}$ ($\sim 300D_{\text{TC}}$) to reduce conduction losses. The junction was formed by spot welding overlapping wires. After welding, the wire was pulled tight and epoxied in place. The fine wire was welded to thicker 0.511-mm wire that spanned the pivot and was connected to the data acquisition system (DAQ). The brace was rigid enough to keep the wire tight and made of plastic for small conduction losses.

The pivot allowed the probe to self-align to the wall prior to each acquisition, reducing measurement errors. Alignment was done by moving the probe into the wall until both ends of the brace were pressed firmly and any angle corrected, then pulling the probe away from the wall. The alignment process is shown

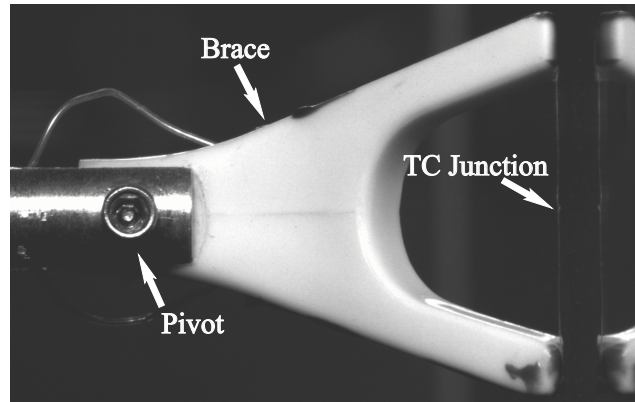


Fig. 4.4: TC Probe with its reflection in the heated wall on the right

in Fig. 4.5 and involves three steps.

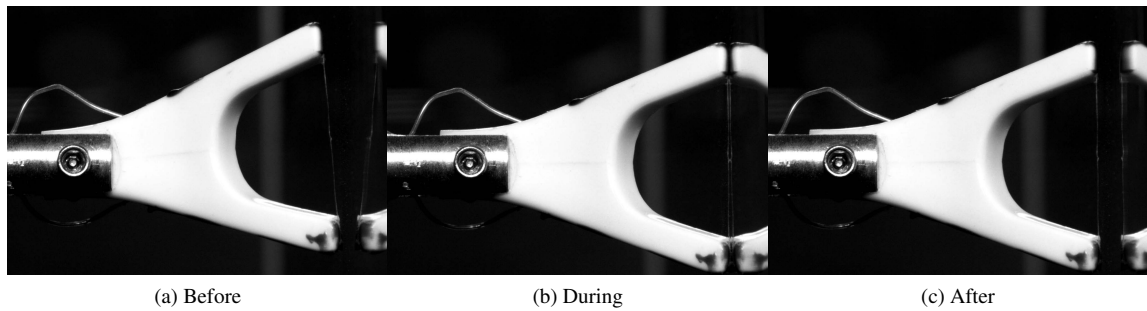


Fig. 4.5: Self-alignment process of the TC Probe with the heated wall

The pictured head of the TC probe was supported by a stainless steel tube with 3.76-mm outside diameter that spanned the test section and exited the wall opposite the heated wall. This tube contained the TC wires and was connected to a Velmex Inc. UniSlide[®] traverse model B4015Q2J. This traverse was used for small, incremental movements such as 200 μm . The distance from the wall was estimated by fitting a line to the measured temperature profile very near the wall to the temperature of the wall measured by embedded TCs. The largest uncertainty in position resulted from the stepper motor resolution. With 200 steps/rev. and assuming 1/2 step resolution, the uncertainty was 2.5 μm . The pitch uncertainty was much smaller at 0.04 mm/25.4 cm or 0.0315 μm for a 200 μm step. Traverse backlash should not be a problem since traversing was done in one direction only and the first point was ignored.

The probe was used in the spanwise center of the test section, directly over the three potted HFSs. Three 25.4 mm access ports were drilled into the wall opposite the heated wall at the x locations of the HFSs. Once

inserted, a collar was used to support the probe tube and fill the port gap. The x locations of the HFSs and the ports were $x_1 = 16.2$ cm, $x_2 = 77.8$ cm, and $x_3 = 139$ cm from the inlet to the test section. These three positions were used for analysis throughout this work.

The output voltages of the TCs and HFSs were small, so specialized DAQ devices were selected. National Instruments (NI) products were used as they interfaced well with the LabVIEW software that was used for system control and thermal data recording. All TCs and HFSs were measured with NI-9213 TC modules. The narrow voltage range of ± 78 mV, 24-bit ADC, and open channel detection capability made them well suited for these measurements. The built-in CJC was used for TCs.

The TC probe was not calibrated, so the standard bias uncertainty of 2.2°C for type K TCs was used. The bias uncertainty of the DAQ was 0.8°C , resulting in overall bias uncertainty as

$$B_{\bar{T}} = \sqrt{B_{\text{TC}}^2 + B_{\text{DAQ}}^2} = 2.34^\circ\text{C}. \quad (4.2)$$

The random uncertainty was calculated from the data as

$$S_{\bar{T}} = t_{95} \frac{S_T}{\sqrt{N}} \quad (4.3)$$

where t_{95} is the confidence level coefficient (taken as 1.96 for 95% confidence and number of samples $N > 30$) and S_T is the sample standard deviation. Bias and random sources were combined as

$$U_{\bar{T}} = \sqrt{B_{\bar{T}}^2 + S_{\bar{T}}^2}. \quad (4.4)$$

The probe may be subject to conduction losses that could lead to measurement error. Accordingly, this error was estimated using a 1-D fin equation with non-uniform ambient temperature. Velocity profiles were measured at the three x locations by Particle Image Velocimetry (PIV) under the same conditions but with the probe removed. The measured temperature and velocity profiles were used to estimate fluid properties and heat transfer coefficients. Heat conduction was considered from the TC junction through the wires that were parallel with the heated wall. Then combined conduction and convection were considered in the wires departing from the wall to the lower temperature air. The epoxy in this area would have an insulating effect on the potted wires, reducing errors, but this effect was conservatively neglected. The largest predicted error from losses was estimated at 0.03°C at the wall at x_1 .

Two convection conditions were measured, forced and mixed. In forced convection, buoyancy forces

were small compared to pressure forces and the effects of natural convection were practically negligible. Mixed convection, however, had natural convection forces similar in magnitude to pressure forces. The forced flow was downward, creating buoyancy-opposed mixed convection where forces of natural and forced convection are in opposite directions [3]. The wall temperature was about 140°C for both cases. The bulk velocities were 4.31 and 2.44 m/s for forced and mixed convection respectively. The flow was only partially-developed in the test section, so the physics were more like external than internal flow.

In addition to forced and mixed convection tests at the three x locations, tests were performed to isolate the error source of the HFS readings. Factorial experiments from Design of Experiments (DOE) were implemented [11]. Data were acquired and errors quantified at the farthest downstream location at x_3 with the TC probe. Three parameters were changed during the tests: air velocity, axial conduction in the heated wall, and temperature magnitude of the heated wall. The values used for these parameters are shown in Table 4.1 for the ten cases. Axial conduction was prescribed by independently controlling the temperature in three heating zones in the streamwise direction. The variation of these parameters is depicted in Fig. 4.6 with two levels of temperature and velocity and three for axial conduction. Extending the parameters to twelve cases was desirable but not feasible. The two velocity levels correspond to forced and mixed convection. The cases numbered 1–10 represent unique combinations of the three parameters with relative magnitudes properly shown on the three axes. The order of these tests was randomized for measurement independence and repeated three times to determine the level of repeatability. Results were averaged over the three repetitions.

Table 4.1: Parameters for the Design of Experiment study

Case	\bar{u}_{bulk} [m/s]	$\partial T / \partial x$ [°C/m]	T_{max} [°C]
1	4.31	0	120
2	2.44	0	120
3	2.44	0	80
4	4.31	0	80
5	4.31	32.5	120
6	2.44	32.5	120
7	2.44	32.5	80
8	4.31	32.5	80
9	4.31	64.9	120
10	2.44	64.9	120

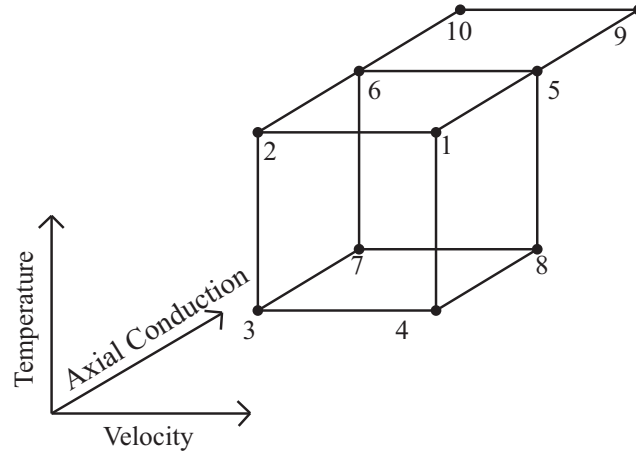


Fig. 4.6: Factorial sketch of the DOE study

4.4 Results

The measured temperature profiles from the TC probe for both forced and mixed convection are shown in Fig. 4.7. The spatial resolution of the first eight points was $200\mu\text{m}$. Subsequent spacing increases with increasing distance from the heated wall and the last several points measured the free-stream temperature. The development of the thermal boundary layer is observable in x in both cases and the larger boundary layer is seen for the mixed case (lower velocity) as expected. Each location is the time mean of 250 points acquired at 15 hz. The traverse started the probe head at the heated wall and pulled it away, allowing several seconds for each move and for the probe to come into thermal equilibrium.

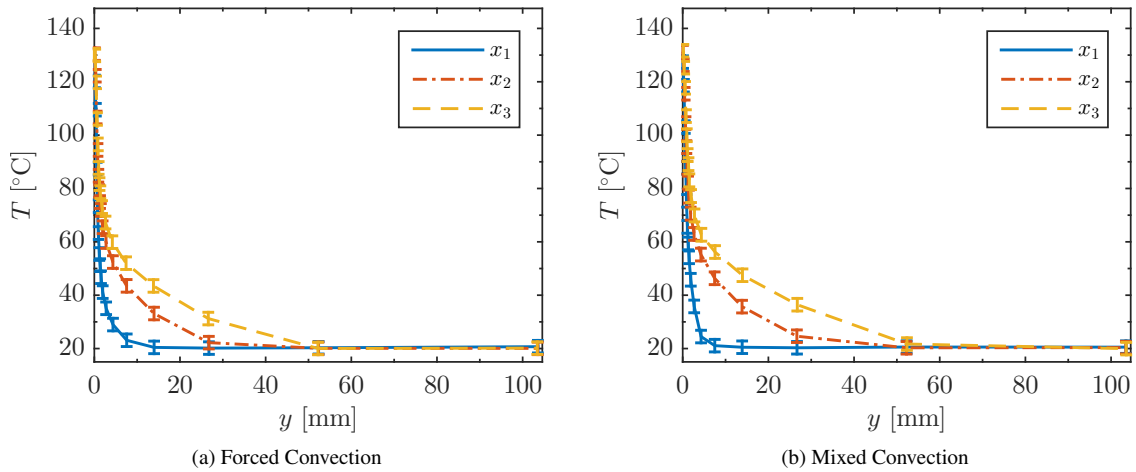


Fig. 4.7: Measured temperature profiles for both cases and all three x locations

The same temperature data in the near-wall region and line fit are shown in Fig. 4.8. For the line fit, initially eight points were included in the fit and a stable iterative method was used to calculate the temperature gradient and the number of data points to fit within $y^+ \leq 6.6$, half the critical y^+ value for air. This ensured the fitted data were within the inner portion of the viscous sublayer where linear temperatures were expected. The first point was not considered as it is likely to have position error. Errors in wall position were corrected by taking the temperature gradient to the measured wall temperature. The linear fit was performed using linear regression with more weight given to data with lower uncertainty [12]. This method also provided a measure of the fit uncertainty.

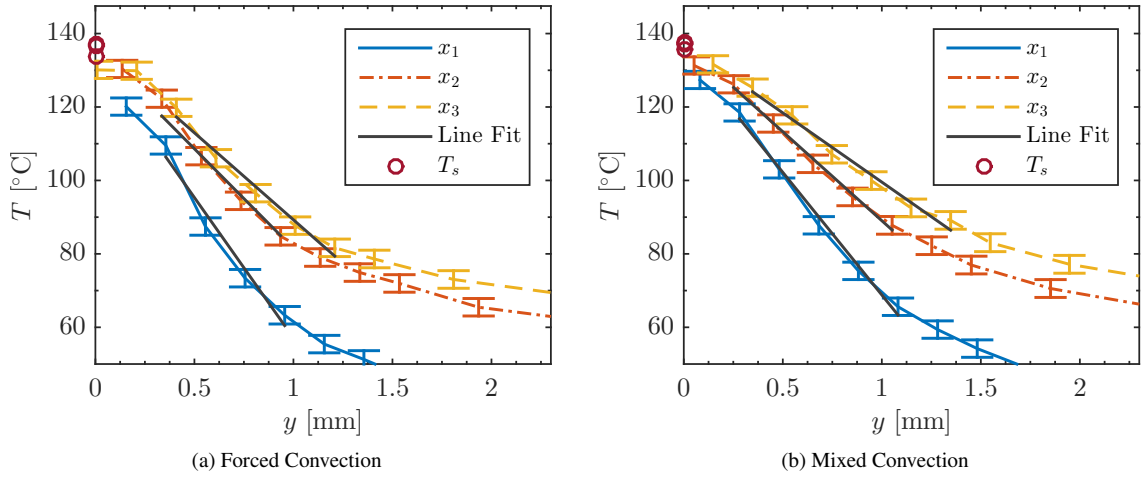


Fig. 4.8: Measured temperature profiles near the heated wall with line fit for both cases for all three x locations. Note the unique wall temperature values T_s as the wall is nearly isothermal. T_s at x_1 is several degrees cooler than at x_2 and x_3 .

Nondimensional profiles are shown and compared with the thermal law of the wall [2] in Fig. 4.9. The agreement is excellent for $y^+ \leq \sim 6$. The results in the buffer layer and fully turbulent region are about five below the expected values, likely due to the partially-developed nature of the measurement region. Temperature fluctuations are not presented as the mass of the TC wire rendered it insensitive to the higher frequencies in this flow. These frequencies were determined to be about 300–600 Hz with a 50.8- μm diameter tungsten hot-film probe with much less thermal mass.

The intrusive nature of the probe caused an increase in wall heat flux observable in the HFS data acquired at the time. The largest error of wall heat flux occurred when the probe was touching the heated wall and steadily decreased as the probe was retracted from the wall. Maximum errors of 9.84%, 9.90%, and 8.61%

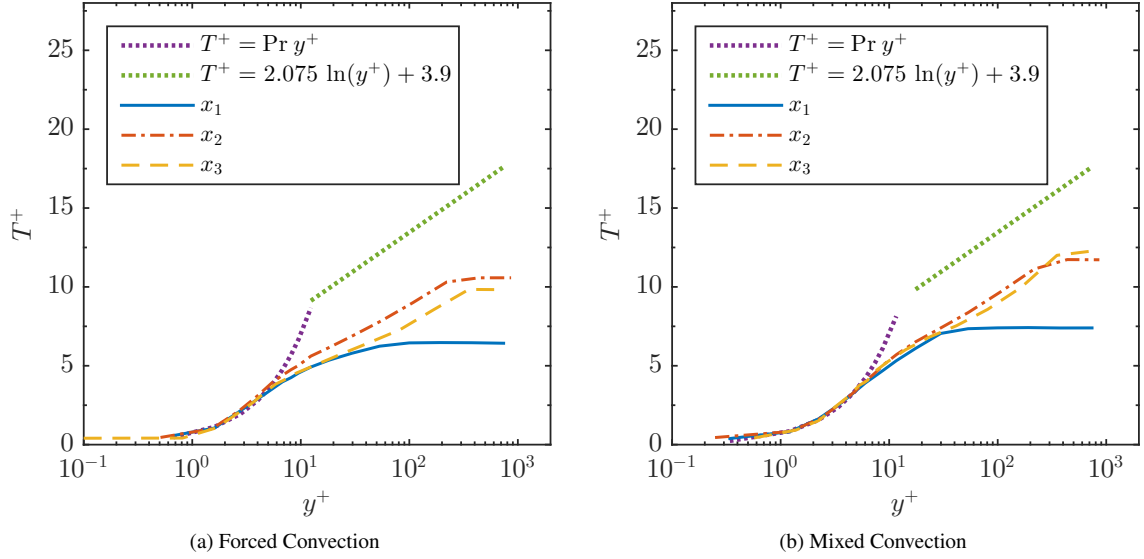


Fig. 4.9: Measured nondimensional temperature profiles with the thermal law of the wall for air for both cases and all three x locations

for the forced case and of 18.7%, 10.4%, and 7.93% for the mixed case were measured at locations x_1 , x_2 , and x_3 respectively. The likely cause of the heat flux increase is an increase in local turbulence levels caused by the probe. The forced convection case had very consistent errors and was fully turbulent as measured with PIV at a separate time in these conditions. The mixed convection case had a large range of error levels and was likely intermittently turbulent. In this case, the presence of the probe likely increased turbulence levels such as by a turbulence trip.

Published correlations for heat transfer can be used for comparison with both the HFS and TC probe results. First is turbulent forced convection over a flat plate. The local Stanton number correlation is

$$St = \frac{Nu_x}{Re_x Pr} = \frac{0.0287 Re_x^{-0.2}}{0.169 Re_x^{-0.1} (13.2 Pr - 9.25) + 0.85} \quad (4.5)$$

where Nu_x is the local Nusselt number, Re_x is the local Reynolds number, and Pr is the Prandtl number [2]. Once the Nusselt number is solved from this correlation, heat flux was calculated as $q'' = Nu_x k (T_s - T_\infty) / x$ where q'' is heat flux, k is fluid thermal conductivity, T_s and T_∞ are surface and free-stream temperatures respectively, and x is the streamwise distance from the leading edge.

As there are no known heat transfer correlations for mixed convection in developing channel flow, the correlation for fully developed turbulent flow in vertical tubes was used from the work of Jackson *et al.* [13]

as in

$$\frac{Nu}{Nu_F} = \left| 1 \pm \frac{10^4 Gr}{Re^{2.7} Pr^{0.5}} \right|^{0.46} \quad (4.6)$$

where Nu_F is the forced convection Nusselt number as calculated by Eqn. 4.5 and Gr is the Grashof number. The plus sign is used for buoyancy-opposed flows such as that investigated in this work while a minus sign applies to buoyancy-aided flows. Local values for Nu_x , $Nu_{F,x}$, Gr_x , and Re_x were used in place of the fully-developed variables.

As the boundary layers are partially developed at the inlet where $x = 0$, considering an unheated starting length was thought to improve agreement between measured values and correlations. This process required three calculations: 1) the momentum thickness at the inlet, 2) the distance upstream to a virtual origin, and 3) adjusting heat transfer correlations using the virtual origin as an unheated starting length. First the momentum thickness was calculated from PIV data at the spanwise center ($z = 0$) location at the inlet ($x = 0$) using the integral

$$\delta_2 = \int_0^\infty \frac{\bar{u}}{\bar{u}_\infty} \left(1 - \frac{\bar{u}}{\bar{u}_\infty} \right) dy \quad (4.7)$$

where δ_2 is the momentum thickness, \bar{u} is the time mean velocity across y , and \bar{u}_∞ is the time mean free-stream velocity [2]. Constant density has been assumed. This is a good approximation at the inlet which is upstream of the heated wall but would be inappropriate downstream where the near-wall air was heated. The boundary layers on both walls were considered and the result divided by two.

The calculation of a virtual origin was the second step and predicts the equivalent length of a flat plate extending upstream of the inlet. This allows for the impact of the contraction to be assessed simply, even though the geometry is very complex. Assuming the flow was always turbulent, the relationship has been derived as

$$\frac{\delta_2}{x} = \frac{0.036\nu^{0.2}}{\bar{u}_\infty^{0.2}x^{0.2}} = 0.036Re_x^{-0.2} \quad (4.8)$$

where ν is kinematic viscosity [2]. The left two portions can be arranged to isolate x as in

$$\xi = \frac{\delta_2^{1.25}\bar{u}_\infty^{0.25}}{0.0157\nu^{0.25}} \quad (4.9)$$

where ξ has been substituted for x and is the distance upstream to a virtual origin given δ_2 defined earlier. The results from the first two analyses are given in Table 4.2 for both cases. As expected, the momentum thickness is larger for mixed convection. It is reasonable to add these virtual origin distances to the x values in this work when comparing to more canonical flows. Also Re_x may be adjusted.

Table 4.2: Boundary layer analysis results from velocity data at the inlet

Parameter	Forced	Mixed
δ_2 [mm]	1.18	1.73
ξ [mm]	327	458

The third calculation was to adjust the correlation results for an unheated starting length with distances from the virtual origin analysis. The local Nusselt number was augmented by

$$\text{Nu}_x = \frac{\text{Nu}_x|_{\xi=0}}{\left[1 - (\xi/x)^{9/10}\right]^{1/9}} \quad (4.10)$$

where the local Nusselt number Nu_x and $\text{Nu}_x|_{\xi=0}$ was measured from the leading edge of the unheated starting length [3]. The adjusted flux values were slightly higher than the original, also an expected result.

Wall heat flux as measured by the HFSs and TC probe is shown in Fig. 4.10 with published correlations. The measured HFS trends in the streamwise direction x are inconsistent with expected results. The HFS at x_2 gives a smaller reading than that at x_3 for both cases. The likelihood that this error is real is supported by the monotonic decrease in the temperature gradient near the wall with streamwise distance x as observed in the TC probe results of Fig. 4.8. This decrease suggests a decrease in wall heat flux with x , consistent with theory. The TC probe results follow an expected trend and measured higher fluxes in both cases. The correlation prediction of heat flux uses the equations presented previously and the measured temperatures along the heated wall centerline. The first point very near $x = 0$ is low, attributable to the relatively cooler, insulated leading edge. The bump near $x = 0.5$ m in both cases is due to a temperature peak in the heated wall.

Heat flux results from the HFSs and TC probe are presented in numeric format in Table 4.3 for both cases and at all three x locations investigated. Taking the TC probe as the reference, HFS errors were quantified. Uncertainty at the 95% confidence level was calculated for all quantities, including the error. The errors are all negative as the HFS results are consistently low. The errors are moderately high, with the best agreement at x_3 . These results are consistent with the notion that measurements of derivative quantities are challenging and moderate errors can be expected.

The results of the DOE study were the flux errors of the HFSs relative to the TC probe. This study was performed at x_3 , where the errors were the smallest and the boundary layer the largest. The resulting errors are shown on the factorial sketch for cases 1–10 as shown in Fig. 4.11. The resulting errors show surprising

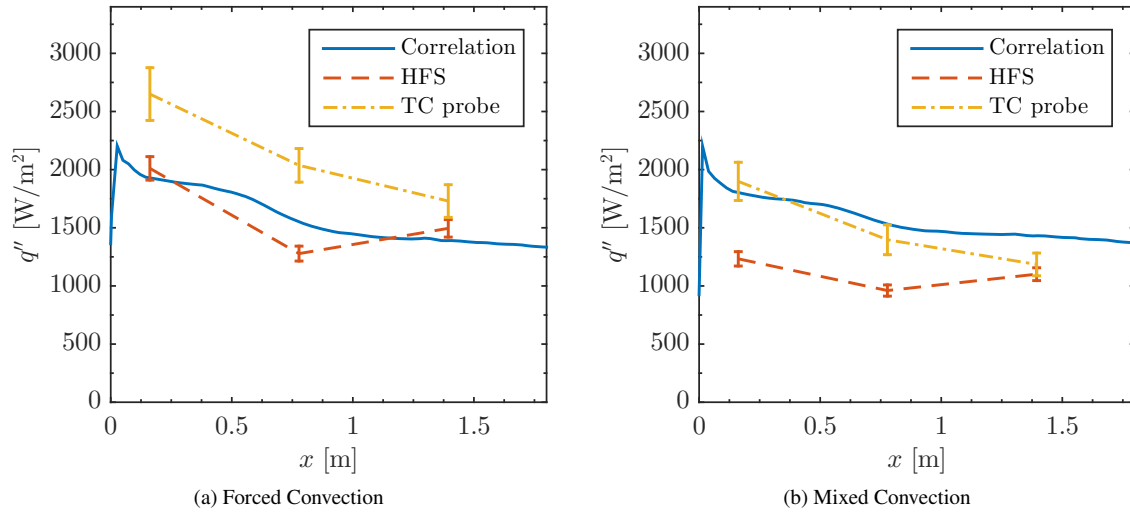


Fig. 4.10: Measured and predicted heat flux plotted in the streamwise direction

consistency around 20%. There is no apparent trend, suggesting that the error is relatively insensitive to the three parameters tested.

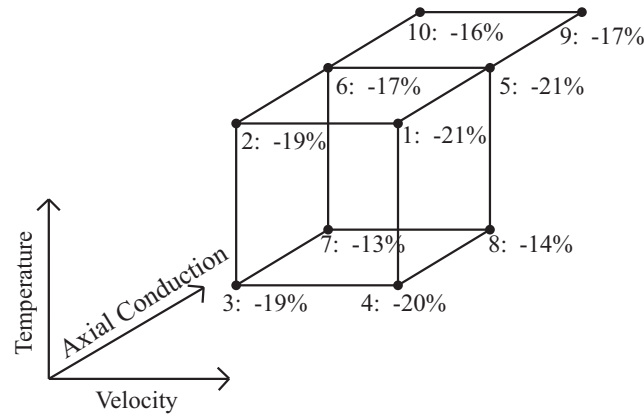


Fig. 4.11: Factorial sketch of the DOE study with errors

The consistency of these results suggests a constant bias to the error. Further investigation revealed that there may be non-uniform thermal resistance in the heated wall. After checking the thermal conductivity of Kapton[®] used adjacent to the HFSs, an error was found. The most likely thermal conductivity was 42% higher than the design value. Using a 1-D thermal circuit, the predicted error of the heat flux measurement due to spatial non-uniformity was -17.5% instead of 2.4% originally predicted. The results presented previously

Table 4.3: Heat flux results for both cases from the HFSs and the TC Probe results at all three x locations

		x [cm]	16.2	77.8	139
Forced	HFS	q'' [W/m ²]	2010	1280	1500
		$U_{q''}$ [%]	5.02	5.01	5.02
	TC Probe	q'' [W/m ²]	2650	2037	1730
		$U_{q''}$ [%]	8.56	7.09	8.12
	Error	ε [%]	-24.1	-37.2	-13.6
		U_{ε} [%]	7.53	5.45	8.25
Mixed	HFS	q'' [W/m ²]	1230	960	1101
		$U_{q''}$ [%]	5.01	5.01	5.01
	TC Probe	q'' [W/m ²]	1900	1400	1180
		$U_{q''}$ [%]	8.65	9.18	8.24
	Error	ε [%]	-35.1	-31.3	-7.06
		U_{ε} [%]	6.49	7.19	8.96

were not corrected from this information as there was a lack of confidence in either thermal conductivity specification.

4.5 Conclusions

The purpose of this work was to assess the accuracy of the commercial HFSs used in a validation experiment. These sensors were believed to be in error from an unknown source. An independent method of measuring heat flux in air near a heated wall under convection was developed and tested. The intrusive nature of the probe caused moderate errors in heat flux. The TC probe results, while possessing moderate uncertainties and flow disruptions, provide expected trends. A HFS error from non-uniform thermal resistance in the heated wall was identified. The probe results have known uncertainties and errors, while the HFSs have at least one unknown error remaining as evidenced by the illogical trends in the streamwise direction. The measured flux from the probe should be used for validation data while considering the limitations mentioned.

References

- [1] Oberkampf, W. L., and Roy, C. J., 2010, *Verification and Validation in Scientific Computing*, Cambridge University Press, doi:[10.1017/cbo9780511760396](https://doi.org/10.1017/cbo9780511760396).
- [2] Kays, W. M., Crawford, M. E., and Weigand, B., 2012, *Convective Heat and Mass Transfer*, 4th ed., McGraw-Hill.

- [3] Incropera, F. P., Dewitt, D. P., Bergman, T. L., and Lavine, A. S., 2007, *Fundamentals of Heat and Mass Transfer*, 6th ed., John Wiley & Sons.
- [4] RdF, 2014, “Heat Flow Measurement: Calibration, Specifications & Accuracy,” Tech. rep., RdF, corp.
- [5] Holmberg, D. G., and Womeldorf, C. A., 1999, “Performance and Modeling of Heat Flux Sensors in Different Environments,” ASME Heat Transfer Division, pp. 71–77.
- [6] Diller, T. E., 1999, *The Measurement, Instrumentation, and Sensors Handbook*, chap. 34, Heat Flux, CRC Press.
- [7] Harris, J. R., Lance, B. W., and Smith, B. L., 2015, “Experimental Validation Data for Computational Fluid Dynamics of Forced Convection on a Vertical Flat Plate,” *Journal of Fluids Engineering*, **138**(1), p. 011401, doi:[10.1115/1.4031007](https://doi.org/10.1115/1.4031007).
- [8] Touloukian, Y. S., Liley, P. E., and Saxena, S. C., 1970, “Thermophysical Properties of Matter-The TPRC Data Series. Volume 3. Thermal Conductivity-Nonmetallic Liquids and Gases,” Tech. rep., DTIC Document.
- [9] Warner, C. Y., and Arpaci, V. S., 1968, “An Experimental Investigation of Turbulent Natural Convection in Air at Low Pressure Along a Vertical Heated Flat Plate,” *International Journal of Heat and Mass Transfer*, **11**(3), pp. 397–406, doi:[10.1016/0017-9310\(68\)90084-7](https://doi.org/10.1016/0017-9310(68)90084-7).
- [10] Blackwell, B. F., Kays, W. M., and Moffat, R. J., 1972, “The Turbulent Boundary Layer on a Porous Plate: an Experimental Study of the Heat Transfer Behavior with Adverse Pressure Gradients,” Tech. Rep. HMT-16, The National Aeronautics and Space Administration.
- [11] Montgomery, D., 2012, *Design and Analysis of Experiments, 8th Edition*, John Wiley & Sons, Inc.
- [12] Bevington, P. R., and Robinson, D. K., 2003, *Data Reduction and Error Analysis*, McGraw–Hill, New York.
- [13] Jackson, J. D., Cotton, M. A., and Axcell, B. P., 1989, “Studies of Mixed Convection in Vertical Tubes,” *International Journal of Heat and Fluid Flow*, **10**(1), pp. 2–15, doi:[10.1016/0142-727x\(89\)90049-0](https://doi.org/10.1016/0142-727x(89)90049-0).

CHAPTER 5

CONCLUSIONS

This work has described the theory behind model validation, provided an example of a validation experiment, and provided links to a validation database. Steady and transient mixed convection have been studied experimentally with high-fidelity instrumentation. Steady mixed convection has been presented in previous works, but never in a validation experiment. This is the first presentation of transient mixed convection in known publications. The coupled fluid momentum and heat transfer, together with measurements of dependent variables and their spatial derivatives, make this a robust benchmark for thorough CFD validation studies. The data were provided in tabular format with adequate significant figures to make approximations unnecessary. Boundary conditions may be implemented directly in CFD models ensuring consistent inputs between experiment and simulations. System response quantities were in table format for direct comparison with model outputs and can be plotted in any program. Additionally, uncertainties of all results were provided to aid in quantifying simulation uncertainty through validation studies.

Model development and application are certain to continue as an integral part of science and engineering. The procedures and reporting in this validation experiment were good examples for others to follow for future work, though the physics and geometry will be different in each case. There is danger in performing simulations alone because the natural tendency is to trust a prediction when there is nothing with which to compare. Every research program that develops models or seeks to apply existing models to new problems needs to allot time and resources to validation. And if the physics have not been measured, the large expense of conducting experiments should be put forth. The attitude of validation is skeptical, but an appropriate level of skepticism will avoid at least some costly setbacks that often accompany incorrect predictions in science and engineering.

APPENDICES

Appendix A

Unsteady Computational Fluid Dynamics Simulations

A.1 Introduction

Since the purpose of this work was to provide validation data for computational fluid dynamics (CFD), simulations were always being performed in parallel with experiments. Initially a senior engineer at the Idaho National Laboratory (INL) performed blind studies, meaning that the knowledge was limited to the information provided in reports and the data associated with them. This approach was meant to decrease the level of bias of the modeler towards the experimental results. Modelers and experimentalists at Utah State University (USU) also ran simulations to guide the experiments as to what information was needed for model inputs, where output data should be measured, and what System Response Quantities (SRQs) would be useful for comparison. Many steady cases were run, such as for the steady mixed convection case described in this work. Furthermore, Unsteady Reynolds-Averaged Navier-Stokes (URANS) simulations were performed by the experimentalist as the previous modelers at the INL and USU were not available. This section describes the modeling approach and compares results with experimental data for the transient mixed convection case.

A.2 Methods

The URANS simulations were performed using Star-CCM+ 9.06 [1] with the experimental boundary conditions (BCs). The BCs were the as-built geometry, the temperature on all four walls and the inflow, the inflow ensemble-averaged velocity profiles, the inflow turbulence kinetic energy k profiles, and the air properties. The inflow turbulence dissipation rate profiles were determined by an empirical correlation using k [2]. The implicit unsteady model was used in combination with the Low-Re $\overline{v^2} - f, k - \epsilon$ model [3]. This model was found to perform well with buoyant flows in vertical channels [4]. Air was modeled as an ideal gas with properties as functions of temperature. Thus, buoyancy is modeled directly. Coupled momentum and coupled energy were also used to capture natural convection. Solvers were second-order accurate in space and in time. The as-built geometry was used for the fluid domain.

All normalized residuals were driven to below 1×10^{-6} at every time step. The time step was chosen for a particle to displace no more than one cell length in the streamwise direction. Converged solutions were obtained for three meshes of 15.625k, 125k, and 1M cells with equivalent cell counts in each direction of 25,

50, and 100, respectively. Cells were concentrated near the walls. The configuration for the finest mesh is shown in Fig. A.1 with the global coordinates specified. The cell size in each direction and the time step were reduced by a factor of two with each refinement. The maximum wall y^+ values were 1.5, 0.76, and 0.36, respectively. Three meshes allowed for the Grid Convergence Index method first proposed by Roache and improved upon by others to quantify numerical uncertainty [5,6]. The safety factor was allowed to increase to compensate for results with less consistency. These results are at the 95% confidence level and are used as uncertainty bands for CFD outputs in Figs. A.2 and A.3.

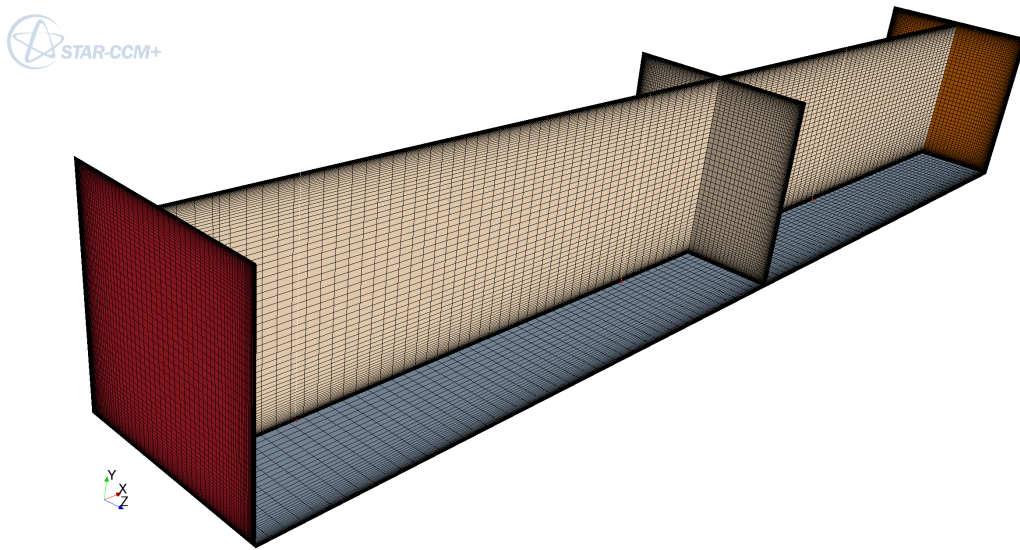


Fig. A.1: The structured rectangular mesh with 1M cells

The unsteady nature of the simulations and strict requirements placed on iterative convergence motivated the use of a computing cluster. The Division of Research Computing cluster Navier at USU was used for the medium and fine meshes while the coarsest mesh was solved on a local workstation. Simulations were setup on a local workstation and submitted as a batch job to the cluster. The workstation had 16 cores. Each node of Navier had 64 cores between four CPUs. The medium-mesh simulation used one node for 22 hours while the fine-mesh simulation used three nodes for 89 hours.

A.3 Results

Both experimental and CFD predicted profiles of ensemble-averaged streamwise velocity \bar{u} and turbulent kinetic energy \bar{k} are shown in Fig. A.2 at three locations in x for the top (x_1), middle (x_2), and bottom (x_3).

The definition $\bar{k} = \frac{1}{2} (\overline{u'u'} + \overline{v'v'} + \overline{w'w'})$ was used, assuming $\overline{w'w'} = \overline{v'v'}$ since the third component of velocity was not measured. Since the CFD model used modified two-equation RANS, the Reynolds stresses are not available and \bar{k} was the logical choice for an SRQ.

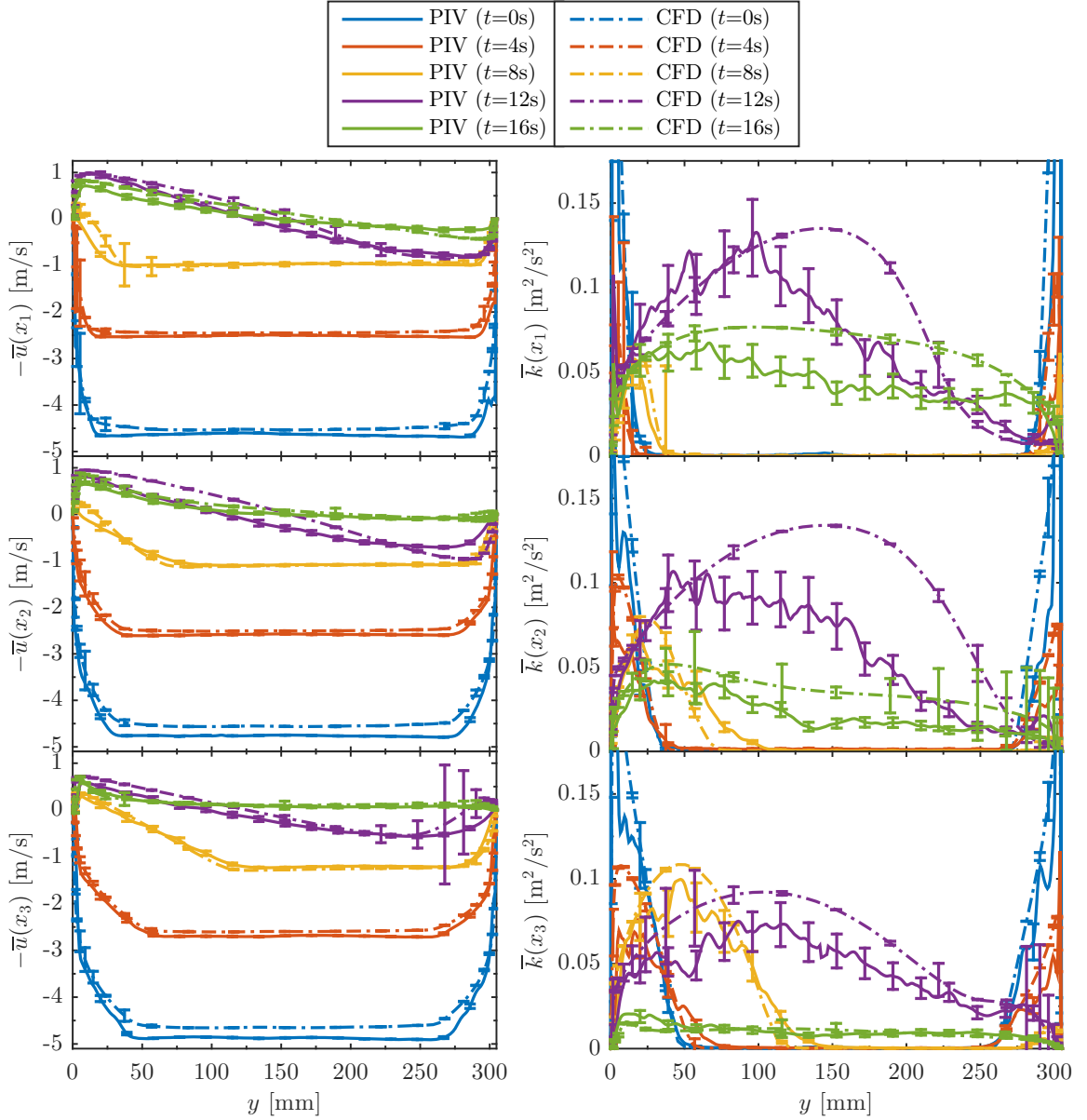


Fig. A.2: The streamwise velocity \bar{u} and turbulent kinetic energy \bar{k} for both PIV and CFD results

The streamwise velocity \bar{u} profiles from PIV and CFD show acceptable consistency through the transient. The boundary layer thickness increases in the streamwise direction x at the initial condition as expected.

There is a small difference in the bulk velocity in PIV and CFD results at this initial condition, perhaps due to a discrepancy in the inflow velocity mapping in the direction not measured. Any errors here are not inherent in the experimental BCs as inflow mapping is left to the modeler. The velocity profile shape generally remains similar but is reduced in magnitude during the first four seconds. At $t = 8$ s, the contribution from natural convection begins affecting the profiles near the heated wall ($y = 0$). At $t = 12$ s the profiles show a strong influence from natural convection. The large uncertainty bands for x_3 and large y are from the flow reversal phenomena not being mesh converged locally in the CFD. The changes from $t = 12 - 16$ s are subtle as steady natural convection is reached. The uncertainty bands are generally small on both PIV and CFD results and do not overlap, suggesting remaining model form uncertainty which is not represented nor easily quantified.

The results for turbulent kinetic energy \bar{k} are similar but have greater spatial variability and uncertainty. Initially \bar{k} is elevated near both walls as expected. The influence of natural convection increases \bar{k} near the heated wall initially. The area of elevated \bar{k} moves away from this wall over time. The phase of $t = 12$ s has the highest levels, likely from the chaotic flow reversal. The final measured state has reduced kinetic energy and may still be decreasing. Similar to streamwise velocity, the uncertainty bands generally do not overlap suggesting remaining model form uncertainty.

The uncertainty bands on CFD data are from the grid convergence study and are presented at the 95% confidence level. Particle Image Velocimetry (PIV) uncertainties are from the Uncertainty Surface Method and consider bias uncertainty from particle displacement, particle image density, particle image size, and shear originally described in [7] and improved upon with methods from [8]. Precision uncertainty was calculated by methods of Wilson & Smith [9]. Total uncertainty was calculated by the root-sum-square of the bias and precision uncertainties at the 95% confidence level.

Results for the scalars of wall heat flux and wall shear stress are shown in Fig. A.3 at the same three x locations, through time, with their associated uncertainty bands. The experimental heat flux came from the Heat Flux Sensors (HFSs) using the manufacturer-calibrated sensitivity. The uncertainty included 5% bias while the random values were measured. The heat flux results of the experiment and CFD are not in good agreement. The experimental results from the HFSs show a low sensitivity to convection due to the thermal capacitance of the heated wall, but the CFD had no capacitance modeled. Also, the CFD mesh was not well refined when considering heat flux as noted by large uncertainty bands during some phases of the transient and some physical locations. Further efforts should be made in CFD to model capacitance and refine the mesh. Wall shear has better agreement between PIV and CFD results. The experimental measurements are somewhat noisy at high levels of shear, likely from the decreased accuracy of PIV data near walls and the

relatively fewer points included in the fit. When the shear decreases, more points can be used in the fit for smoother results. The uncertainty bands on the CFD results suggest that the mesh was well resolved for shear, but again not as well in regions in space and time of flow reversal near the heated wall.

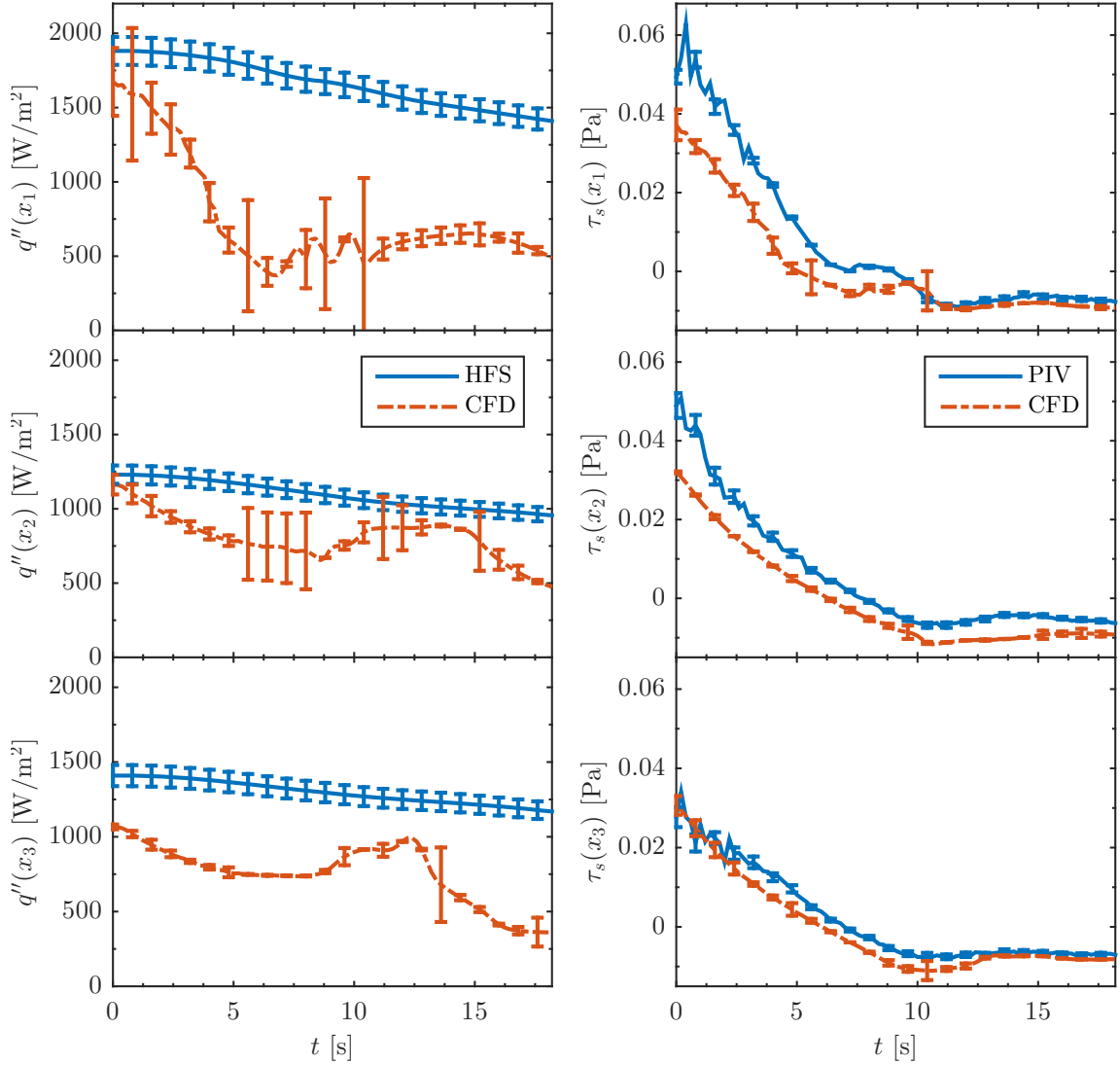


Fig. A.3: The heated wall heat flux and wall shear stress plotted over time

A.4 Conclusions

Simulations were run by the experimenter using the measured BCs. These activities confirmed the BCs were complete and formatted properly. The simulation used commercial software Star-CCM+ that ran the

URANS simulations in three-dimensions. Convergence criteria were strict. A grid convergence study was performed to estimate numerical uncertainty. Experimental results and simulation outputs were plotted on the same axes with uncertainty bands on each. This comparison can help identify simulation errors. With further work, simulation uncertainty could be quantified with the data in this study. On the other hand, the complicated nature of the data make this process challenging as the data cover two dimensions in space and one in time.

Appendix B

Processing and Post-processing Codes

B.1 Introduction

The purpose of this work was to provide validation data for computational fluid dynamics simulations. Therefore, meaningful data, their correct treatment, and proper reduction were crucial. Some have said that all raw data should be available for validation studies. In some instances this is the best approach. But there is danger in presenting raw data acquired with modern experimental techniques as the data become 1) overwhelmingly large and 2) very complicated quickly.

To address the first issue, overwhelmingly large data, it is easy to understand with examples from this work. The main measurement technique was Particle Image Velocimetry (PIV) which measured velocity fields in planes. Each plane often has at least 10,000 vectors, each with two components in the case of two-component PIV as used in this work. The uncertainty of each vector component was also quantified, doubling the data stored. A single acquisition is insufficient for averaging in time, so often 1000 acquisitions were performed for each data set. Each case included about ten sets, and there were several repeats of the data. Furthermore, the transient case had 101 phases measured. So it's easy to see how the number of data points can easily reach into the billions. These, with the many PIV images acquired, comprise several TB of space. Backing up and sharing these data becomes difficult very quickly.

With modern techniques, misinterpreting the meaning of the data is a real possibility that could have significant consequences. For instance, in nuclear reactor thermal-hydraulics, simulations are often used to assess the safety of designs in transient accident scenarios. If, in the validation of these codes, experimental data were misinterpreted, code predictions may be trusted when they shouldn't. The PIV data in this study were saved in a proprietary format that was difficult to analyze without commercial software. If a researcher were to attempt to fill the knowledge gaps, mistakes are very plausible. Data post-processing techniques are another form of complexity that may make the data misinterpreted.

In conclusion, the sharing of data is crucial to CFD validation. The data should be carefully reduced to a meaningful form and be presented in a concise way. This reduces the burden of both large data and the complexities associated with modern measurement techniques. Data averages, fluctuations, and the uncertainty in both (with confidence level used) should be included whenever possible. A global coordinate

system should be defined and included with all BC and SRQ data. Units should always be included. Any codes and/or procedures for data processing and post-processing should always be included for future reference. As such, the MATLAB codes used in this work are described and available for download through digitalcommons.usu.edu/all_datasets/8/. All of the codes may be downloaded in a single zipped file [Codes](#). If any of these codes are used for future work, a proper citation is required.

B.2 Particle Image Velocity Uncertainty

The methods and code to calculate PIV uncertainty used throughout this work were developed by others [7–9]. They were customized only slightly to plot data parameters such as particle image diameter, density, and shear relative to the range in the look-up table in the Uncertainty Surface Method. The process of quantifying the uncertainty began with creating synthetic images with known image parameters with [SIG_parallel_New_4x32x32_75%_Round_2.m](#) that contains the parameters used in this work. These images were processed in DaVis with the same steps as the data of interest. Then an uncertainty surface generator was used to read the synthetic image parameters, the velocity results from DaVis, and create an uncertainty surface with [DaVisSurfaceGeneratorFo.m](#). The uncertainty surface used in this work was [Uncertainty_4x32x32_75%_Round_PostProc_2_Used.mat](#) associated with the DaVis PIV processing settings in [Uncertainty_4x32x32_75%_Round_PostProc_2.xml](#). The code [surfaceViewer.m](#) was written to view the uncertainty surface. The uncertainty code was [PIVuncertaintyCode.m](#) with associated [PIVuncertaintyGUI.m](#) and [PIVuncertaintyGUI.fig](#). Some dependent functions of these codes were [DiaDen2.m](#) and [PIV_Stats.m](#), the latter of which had plotting capabilities added. In the steady work, the GUI was used to configure uncertainty calculation jobs and call the appropriate functions. Because the transient data had very many sets to be analyzed, this manual setup was impractical. The code [PIVuncertainty_TransientDriver2.m](#) was written to call the uncertainty code in a batch mode with much less time required by the user, at least when the file paths follow the pattern within this work. One [*Stats.m](#) file for each data set would be created that included data for the ensemble-average, Reynolds stresses, and the associated uncertainties of each. One code that will plot the nominal data and uncertainties of a given [*Stats.m](#) file was called [Plot_Uncertainties.m](#).

Since the time of this work, commercial PIV codes have included uncertainty calculations that are much easier to use and are often more accurate [10–12]. Another set of codes independent from the first was written by others to calculate only the particle image diameter and density. This set remains useful for these parameters as they are not available in known commercial software. They are in [DiaDen2.m](#), [PIVdiaden.m](#) with the associated [PIVdiadenGUI.m](#) and [PIVdiadenGUI.fig](#).

B.3 Inlet Analysis

As mentioned in this work, the inflow was measured with PIV in several planes. Several codes were written to map these velocities in space appropriately by taking single rows of data and matching them with global coordinates. The formatting is compatible as an input to commercial CFD code Star-CCM+. The code for the steady work was [InletAnalysisAndProfilesFromStats6_1.m](#) and for the transient work was [InletAnalysisAndProfilesFromStats_Transient_6_4.m](#). Another code was written to visualize the output of this code as a filled contour plot with superimposed lines to depict where data were acquired in [PlotVelocityInletContour_2.m](#).

B.4 Boundary Condition Statistics

In addition to the inflow BC data, boundary temperatures were included in several sets of files. These sets of files could be analyzed for time means and uncertainties with [BC_Stats2_2.m](#) for the steady work and ensemble-averaging and uncertainties with [BC_Stats.Transient.L.m](#) for the transient work. These codes also performed these calculations on the HFS heat flux results as they were recorded at the same time. Outlier detection and rejection was performed with the transient version.

B.5 Interpolation Codes for Boundary Conditions

The inflow velocity data could be interpolated or ‘mapped’ onto a fine grid for use in CFD by [ToStarInterpolator4_4.m](#) and [ToStarInterpolator_Transient_5_3.m](#). Also the heated wall temperatures could be interpolated by [TemptoStar.m](#).

B.6 Virtual Origin

The virtual origin analysis was performed for the steady case using velocity data at the inlet in [InletVirtualOrigin.m](#).

B.7 System Response Quantity Analysis

The averaged SRQs were analyzed with [SteadySRQ_Plots_2_8.m](#) and [TransientSRQ_Plots_2_8.m](#) as well as [SteadySRQ_Plots_HeatFlux_2_3.m](#). These codes called the functions [PIV_dudy.m](#) and [LineFitFunc.m](#) to estimate wall shear from velocity data. The code [InstantVelAnalysis.m](#) made histograms and scatter plots from instantaneous PIV data.

B.8 Transient Image Organization

The transient PIV data had a series of image pairs recorded for each run. For a given set of parameters, 101 image pairs were recorded and this was repeated for 100 or 200 runs. For proper ensemble-averaging, these data needed to be organized in 101 folders with 100 or 200 image pairs in each. The code [TransientImageOrganization_2.3.m](#) was used for this purpose. Acquisition of PIV data had inconsistent start times caused by variable delay in the PIV timing system. This delay was recorded by the master LabVIEW program and used in the organization code to properly align the data in phase. Also, outlier detection was performed on spatial averaged streamwise velocities to compensate for timing jitter with the code [Transient.OutlierDetetion.m](#) and data for subsequent runs were removed from further analysis.

B.9 Transient Computational Fluid Dynamics Grid Convergence Index

Unsteady RANS models were performed to accompany the transient work. These simulations were performed on three grids for a grid convergence study using Roache's modified method [5,6]. The four SRQ outputs from the CFD were exported at each time step associated with data acquisition in the experiment. The code [TransientCFD_GCI.m](#) read the data from the CFD simulations on all three meshes, performed the analysis, and saved the CFD SRQ data in an output file with uncertainties at the 95% confidence level.

B.10 TC Probe Analysis

The work involving the TC probe had unique codes used to analyze these results. The analysis used to estimate measurement errors from conduction losses within the probe was performed in [ConductionAnalysis2.m](#). The measured temperature profiles were analyzed and line fitted in [TempProfileAnalysis.y0-yPlusMax.loop_2.3.m](#). The heat flux results from HFSs and the TC probe, with predicted flux from correlations, were in [SteadySRQ_Plots.HeatFlux.TC_Probe.m](#).

B.11 Custom Functions

Several custom functions were used with many being written by others. Occasionally these were modified for more desired results. These included [columnlegend2.m](#), [csvwrite_with_headers.m](#), [line_fewer_markers.m](#), [sort_nat.m](#), [subtightplot.m](#), [tightfig.m](#), [tightfig2_1.m](#), [TrimToMask.m](#), and [uigetfile_n_dir.m](#).

Appendix C

Mixed Convection Parameters

Several nondimensional numbers for mixed convection are included in the following MathCAD document. Also heat transfer correlations were used for estimates. All parameters are local for the given value of x defined near the top.

Properties

$$T_{\text{inf}} := (20 + 273.15)\text{K} \quad T_{\text{plate}} := (130 + 273.15)\text{K} \quad T_f := \frac{T_{\text{plate}} + T_{\text{inf}}}{2} = 348.15\text{K}$$

$$L := 74.25\text{in} \quad w_{\text{plate}} := 11\text{in} \quad A_{\text{plate}} := L \cdot w_{\text{plate}} = 0.527\text{m}^2$$

Fluid Properties at 75 deg C from Fluid Mechanics, Cengel and Cimbala

$$\beta := \frac{1}{T_f} = 2.872 \times 10^{-3} \frac{1}{\text{K}} \quad \nu := 2.046 \times 10^{-5} \frac{\text{m}^2}{\text{s}} \quad \text{Pr} := 0.7166 \quad k := 0.02917 \frac{\text{W}}{\text{m}\cdot\text{K}}$$

This kinematic viscosity is at 1 atm, but the experiments had much lower fluid density. The following is using the ideal gas law for density and Sutherland's law for dynamic viscosity (see TransientSRQ_Plots_2_8.m). This change will affect Gr_x and Re_x but not $\text{Gr}_x/\text{Re}_x^2$.

$$\nu := 3 \cdot 10^{-5} \frac{\text{m}^2}{\text{s}}$$

The x locations of interest are at the Heat Flux Sensor locations

$$x := \begin{pmatrix} 6.3675\text{in} \\ 30.6175\text{in} \\ 54.8675\text{in} \end{pmatrix}$$

Free Convection

$$\text{Gr}_x := \frac{g \cdot \beta \cdot (T_{\text{plate}} - T_{\text{inf}}) \cdot x^3}{\nu^2} = \begin{pmatrix} 1.457 \times 10^7 \\ 1.619 \times 10^9 \\ 9.319 \times 10^9 \end{pmatrix}$$

$$\text{Ra}_x := \text{Pr} \cdot \text{Gr}_x = \begin{pmatrix} 1.044 \times 10^7 \\ 1.16 \times 10^9 \\ 6.678 \times 10^9 \end{pmatrix}$$

$$\text{Nu}_N := \left[0.825 + \frac{0.387 \text{Ra}_x^{\frac{1}{4}}}{\left[1 + \left(\frac{0.492}{\text{Pr}} \right)^{\frac{9}{16}} \right]^{\frac{8}{27}}} \right]^2 = \begin{pmatrix} 31.632 \\ 128.796 \\ 222.394 \end{pmatrix}$$

$$h_{\text{nat}} := \frac{k \cdot \text{Nu}_N}{L} = \begin{pmatrix} 0.489 \\ 1.992 \\ 3.44 \end{pmatrix} \cdot \frac{\text{W}}{\text{m}^2\text{K}}$$

Forced Convection

Bulk velocity u taken mean of u column in Inlet-uvw-interp.csv

$$u := 2.44 \frac{\text{m}}{\text{s}}$$

$$u_{\text{m}} := 4.32 \frac{\text{m}}{\text{s}}$$

Choose the appropriate velocity (mixed or forced convection cases)

$$\text{Re}_x := \frac{u \cdot x}{\nu} = \begin{pmatrix} 2.329 \times 10^4 \\ 1.12 \times 10^5 \\ 2.007 \times 10^5 \end{pmatrix}$$

$$\text{Ri}_x := \frac{\text{Gr}_x}{\text{Re}_x^2} = \begin{pmatrix} 0.027 \\ 0.129 \\ 0.231 \end{pmatrix}$$

$$\text{Nu}_F := 0.664 \cdot \text{Re}_x^{\frac{1}{2}} \cdot \text{Pr}^{\frac{1}{3}} = \begin{pmatrix} 90.68 \\ 198.843 \\ 266.184 \end{pmatrix}$$

$$h_{\text{forced}} := \frac{k \cdot \text{Nu}_F}{L} = \begin{pmatrix} 1.403 \\ 3.076 \\ 4.117 \end{pmatrix} \cdot \frac{\text{W}}{\text{m}^2 \text{K}}$$

Mixed Convection

$$\text{Nu}_{\text{mixed}} := \left(\text{Nu}_F^3 + \text{Nu}_N^3 \right)^{\frac{1}{3}} = \begin{pmatrix} 91.945 \\ 215.432 \\ 310.238 \end{pmatrix}$$

$$h_{\text{mixed}} := \frac{k \cdot \text{Nu}_{\text{mixed}}}{L} = \begin{pmatrix} 1.422 \\ 3.332 \\ 4.798 \end{pmatrix} \cdot \frac{\text{W}}{\text{m}^2 \text{K}}$$

$$q_{\text{mixed}} := A_{\text{plate}} \cdot h_{\text{mixed}} \cdot (T_{\text{plate}} - T_{\text{inf}}) = \begin{pmatrix} 82.43 \\ 193.137 \\ 278.132 \end{pmatrix} \text{W} \quad q''_{\text{mixed}} := \frac{q_{\text{mixed}}}{A_{\text{plate}}} = \begin{pmatrix} 156.432 \\ 366.53 \\ 527.83 \end{pmatrix} \cdot \frac{\text{W}}{\text{m}^2}$$

Another Correlation from the Handbook of Single-phase Convective Heat Transfer by Kakac, Shah, and Aung; Eqn 14.43:

$$c := 0.36 \quad \text{for vertical plates}$$

$$n := 3$$

$$F(\text{Pr}) := 0.0287 \cdot \text{Pr}^{0.6}$$

$$G(\text{Pr}) := 0.15 \cdot \text{Pr}^{\frac{1}{3}} \left[1 + \left(\frac{0.492}{\text{Pr}} \right)^{\frac{9}{16}} \right]^{\frac{-16}{27}}$$

$$\text{Nu}_x := F(\text{Pr}) \cdot \text{Re}_x^{\frac{4}{5}} \left[1 + c \cdot \left[\frac{G(\text{Pr})}{F(\text{Pr})} \left(\frac{\text{Gr}_x}{\text{Re}_x^{\frac{12}{5}}} \right)^{\frac{1}{3}} \right]^n \right]^{\frac{1}{n}} = 749.018$$

Appendix D

Heated Wall Conduction Analysis

The one-dimensional conduction analysis by thermal resistance network is provided in the following MathCAD document. It was used to determine the thermal resistance by conduction path going through HFSs and non-HFSs paths. The error by non-uniform resistance was estimated. The error was originally 2.4%, but with an updated thermal conductivity of Cirlex[®] (laminated Kapton[®]), was estimated to be -17.5%.

Thermal Circuit to determine heat flux difference inside Heated Plate from different conduction paths

Assume Base temperature of $T_{\text{base}} := 413.15\text{K}$ (140 C)

and Surface temperature of $T_s := 410.15\text{K}$ (137 C)

Define Thicknesses and Thermal Conductivities

Surface plate, Aluminum 2024 $t_{\text{surface}} := 0.125\text{in}$ $k_{\text{surface}} := 141 \frac{\text{W}}{\text{m}\cdot\text{K}}$

Total thickness of adhesive in combination with HFS or Cirlex $t_{\text{total}} := 0.05\text{in}$

Heat Flux Sensor $t_{\text{HFS}} := 0.013\text{in}$ $k_{\text{HFS}} := 0.156 \frac{\text{W}}{\text{m}\cdot\text{K}}$

Cirlex $t_{\text{Cirlex}} := 0.010\text{in}$ $k_{\text{Cirlex}} := 0.12 \frac{\text{W}}{\text{m}\cdot\text{K}}$

updated k for Cirlex from Fralock and Katco $k_{\text{Cirlex}} := 0.17 \frac{\text{W}}{\text{m}\cdot\text{K}}$

Adhesive layer over HFS $t_{\text{ad_HFS}} := t_{\text{total}} - t_{\text{HFS}} = 0.037\text{in}$

Adhesive layer over Cirlex $t_{\text{ad_Cirlex}} := t_{\text{total}} - t_{\text{Cirlex}} = 0.04\text{in}$

$k_{\text{ad}} := 1.0 \frac{\text{W}}{\text{m}\cdot\text{K}}$

Base Metal, Aluminum 6061 $t_{\text{base}} := 0.25\text{in}$ $k_{\text{base}} := 167 \frac{\text{W}}{\text{m}\cdot\text{K}}$

Thermal Circuit Analysis

$$V = I \cdot R \quad T_1 - T_2 = q'' \cdot R'' \quad q'' = \frac{T_1 - T_2}{R''}$$

Consider two parallel paths and compare thermal resistance and heat flux

$$R''_{\text{HFS}} := \frac{t_{\text{base}}}{k_{\text{base}}} + \frac{t_{\text{HFS}}}{k_{\text{HFS}}} + \frac{t_{\text{ad_HFS}}}{k_{\text{ad}}} + \frac{t_{\text{surface}}}{k_{\text{surface}}} = 3.117 \times 10^{-3} \cdot \frac{\text{m}^2\text{K}}{\text{W}}$$

$$R''_{\text{Cirlex}} := \frac{t_{\text{base}}}{k_{\text{base}}} + \frac{t_{\text{Cirlex}}}{k_{\text{Cirlex}}} + \frac{t_{\text{ad_Cirlex}}}{k_{\text{ad}}} + \frac{t_{\text{surface}}}{k_{\text{surface}}} = 2.571 \times 10^{-3} \cdot \frac{\text{m}^2\text{K}}{\text{W}}$$

$$q''_{\text{HFS}} := \frac{T_{\text{base}} - T_s}{R''_{\text{HFS}}} = 962.461 \frac{\text{W}}{\text{m}^2}$$

$$q''_{\text{Cirlex}} := \frac{T_{\text{base}} - T_s}{R''_{\text{Cirlex}}} = 1.167 \times 10^3 \cdot \frac{\text{W}}{\text{m}^2}$$

$$\frac{q''_{\text{HFS}}}{q''_{\text{Cirlex}}} = 0.825$$

Error on k_{Cirlex} with a Measured Error From the Design of Experiments Analysis

$$\frac{q''_{\text{Cirlex}}}{q''_{\text{HFS}}} = \frac{T_1 - T_2}{R''_{\text{Cirlex}}} \cdot \frac{R''_{\text{HFS}}}{T_1 - T_2} = \frac{R''_{\text{HFS}}}{R''_{\text{Cirlex}}} = \frac{\frac{t_{\text{base}}}{k_{\text{base}}} + \frac{t_{\text{HFS}}}{k_{\text{HFS}}} + \frac{t_{\text{ad_HFS}}}{k_{\text{ad}}} + \frac{t_{\text{surface}}}{k_{\text{surface}}}}{\frac{t_{\text{base}}}{k_{\text{base}}} + \frac{t_{\text{Cirlex}}}{k_{\text{Cirlex}}} + \frac{t_{\text{ad_Cirlex}}}{k_{\text{ad}}} + \frac{t_{\text{surface}}}{k_{\text{surface}}}} = E$$

Solving for k_{Cirlex}

$$k_{\text{Cirlex_Corrected}} := t_{\text{Cirlex}} \cdot \left[\left(\frac{t_{\text{base}}}{k_{\text{base}}} + \frac{t_{\text{HFS}}}{k_{\text{HFS}}} + \frac{t_{\text{ad_HFS}}}{k_{\text{ad}}} + \frac{t_{\text{surface}}}{k_{\text{surface}}} \right) \cdot \frac{1}{E} \dots \right]^{-1} + \left(\frac{t_{\text{base}}}{k_{\text{base}}} + \frac{t_{\text{ad_Cirlex}}}{k_{\text{ad}}} + \frac{t_{\text{surface}}}{k_{\text{surface}}} \right)$$

$$k_{\text{Cirlex_Corrected}} = 0.162 \cdot \frac{\text{W}}{\text{m} \cdot \text{K}} \quad \frac{k_{\text{Cirlex_Corrected}}}{k_{\text{Cirlex}}} = 0.955$$

The thermal conductivity k of the original Cirlex would have to be off by 35% to have an 18% error. This seems unlikely.

The updated k_{Cirlex} could be off by 4.5%, which suggests that its value is pretty close.

Appendix E

Permission Letter for Steady Mixed Convection Work

Jeff Harris

PO Box 30
State College, PA 16801
Phone: 814-863-3025

► **Utah State University**

Old Main Hill
Logan, UT 84322
Phone: 435-797-1000

To whom it may concern:

The paper *Experimental Validation Data for CFD of Mixed Convection on a Vertical Flat Plate* written by Blake Lance, Barton Smith, and myself may be used to fulfil the dissertation and graduation requirements of the first author.

Respectfully,
Jeff Harris
Research Associate
The Pennsylvania State University
8/6/2015

References

- [1] CD-Adapco, Melville, NY, *Star-CCM+ User Guide*, 9.06 ed.
- [2] Versteeg, H. K., and Malalasekera, W., 2007, *An Introduction to Computational Fluid Dynamics*, Prentice Hall.
- [3] Davidson, L., Nielsen, P., and Sæviingsson, A., October 12-17, 2003, “Modifications of the $\overline{v^2} - f$ Model for Computing the Flow in a 3D Wall Jet,” Proceedings of the International Symposium on Turbulence, Antalya, Turkey.
- [4] Moutaouakil, L. E., Zrikem, Z., and Abdelbaki, A., 2014, “Performance of Various RANS Eddy-viscosity Models for Turbulent Natural Convection in Tall Vertical Cavities,” *Heat Mass Transfer*, **50**(8), pp. 1103–1113, doi:[10.1007/s00231-014-1322-4](https://doi.org/10.1007/s00231-014-1322-4).
- [5] Roache, P. J., 1997, “Quantification of Uncertainty in Computational Fluid Dynamics,” *Annual Review of Fluid Mechanics*, **29**(1), pp. 123–160, doi:[10.1146/annurev.fluid.29.1.123](https://doi.org/10.1146/annurev.fluid.29.1.123).
- [6] Oberkampf, W. L., and Roy, C. J., 2010, *Verification and Validation in Scientific Computing*, Cambridge University Press, doi:[10.1017/cbo9780511760396](https://doi.org/10.1017/cbo9780511760396).
- [7] Timmins, B. H., Wilson, B. W., Smith, B. L., and Vlachos, P. P., 2012, “A Method for Automatic Estimation of Instantaneous Local Uncertainty in Particle Image Velocimetry Measurements,” *Experiments in Fluids*, **53**(4), pp. 1133–1147, doi:[10.1007/s00348-012-1341-1](https://doi.org/10.1007/s00348-012-1341-1).
- [8] Warner, S. O., and Smith, B. L., 2014, “Autocorrelation-based Estimate of Particle Image Density for Diffraction Limited Particle Images,” *Measurement Science and Technology*, **25**(6), p. 065201, doi:[10.1088/0957-0233/25/6/065201](https://doi.org/10.1088/0957-0233/25/6/065201).
- [9] Wilson, B. M., and Smith, B. L., 2013, “Taylor-series and Monte-Carlo-method Uncertainty Estimation of the Width of a Probability Distribution Based on Varying Bias and Random Error,” *Meas. Sci. Technol.*, **24**(3), p. 035301, doi:[10.1088/0957-0233/24/3/035301](https://doi.org/10.1088/0957-0233/24/3/035301).
- [10] LaVision, 2015, “DaVis,” Version 8.2.
- [11] Wieneke, B., 2015, “PIV Uncertainty Quantification from Correlation Statistics,” *Measurement Science and Technology*, **26**(7), doi:[10.1088/0957-0233/26/7/074002](https://doi.org/10.1088/0957-0233/26/7/074002).
- [12] Sciacchitano, A., Neal, D. R., Smith, B. L., Warner, S. O., Vlachos, P. P., Wieneke, B., and Scarano, F., 2015, “Collaborative Framework for PIV Uncertainty Quantification: Comparative Assessment of Methods,” *Measurement Science and Technology*, **26**(7), doi:[10.1088/0957-0233/26/7/074004](https://doi.org/10.1088/0957-0233/26/7/074004).

CURRICULUM VITAE

Blake W. Lance

29 Aggie Vlg Apt G – Logan UT – USA

☎ 435-512-7968 • ☎ 435-797-8147 • ✉ b.lance@aggiemail.usu.edu
in BlakeLance

Education

Utah State University	Logan
<i>Ph.D. in Mechanical Engineering, 4.0</i>	2012–2015
Utah State University	Logan
<i>M.S. in Mechanical Engineering, 3.91</i>	2011–2012
Utah State University	Logan
<i>B.S. in Mechanical Engineering, 3.90</i>	2007–2012
Magna cum Laude, Mathematics minor	

Training

Los Alamos National Lab	Los Alamos
<i>Advanced Studies Institute</i>	<i>April–May 2015</i>
Gained professional exposure to current research and gained training and experience in proposal writing	
Idaho National Lab	Idaho Falls
<i>Modeling, Experimentation, and Validation (MeV) Summer School</i>	<i>July 2014</i>
Learned from experts in Nuclear Reactor Safety, contributed a large portion to group paper and presentation, earned Best Group Presentation Award	
Bill Oberkamp & Chris Roy	Las Vegas
<i>ASME Verification, Validation, and Uncertainty Quantification Workshop</i>	<i>May 2014</i>
Learned theory and best practices from two leading experts in the VVUQ field applied to fluid dynamics and heat transfer	

Ph.D. Dissertation

title: “*Experimental Validation Data for CFD of Steady and Transient Mixed Convection on a Vertical Flat Plate*”

supervisor: Barton L. Smith

description: Experiments were conducted for the purpose of providing validation data to Computational Fluid Dynamics simulations. The physics were steady and transient convection on a vertical flat plate with notable buoyancy effects. The measurements and description were very detailed and extra effort was invested in disseminating the data in an organized, straightforward way. The data may be used to assess simulation error and even prediction uncertainty.

Masters Thesis

title: “Using Stereo Particle Image Velocimetry to Quantify and Optimize Mixing in an Algae Raceway Using Delta Wings”

supervisors: Byard Wood & Barton L. Smith

description: An economical method for growing algae for biofuels is to use open raceway ponds, but these suffer from low fluid mixing. A novel application of a delta wing in these raceway ponds is to create mixing of the growth culture, a change which should increase growth rates. Experiments were conducted in a model raceway to measure optimal parameters for the use of these wings to increase mixing. Particle Image Velocimetry measured high fidelity velocity data to quantify mixing levels.

Experience

Research.....

Utah State University

Logan

Graduate Research Assistant (Ph.D.)

August 2012–present

- Performed validation experiments using specialized Rotatable Buoyancy Tunnel (RoBuT) at USU
- Acquired velocity data using Particle Image Velocimetry (PIV) and best practices
- Developed detailed instrumentation and control hardware and software
- Developed data post-processing codes for organizing, reduction, and plotting of data
- Performed URANS simulations in commercial package using best practices
- Performed grid convergence, sensitivity, and validation studies
- Advised Undergraduate Research Assistants on experimental setup and execution, code development, and database management

Utah State University

Logan

Graduate Research Assistant (M.S.)

August 2011–August 2012

- Quantified fluid mixing enhancement in scaled raceway with PIV by use of delta wings
- Performed optimization study on wing configuration and raceway fluid speed to potentially increase algae productivity and reduce operation costs
- Developed Stereo PIV expertise in water
- Performed power measurement on three-phase, pulsed power with basic instrumentation
- Advised Undergraduate Research Assistants on experimental setup and execution

Utah State University

Logan

Undergraduate Researcher (B.S.)

May 2009–May 2011

- Designed, built, and tested heated and instrumented plate for validation experiments in RoBuT
- Assisted contractor in the design and assembly of the RoBuT facility
- Designed, built, and tested reference heat flux generator for sensor calibration
- Assisted others in the execution, troubleshooting, and data analysis of experiments
- Completed coding project modifying commercial code

Professional.....

Sandia National Labs

Albuquerque

Graduate Student Intern

May 2013–November 2014

- Configured unsteady experiment for phase locked data acquisition in oscillatory water tunnel
- Performed first known statistical analysis of coherent turbulent structures in oscillating flow
- Acquired experimental data on schedule
- Demonstrated best practices for data acquisition and processing
- Used safety practices to government lab standards

Apogee Instruments

Logan

Mechanical Engineering Intern

May 2011–August 2011

- Improved design of Aspirated Radiation Shield through heat transfer analyses
- Contributed to several R&D projects in multi-disciplinary groups for new products
- Developed new products and manufacturing facilities, including solid model development

Teaching

Utah State University

Logan

Graduate Teaching Assistant

August 2011–December 2011

- Assisted 100 students in learning the concepts of Thermodynamics II
- Tutored during weekly recitation and office hours
- Consistently graded homework every week

Specialized Skills

Experimental Experience

- Calibration, data filtering, amplification, fourier transforms, cross-correlations, and uncertainty analysis
- Steady and unsteady 2-component and 3-component PIV in water and air
- Phase-locked data acquisition and analysis of periodic and non-periodic transient experiments
- Data acquisition and systems control using LabVIEW
- Temperature measurement theory and practice
- Electrical circuit theory and design
- Laser alignment and safety practices

Numerical Experience

- Data processing, post-processing, and plotting in FORTRAN and MATLAB
- Automated organization and processing of large data sets
- Computational Fluid Dynamics modeling with Star-CCM+, FLUENT, and personal codes using RANS and URANS models
- High performance computing experience with personal and commercial codes using Linux clusters
- Sensitivity, grid convergence, and validation studies
- Finite element modeling with FEMAP and ALGOR
- Desktop computer assembly and repair

Computing Languages

- MATLAB, FORTRAN, and LabVIEW

Software Packages.....

- Microsoft Office, Star-CCM+, FLUENT, SolidWorks, SolidEdge, MathCAD, L^AT_EX, DaVis

Awards

Fellowship.....

- U.S. Nuclear Regulatory Commission Fellowship, 2012–2016

Scholarships.....

- U.S. Nuclear Regulatory Commission Scholarship, 2009–2011
- USU Presidential Scholarship, 2007–2012
- Sam Walton Community Scholarship, 2007–2008

Recognitions.....

- Mechanical & Aerospace Engineering (MAE) Outstanding Ph.D. Researcher, 2015
- MAE Outstanding Undergraduate Researcher, 2011
- Tau Beta Pi Engineering Honor Society Membership, 2009
- MAE Academic Excellence Award, 2009–2011
- MAE A-Pin Awarded for Academic Excellence, 2008
- MAE Lundberg Excellence Award, 2007–2009
- USU Dean's List, 2007–2008

Service

Treasurer of USU Nuclear Club (Interim ANS Chapter).....

- Was elected to the first executive council on interim ANS Chapter at USU
- Prepared activities and petition to gain official chapter recognition
- Performed public outreach at Engineering Week Community Night

Volunteer Amateur (Ham) Radio Operator.....

- Provided volunteer communications for church organization and athletic events
- Assembled radio equipment systems for emergency operations
- Initiated and organized class for public to acquire licensing and learn operating practices

Clerk in Local Church.....

- Recorded minutes of meetings and submitted performance reports
- Kept member and financial records
- Trained and supervised other clerks
- Coordinated schedules and prepared meeting agendas

Boy Scouts of America Eagle Scout Award.....

- Prepared 80 personal chalkboards for humanitarian education kits
- Managed several groups of volunteers and raised funds for materials
- Learned life skills and personal management

Publications

Journal Papers.....

- Lance, B., Harris, J., and Smith, B. "Experimental Validation Data for CFD of Mixed Convection on a Vertical Flat Plate," *Journal of Verification, Validation and Uncertainty Quantification*, submitted September 2015.
- Harris, J., Lance, B., and Smith, B. "Experimental Validation Data for Computational Fluid Dynamics of Forced Convection on a Vertical Flat Plate," **138**(1), *Journal of Fluids Engineering*, 2015, doi:10.1115/1.4031007.

Invited Presentations.....

- Lance, B. "Validation Experiments," NAVSEA Carderock Division Hydrodynamics Colloquium, Sept. 29, 2015, Bethesda, MD.
- Lance, B., "Transient Convection from Forced to Natural with Flow Reversal on a Vertical Flat Plate for CFD Validation," VVUQ Colloquium at Sandia National Labs, Aug. 25, 2015, Albuquerque, NM.
- Lance, B. and Smith, B. "Particle Image Velocimetry and the Nuclear Field," American Nuclear Society Chapter Lecture, Nov. 19, 2014, Logan, UT.

Conference Papers.....

- Lance, B. and Smith, B. "Transient Convection from Forced to Natural with Flow Reversal for CFD Validation," 16th International Topical Meeting on Nuclear Reactor Thermal Hydraulics, August 30–September 4, 2015, Chicago, IL.
- Lance, B. and Smith, B. "Transient Convection from Forced to Natural with Flow Reversal for CFD Validation," 2015 American Nuclear Society Annual Meeting, June 7–11, 2015, San Antonio, TX.
- Lance, B. and Harris, J. "Mixed Convection Validation and Simulation," American Nuclear Society 2014 Student Conference, April 3–5, 2014, State College, PA.
- Lance, B., Harris, J., Iverson, J., Spall, R., Johnson, R., and Smith, B., "Validation Study on Forced and Mixed Convection in the Rotatable Buoyancy Tunnel," ASME 2013 Fluids Engineering Division Summer Meeting, July 7–11, 2013, Incline Village, NV, Paper Number 16214.
- Harris, J., Lance, B., and Smith, B., "Design of Apparatus for Validation Experiments," American Nuclear Society Annual Meeting, June 16–20, 2013, Atlanta, GA.
- Harris, J., Lance, B., Spall, R., and Smith, B., "Transient Mixed Convection Validation Facility and Study," The 15th International Topical Meeting on Nuclear Reactor Thermal Hydraulics (NURETH), May 12–16, 2013, Pisa, Italy, Paper Number 15-356.
- Harris, J., Lance, B., and Iverson, J., "Single Phase Forced Convection Validation and Simulation," American Nuclear Society 2013 Student Conference, April 4–6, 2013, Boston, MA. ○ **Awarded Best Overall Graduate Paper.**

Conference Presentations.....

- Lance, B. and Smith, B. "Experimental Transient Convection from Forced to Natural with Flow Reversal for CFD Validation," 2015 ASME Verification and Validation Symposium, May 11-15, 2015, Las Vegas, NV.

- Lance, B., Roberts, J., Kearney, S., and Smith, B. "Wall Shear Stress in Oscillating Channel Flow Using Particle Image Velocimetry," 66th Annual Division of Fluid Dynamics Meeting of the American Physical Society, Nov. 24-26, 2013, Pittsburgh, PA.
- Harris, J., Lance, B., and Smith, B. "Experimental Validation Dataset for CFD Simulations of Buoyancy Opposed Convection," 66th Annual Division of Fluid Dynamics Meeting of the American Physical Society, Nov. 24-26, 2013, Pittsburgh, PA.
- Smith, B., Lance, B., Harris, J., Iverson, J., and Spall, R. "The RoBuT Wind Tunnel for CFD Validation of Natural, Mixed, and Forced Convection," 2013 ASME Verification and Validation Symposium, May 22-24, 2013, Las Vegas, NV.
- Harris, J., and Lance, B. "The Design and Implementation of Simulation Validation Experiments for Passive Cooling Features in Nuclear Reactors," Utah State University Graduate Research Symposium, April 12, 2013, Logan UT. ○ **Honorable Mention Award.**
- Lance, B., Wood, B., and Smith, B., "Optimizing Open Raceway Design," USTAR BioEnergy Summit, August 7, 2012, Logan, UT.